POLITECNICO DI TORINO

Corso di Laurea Magistrale
in Ingegneria Meccanica

Tesi di Laurea Magistrale

Triboelectric Sensing for Soft Robots

Relatori:
Prof. Giacomo Frulla
Prof. Enrico Cestino

Candidato:
Gianluca Palucci

Anno Accademico 2019/2020

PURDUE UNIVERSITY

Supervisore esterno:
Dr. James M. Gibert

College of Engineering
School of Mechanical Engineering

Ray W. Herrick Laboratories

ACKNOWLEDGEMENTS

I would like to thank my advisors, professor Giacomo Frulla and professor Enrico Cestino, for giving me the opportunity to research such an interesting topic on the other side of the ocean, in one of the best universities of the world. I would also like to thank my external advisor Dr. James Gibert for giving me the chance to join his research team and for his constant guidance and support during my stay at Purdue. I would also like to express my gratitude to the Herrick laboratories staff for their technical assistance and for providing me with everything I needed for my research. A special thanks goes to Hongcheng Tao and Dr. Francesco Danzi for their precious help in every stage of the work, without them I would probably still be moving my first tentative steps in this research. I would also like to thank Sami Khreisat, Amin Joodaki and all the other members of Dr. Gibert's team for providing me with a very stimulating environment from which to draw inspiration for my work.

Contents

List of Figures

Abstract

Triboelectric nanogenerators are a promising technology for converting mechanical energy from the ambient environment into electric energy at high efficiency rates. The versatility in design, the high surface power densities achievable, the ease of building and the non-negligible advantage of being very adaptable to the use of the most different sources of mechanical energy for energetic conversion make these devices particularly interesting in the fields of energy harvesting and energy storage, in addition to or in substitution of common electrochemical batteries. In recent years, researchers around the world have been able to further enhance the encouraging capabilities of triboelectric nanogenerators whose potential fields of utilisation have consequently become broader and more varied. As sources of power, they have been used (Yang Wang et al. 2017) in wearable and portable electronic devices to provide electric energy by converting mechanical energy harvested from human body motions. As skin sensors, they have been used (Minjeong Ha et al. 2015) to detect external stimuli by converting mechanical forces into electric outputs.

Their ability to generate electric outputs from external mechanical forces has proved to be of great interest in assessing the deformation of objects for which triboelectric devices could work as deformation sensors. In this dissertation, this property is used to develop a triboelectric deformation sensor for soft pneumatic actuators. These actuators, also known as soft robots, are used in those situations in which traditional hard-bodied robots may not be particularly suited for, such as surgical assistance or human-robot interactions (wearable robots, prosthetics).

The work will be divided into three different phases. A first phase describing all the steps undertaken in the design and assembly of functioning soft robots and triboelectric devices and in the subsequent efforts to embed the triboelectric sensor into the soft robot body. A second phase where a model is developed in the simulation environment to study the behaviour of the robot-embedded sensor during cycles of loading corresponding to the inflation of the chambers of the robot. A last phase where the prototypes built in the first phase are tested and where the results of this experimental testing are compared with the simulation results, so that the correlation that exists between displacement and electric output during the inflation of the robot chambers can be determined.

1 An overview on triboelectric nanogenerators

1.1 Introduction

In the last couple of decades, large scale and small scale energy-harvesting technologies have been developed at an unprecedented rate to meet the demands of an ever expanding market and to address the environmental consequences of the increasing leves of greenhouse gases in the atmosphere linked to human activities. Transitioning from fossil fuels to renewable sources of energy, like wind power or solar power, has been the struggle of the new millennium, and it has proved to be of vital importance if we are to put a halt on carbon emissions and try to contain the negative effects of climate change. Moreover, if on one hand the increasing demand of energy and the efforts to reduce carbon emissions have prompted the research of new alternatives to conventional energy sources, the worldwide diffusion of portable, if not wearable, electronic devices has further stimulated the study of new technologies also in respect to the energy storage problems associated with this booming market. In this, finding energy-dense and highly charge-efficient batteries has been the primary objective of researchers.

Today basically every mobile electronic device uses batteries as a power source. Conjugating high energy densities with high charge efficiencies and low rates of self-discharge, lithium-ion and lithium polymer batteries are just some of the many typologies adopted by electronics manufacturers, with some others, like lithium-sulphur batteries, still in the developement. Thanks to these properties, most laptops, smartphones, digital cameras nowadays are built with lithium-based batteries as the preferred storage units. Yet, even the best performing batteries cannot guarantee particularly long lifetimes, and while huge progress has been made in regard to their life cycles, their limited durability continues to be a most pressing issue for a more widespread use in future. Furthermore, the environmental damages associated with lithium mining and extraction, as well as the potential harmful ecological impact of its disposal, once the electrochemical cells of the battery are exhausted, has not been properly addressed yet. Therefore even if they are among the best performing batteries currently available on the market and even if the ecological consequences of their use can be contained within certain limits through adequate care, these negative aspects proper of lithium batteries, but not exclusive to them, hamper some of the efforts to transition from a fossil fuel-based economy to a battery-powered one.

Therefore, to account for these downsides, in the past decade researchers have focused their attention on nanogenerators as a way to transition from the short-lived and potentially ecologically hazardous electrochemical batteries to cleaner and more durable technologies. Piezoelectric nanogenerators, pyroelectric nanogenerators and triboelectric nanogenerators are some of the more recent solutions that have been developed to work as energy harvester and power sources for nano and micro-electric devices. Characterised by high energy-conversion efficiencies, triboelectric devices in particular, are among the most promising technologies to have been developed in the latest years. Via contact electrification and electrostatic induction, these triboelectric nanogenerators, commonly shortened into TENGs, convert mechanical energy from the environment into electric energy. The great adaptability of design shown by TENGs further enhances their ability to convert mechanical energy into electric energy at high conversion efficiencies, even from non-conventional power sources, such as human body motion when it comes to wearable electronic devices [1] [2]. And to the already mentioned merits of longer life cycles and better ecological sustainability as compared with common-use batteries, TENGs add large power outputs, low weights and, as said, high energy-conversion efficiencies and great design flexibility; moreover, they are easy to produce and they can be built from a large array of materials, which means that potentially they can also be very cost-effective [3] [4].

Given these impressive properties, by testing different combinations of materials or by rearranging the geometry of the TENGs active parts to better adapt to the ambient from which to convert the mechanical energy, it is possible to improve their already remarkable performances. The optimisation of these devices mostly comes as a result of the enhancement of the electrical properties of the materials, mainly of the dielectric layers, or as a result of the increase of the area of electrical charge exchange between the layers of dielectrics/electrodes. For example, boosting the surface charge densities of the dielectric layers or augmenting their relative permittivity by using materials such as carbon nanotubes has been one of such undertakings [1] [2]. Adopting different structural solutions to increase the exchange surface interface between the dielectric layers or the flexibility of the structure, like building kirigami-patterned TENGs, has also been the focus of some of the most recent studies [5]. Through these kinds of optimisations, it has been possible to build TENGs with surface power densities as high as 490 W/m^2 that are also capable of reaching energy-conversion efficiencies of up to 85 % [3] [6].

So, with the electrochemical batteries current limitations and with the efforts to reduce our dependence upon non-renewable power sources, triboelectric generators have become increasingly more attractive as research went on. For example, their advantages over less efficient energy sources have became more apparent; their ability to convert mechanical energy into electric energy from non conventional sources is particularly interesting. Supplying power to micro or nano systems in portable and wereable devices, in lieu or in tandem with batteries, is one of the most sought-after objectives of researchers who are working on triboelectric generators. In addition to this, being still a relatively young technology, it is probable that in the foreseeable future the potential range of applications of TENGs may be decidedly increased; to this scope, testing different solutions to enhance the performances of TENGs, like adopting materials with compatible electrical properties or improving the energy conversion by increase of the area of exchange of the electric charges is something worth investigating.

1.2 Working principle of TENGs and basic structures

1.2.1 Working principle

The mechanisms which drive energy conversion in TENGs, i.e. contact electrification and electrostatic induction, can be attributable to only two different types of motion of the active parts of the device, vertical contact-separation and lateral sliding. To describe how TENGs work, it is useful to first consider the simplest geometry currently adopted: as shown in **Fig. 1** down below, two layers of dielectrics (material 1 and material 2 in the figure) are separated by a thin air gap; attached to each one of these dielectric materials is an electrode. The two electrodes are connected to one another through an external circuit, but are otherwise insulated inside the device. Due to contact electrification, when an external load brings the dielectric strata into contact, electrostatic charges of opposite sign will appear on the now-touching inner surfaces of the dieletric materials. For the electrostatic equilibrium, on the interfaces of contact, the two dielectric materials will have an equal amount of charges uniformally distributed on each surface, negative charges on one side and positive on the other. As the load is released, the active layers of the TENGs, which were previously brought into contact, separate; a potential difference is established between the two electrodes as the air gap reforms between the dielectrics. This potential difference, which is proportionate to the thickness of the newly reformed air gap between the dielectric layers, prompts electrons to flow through the external circuit from one electrode to the other until the system reaches a new equilibrium. This cycle will repeat itself under new loads.

For the sake of simplicity, in the following equations the assuption of infinitely large surfaces of charge exchange has been adopted. This assumption is justified by the fact that the thickness of the electrodes and of the dielectric layers, along with the thickness of the air gap between them is several orders of magnitudes smaller than the size of the surface of charge exchange.

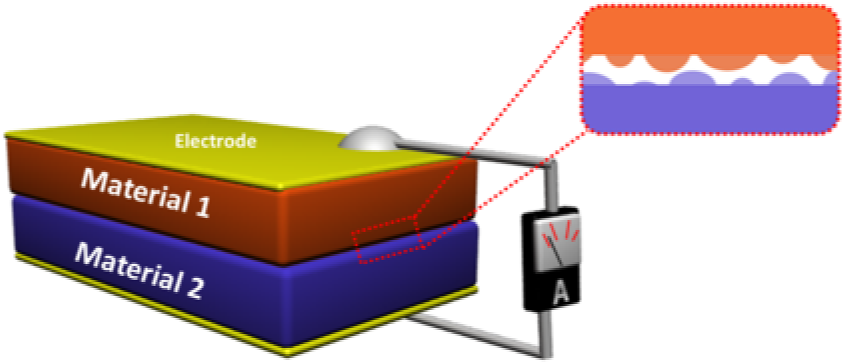

Figure 1: Scheme of a triboelectric nanogenerator. Reproduced from Ref. 27.

When operating, triboelectric nanogenerators show capacitive behaviours, where the capacitance $C(x)$ of the TENG is function of the distance x of the dielectic layers [3]. The potential difference which exists between the electrodes as a consequence of the application of an external load on the device can therefore be described by the following equation, commonly referred to as the V-Q-x relationship [3] [6]:

$$V = -\frac{1}{C(x)}Q(x) + V_{OC}(x) \tag{1}$$

where $Q(x)$ represents the transferred charges.

As evident from this equation, the electric potential difference V is given by the sum of two terms. One term is correlated with the capacitive behaviour of the device and is directly proportional to the transferred charges $Q(x)$, while the other, $V_{OC}(x)$, which is function of the thickness of the air gap between the materials, represents the contribution to V of the polarised charges distributed on the opposing faces of the dielectric layers inner surfaces, after the application of the load. Thus, in an open circuit condition, the potential difference between the electrodes will correspond solely to the second term $V_{OC}(x)$. On the other hand, the presence of an external circuit connecting the two electrodes will drive electrons from one electrode to the other, progressively counterbalancing the effect of the polarised charges; under short-circuit conditions, the flow of transferred charges will completely screen the contribution of the polarised charges on the electric potential difference, which, consequently, will go to zero [3]:

$$0 = -\frac{1}{C(x)} Q_{SC}(x) + V_{OC}(x) \tag{2}$$

Or, rearranged:

$$Q_{SC}(x) = C(x) V_{OC}(x) \tag{3}$$

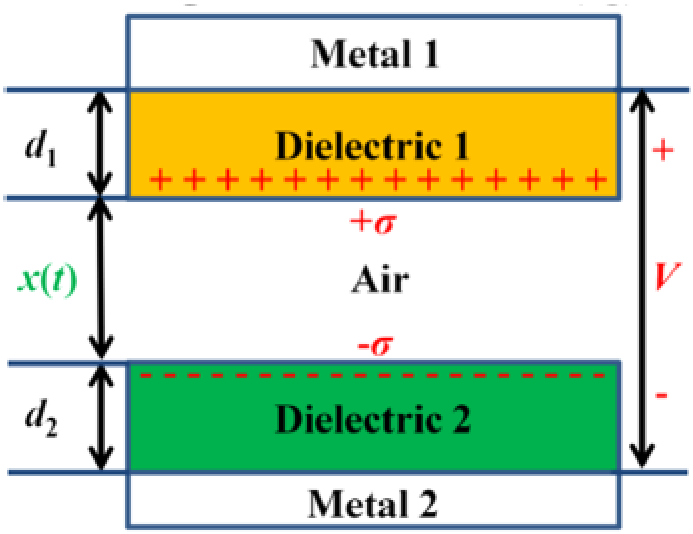

Figure 2: Theoretical model of a contact-mode TENG. Reproduced from Ref. 28.

The V-Q-x relationship, as described in **Eq. (1)**, highlights the great importance of the polarised triboelectric charges on the potential difference; the greater the term $V_{OC}(x)$ the greater the potential difference measured in the system. To enhance the value of $V_{OC}(x)$ it is convenient to choose materials which could increase the surface charge density σ on the inner faces of the dielectric layers after the application of the external load. In particular, two materials with a marked tendency to, respectively, lose and gain electrons should be chosen as the preferred dielectrics pair [3]. This is because $V_{OC}(x)$, and consequently V too, is directly proportional to the surface density of charges σ. In a system such as the one represented in **Fig. 1**, with a vertical load forcing into contact the two dielectric layers, this proportionality can be described by the following equation [3]:

$$V_{OC} = \frac{\sigma x(t)}{\epsilon_0} \tag{4}$$

as evident from this equation, V_{OC} is also linearly dependent on the separation distance $x(t)$ of the dielectric layers of the device; the system of **Fig. 1** under a vertical load is depicted in **Fig. 2**. It is convenient, within certain margins, to increase this distance in order to improve the output performances of the nanogenerator, but for too large distances the "edge effect" can prevail on charge transfer, reducing both charge transfer efficiency and output performances. A more detailed description of this phenomenon can be found at the end of the first part of this chapter.

The relative permittivities ϵ_r of the dielectric materials, on the other hand, while certainly affecting the capacitance C of the system, are not as important when it comes to the electric potential difference between the electrodes [3]. Again for the system as depicted in **Fig. 1**, the capacitance can be defined as:

$$C = \frac{\epsilon_0 S}{d_0 + x(t)} \tag{5}$$

where d_0 represents the effective dielectric thickness of the system, in turn given by the following equation:

$$d_0 = \sum_{i=1}^{n} \frac{d_i}{\epsilon_{ri}} \tag{6}$$

which shows the clear dependency of C upon the relative permittivities of the dielectric materials. As said, this dependency has little effect on the overall potential difference generated between the electrodes. Recalling the V-Q-x relationship described in **Eq. (1)**, and substituting in it the results of **Eq. (4)** and **(5)** yields:

$$V = -\frac{Q}{S\epsilon_(0)}(d_0 + x(t)) + \frac{\sigma x(t)}{\epsilon_0} \tag{7}$$

In such a system, the transferred charges under short-circuit conditions will be:

$$Q_{SC}(x) = \frac{S\sigma x(t)}{d_0 + x(t)} \tag{8}$$

While the charge transfer efficiency:

$$\eta_t = \frac{Q_{SC}(x)}{S\sigma} \tag{9}$$

The equations so far obtained are valid for the system as depicted in **Fig. 1** when the triboelectrification is triggered by a vertical load bringing the layers of dielectrics into contact; yet, as mentioned before, vertical contact-separation is not the only type of motion with the ability to trigger the triboelectrification of the device. The relative motion of the layers of dielectrics along parallel planes can also generate an electric potential difference between the electrodes and this, in turn, can cause electrons to flow from one electrode to the other in a very similar manner to the one described for the vertical contact mode.

In the new motion condition, the system is the same as the one depicted in **Fig. 1**, with the top layer of dielectric material and the electrode attached to it being able to slide under a horizontal load. At time $t_0 = 0s$, the two active layers of the device rest one on top of the other; at time $t_1 = t_0 + \Delta t$, a horizontal load is applied to the top layer of dielectrics/electrode, forcing it to move along the longitudinal direction. As these top strata slide under the application of the external load, charges of opposite sign begin to accumulate on the now exposed portions of the dielectric layers inner surfaces. Same as with the vertical load, the distribution of charges on these exposed surfaces can be considered uniform, with surface densities of σ on the upper dielectric layer and $-\sigma$ on the lower one, as depicted in **Fig. 3**. On the unexposed portions of the dielectric layers inner surfaces, i.e. that region where the two layers are still touching each other, the overall density of charges can be thought of as null because the distribution of positive charges on one surface is balanced by negative charges on the other sitting at atomic-level distances from the first [3]. Similarly to the vertical-load case, as the load is released, the accumulation of charges of opposite sign on the two exposed surfaces of the dielectrics will cause an electric potential difference to be established between the two electrodes of the device. To counter this potential difference, in a non-open circuit condition, charges will be transferred electrode to electrode, until a new static equilibrium is reached, in a short-circuit condition [3]. The cycle will repeat under new loads.

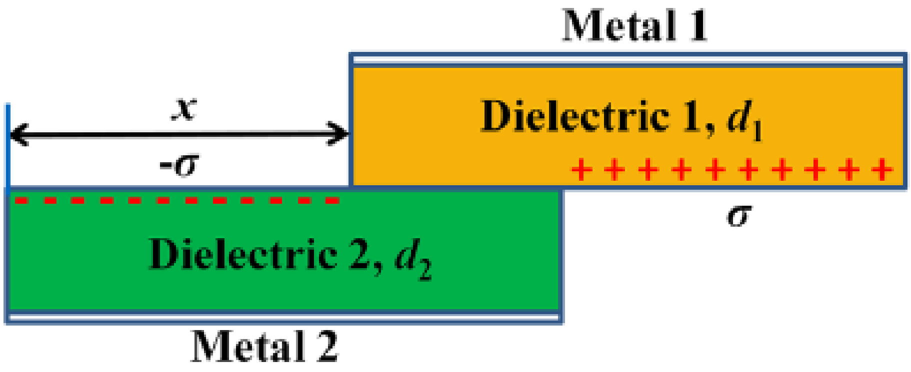

Figure 3: Theoretical model of a sliding-mode TENG. Reproduced from Ref. 29

Having described the triboelectric effect when caused by sliding, it is possible to derive the V-Q-x relationship of **Eq. 1**. In this new condition, the electric potential difference will be inversely proportional to the length of the covered portions of the inner surfaces of the dielectric layers, $l - x$. In particular, using the same definition for the effective dielectric thickness of the device as described in **Eq. 6**, it is possible to obtain the total capacitance of the system under horizontal loads [3]:

$$C = \frac{\epsilon_0 w(l - x(t))}{d_0} \tag{10}$$

where w represents the depth of the triboelectric layers along the z-direction.

The electric potential difference in an open-circuit condition, $V_{OC}(x)$, is given by the following equation:

$$V_{OC} = \frac{\sigma d_0 x(t)}{\epsilon_0 (l - x(t))} \tag{11}$$

Therefore, the V-Q-x relationship becomes:

$$V = -\frac{Qd_0}{\epsilon_0 w(l - x(t))} + \frac{\sigma d_0 x(t)}{\epsilon_0(l - x(t))} \tag{12}$$

where, again, the electric potential difference is given by two terms, one related to the distribution of charges of opposite sign on the exposed surfaces of the dielectric layers, while the other is the screening effect of charge transfer bewteen electrodes in a non-open circuit condition. The same conclusions drawn from vertical contact TENGs can be drawn for sliding contact TENGs: in order to increase the electric potential difference in the device, the surface charge density must be increased and to do so, materials with strong tendencies to gain and lose electrons must be chosen. Moreover, the potential difference is also inversely proportional to the length of the unexposed surface of contact of the dielectric layers; to enhance V it is necessary to reduce $l - x$, or, in other words, to increase the sliding motion of the upper strata along the x-direction. When the displacement of the upper strata equals the length of the strata themselves, the total capacitance of the system will go to zero and in a short-circuit condition electrons will flow from one electrode to the other.

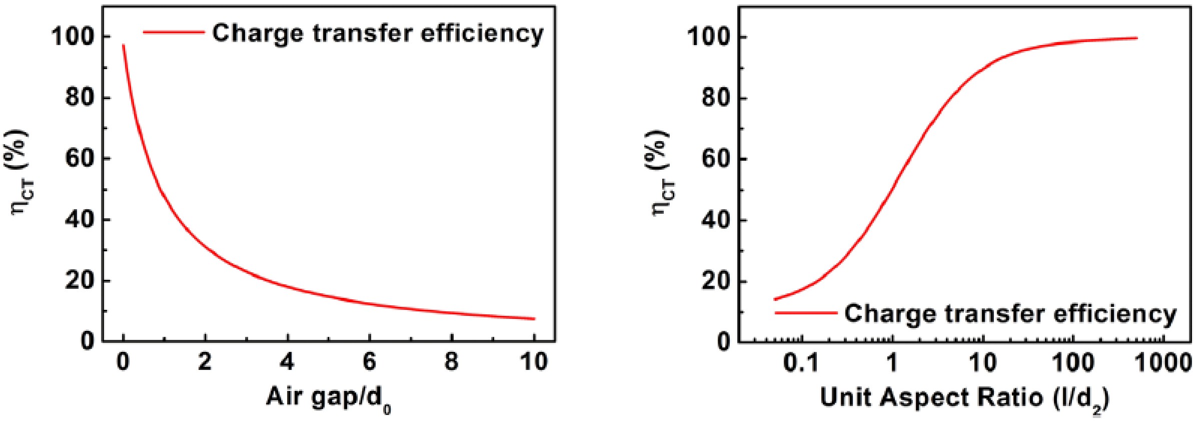

Figure 4: Influence of the air gap and length to thickness ratio of the dielectric layer on the charge transfer efficiency of the device. Reproduced from Ref. 29

The output performances of sliding-mode triboelectric devices are also dependent upon the air gap between upper and lower dielectric layers, in particular, the bigger the air gap in respect to the effective dielectric thickness of the system, the lower the charge transfer efficiency of the device [3]. The dependency of the charge transfer efficiency upon the air gap thickness can be seen in **Fig. 4a**: as evident from this figure, the overall efficiency will go from close to 100 percent to half that value when the air gap to effective dielectric thickness ratio goes from 0 to 1.5; so, in order to build high-efficiency sliding-mode TENGs it is necessary to scale down the air gap between dielectrics. This is in contrast with vertical load-driven triboelectrification, where the output performances of the device were proportional to the separation distance bewteen the dielectric layers, although under short circuit conditions, these devices showed a marked saturation trend in respect with the transferred charges. In particular, in contact-mode TENGs, Q_{SC} reaches 90 percent of the final value,

σS, when the air gap goes from zero to $10d_0$ [3]. A second issue associated with triboelectric devices working under both vertical contact and sliding conditions is the so called "edge effect"; this phenomenon arises when the device has been improperly built, i.e. when the assuption of an infinitely large surface of charge exchange can't be considered valid anymore. In vertical contact triboelectric nanogenerators, this happens when the separation distance x of the dielectric layers is comparable in size with the geometry of the device itself; when this occurs, the edge effect will affect the relationship between the distance x and the potential difference under open-circuit conditions V_{OC}, which will no longer be linear. In sliding-mode TENGs, on the other hand, the edge effect appears when the thickness of the dielectric layers is comparable with the length of the device; this effect hampers the output performances of the nanogenerators, greatly impacting the charge tranfer efficiency for progressively large length to thickness ratios for the dielectric layers, as evident in **Fig. 4b** [3].

1.2.2 Basic structures of TENGs

Having established that triboelectrification in TENGs is consequence of the pressing or sliding of their active layers or a combination of the two under external loads, it is possible to define the four main categories of devices in which triboelectric nanogenerators can be currently classified [3]:

1. *attached-electrode contac-mode triboelectric generators*;
2. *attached-electrode sliding-mode triboelectric generators*;
3. *single-electrode triboelectric nanogenerators*;
4. *freestanding-triboelectric-layer based triboelectric nanogenerators*;

As such, even acknowledging the remarkable flexibility in shapes and forms shown by these devices, it is nonetheless possible to describe their behaviour by using one of the four categories of above. These devices can be further classified into two main categories: dielectric-to-dielectric and conductor-to-dielectric TENGs. As for the attached-electrode contact-mode and sliding-mode TENGs, the dielectric-to-dielectric nanogenerators working principle has been already described in the first part of this chapter, while schemes of their functioning can be seen in **Fig. 2** and **Fig. 3**. Conductor-to-dielectric nanogenerators work similarly to the first ones, the only difference being that one of the two dielectric layers of the device (see **Fig. 1** for reference) has been substituted by a layer of metal. In these configurations, the metal layer has therefore a double purpose: it works both as the conductive material through which the two halves of the nanogenerator create a triboelectric pair in tandem with the other conductive material (dielectrics) and as one of the two electrodes of the nanogenerator. For this reason, in conductor-to-dielectric TENGs, the amount of charges accumulated on the metal layer working as conductor and electrode is the result of both contact electrification under the application of the external load, be it vertical load in contact-mode TENGs or horizontal load in sliding-mode TENGs, and charge tranfer between electrodes via the external circuit.

Considering the other two categories left, single-electrode and freestanding-triboelectric-layer based nanogenerators, the scheme used in **Fig. 1** can no longer be considered valid. These typologies of TENGs were developed in order to account for the relative limited adaptability of contact-mode and sliding-mode TENGs. The greater adaptability of single-electrode and freestanding-triboelectric-layer based TENGs is consequence of their geometry: being as one of the two electrodes is missing, in particular the one corresponding to the moving layer of the nanogenerator, these devices can be used when more compact designs are required or when it is not possible to build devices with a moving electrode. In single-electrode TENGs, the system is compromised of a single layer of dielectric material coupled with a single electrode, working as the tribo-pair of the nanogenerator; a second electrode, which can be placed anywhere, even on the ground, is used as the reference electrode and is connected to the other via an external circuit. Neither one of the two electrodes can move in space, so the triboelectrification of the active pair has to come as consequence of the motion of the only dielectric layer; as with any other typology of TENG, the triboelectrification in single-electrode nanogenerators can be triggered by a vertical load bringing closer the dielectric layer to the in-built electrode, or by a horizontal load displacing the dielectric layer along the longitudinal direction above the in-built electrode. Under short circuit conditions, charges will be transferred from the in-built electrode to the reference electrode. In **Fig. 5** are shown the open-circuit electric potential difference, the short-circuit charge transfer and the charge tranfer efficiency of contact-mode single-electrode TENGs in dependence with the air gap between dielectric and electrode, compared with the same quantities of the system as represented in **Fig. 2**.

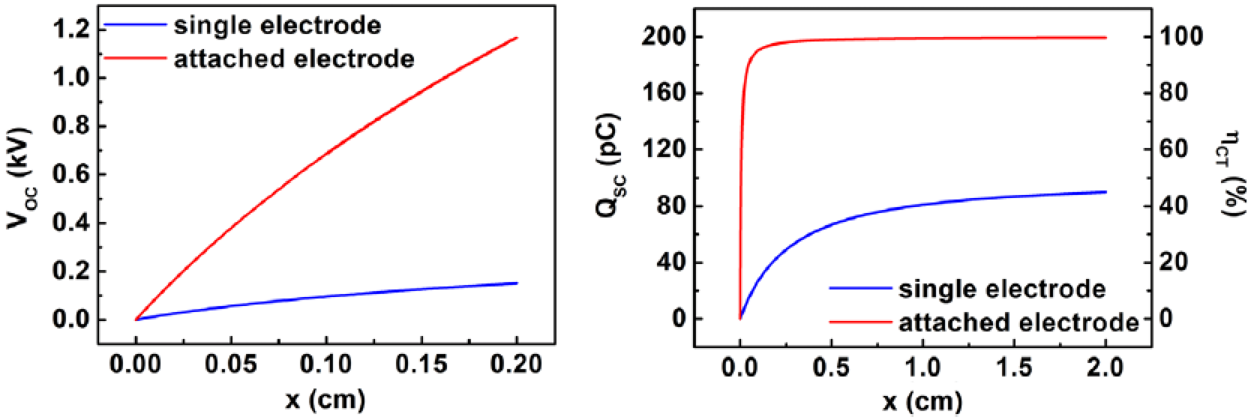

Figure 5: Output performances of attached-electrode and single-electrode TENGs for different values of the separation distance x. Reproduced from Ref. 30

As evident from the figure above, for the same values of the separation distance x of the triboelectric pair layers, attached-electrode TENGs show better performances than single-electrode TENGs along the whole range of the separation distance considered. Particularly significant is the gap existing bewteen the charge transfer efficiencies in the two configurations: while in attached-electrode nanogenerators efficiencies of close to 100% can be reached for very modest separation distances, plateauing almost immediately around the 99 % efficiency value, in single-electrode nanogenerators efficiencies of more than 50 percent can hardly be achieved even for the largest separation distances. In **Fig. 5b** the trends of both charge tranfer efficiency and amount of transferred charges under short-circuit conditions are shown for the two TENGs' configurations. These curves, which are the same for η_{CT} and Q_{SC} for a given nanogenerator, attest the different behaviours also in respect to the saturation values of charge transfer under short-circuit conditions: in attached-electrode TENGs this saturation is achieved almost immediately even for small separation distances x, while in single-electrode TENGs it is only ever reached for the largest air gaps and even then its maximum value is only half as big as the one of the other nanogenerators. As for the open-circuit voltages, the results of **Eg. 4** are confirmed by the (almost) linear tendency exhibited by the curve of **Fig. 5a** in respect to the air gap, in attached-electrode nanogenerators. In single-electrode nanogenerators however, although the overall tendency is similar, the curve slope is markedly smaller as a consequence of large distances separating the dielectric layer from the electrodes, which means that their influence on the electric field distribution on the electrodes is reduced [3].

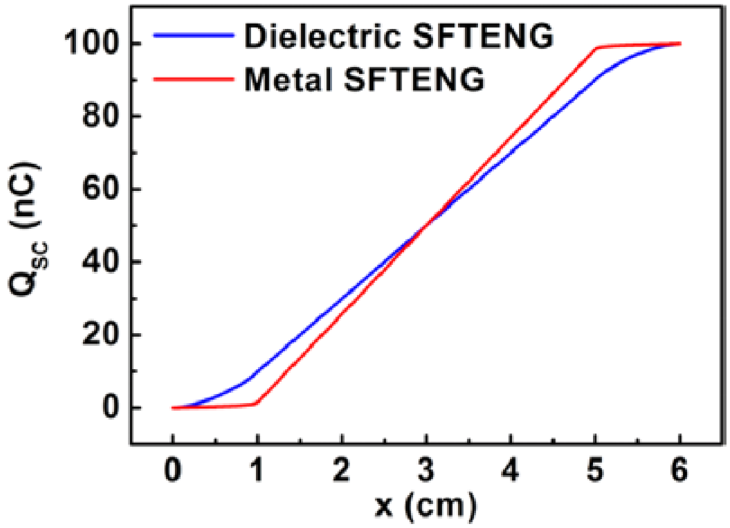

Figure 6: Freestanding-triboelectric-layer based nanogenerators Q_{SC} curve. Reproduced from Ref. 31

Finally the freestanding-triboelectric-layer based nanogenerators were developed in order to circumvent the problems associated with the electrostatic shield effect wich affect the output performances of single-electrode TENGs. This last category of triboelectric nanogenerators can work under vertical load contitions, in which case they present a contact-mode-like behaviour, as well as under horizontal load conditions, in which case a sliding-mode-like behaviour is shown by the device. Again, for these nanogenerators, dielectric-to-dielectric designs or conductor-to-dielectric designs can be used to achieve electrification. Their working principle is similar to regular contact-mode and sliding-mode TENGs, the main difference being that just like single-electrode nanogenerators, freestanding-triboelectric-layer based nanogenerators can function with the moving part of the device not directly connected to the electrodes [3]. Still, their output performances are closer to those of attached-electrode contact mode and sliding mode TENGs rather than single-electrode TENGs. The open-circuit voltage, in particular, shows the same linear dependency on the separation distance as the attached-electrode nanogenerators under contact-mode conditions. The short-circuit charge transfer however, does not exhibit a saturation trend but, instead, it shows again a linear dependency upon the separation distance x [3]. In **Fig. 6** is represented the Q_{SC} curve function of the air gap thickness for dielectric-to-dielectric and conductor-to-dielectric nanogenerators.

It is now possible to compare the performances of the four main categories of triboelectric nanogenerators. For this purpose, Yunlong Zi et al. developed a parameter called the *figure of merits of TENGs* which, regardless of the mode or size of the single device, can help assess the merits of each nanogenerators in regard to open-circuit voltage, short-circuit charge transfer, charge transfer efficiency and power output. The Figure-of-merits parameter is obtained under short-circuit conditions, when the charge transfer reaches its maximum value of Q_{SC}; the maximum output energy per cycle is proportionate to the open-circuit voltage and to the maximum electric potential difference under short-circuit conditions [4]:

$$E_m = \frac{1}{2}Q_{SC}(V_{OC} + V_{max,SC}) \tag{13}$$

Under these conditions, the average output power and the energy-conversion efficiency are given, in turn, by the following equations [4]:

$$P = \frac{E_m}{T} = \frac{vE_m}{2x_{max}} \tag{14}$$

and

$$\eta = \frac{E_{out}}{E_{in}} = \frac{1}{1 + \frac{1}{\frac{E_m}{2Fx_{max}}}} \tag{15}$$

where v represents the average velocity of the moving part of the device while F represents the average dissipative force acting on the device when this is in function. From this it becomes apparent how the output power and the energy-conversion efficiency alike are dependent on the E_m/x_{max} ratio; then, recalling the results of **Eq. 4** and **Eq. 8**, it becomes apparent that voltage and charge transfer alike are proportional to the surface charge density σ. The $V_{max,SC}$ is also proportional to the charge density, so the maximum energy output per cycle has to be proportional to its square value. The structural figure of merits of TENGs can therefore be expressed as a function of the maximum energy output, divided by the area of the charge exchange surface as to make the parameter dimensionless [4]:

$$FOM_S = \frac{2\epsilon_0 E_m}{\sigma^2 A x_{max}} \tag{16}$$

and from this equation, the performance figure of merits of TENGs:

$$FOM_P = \sigma^2 FOM_S \tag{17}$$

With these parameters at hand, it is possible to compare the output performances of each category of triboelectric nanogenerators regardless of their dimensions or the mode of motion which triggers their triboelectrification.

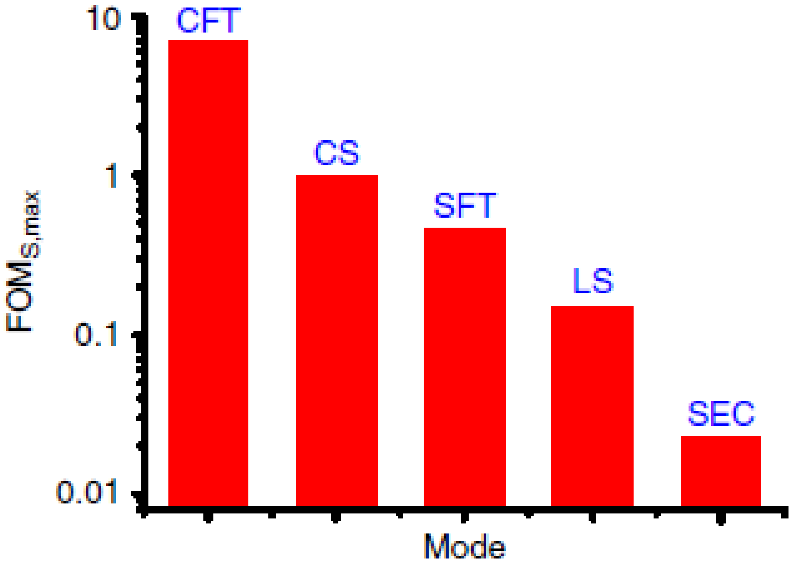

Figure 7: Figure of merits for the main categories of TENGs. Reproduced from Ref. 4

In **Fig. 7** the values of the FOM_S parameter are plotted for each category: contact-mode freestanding-triboelectric layer-based TENGs show the best results. This is because these nanogenerators present reduced capacitances between the electrodes and this property results in increased electric potential differences established in the device. Moreover, since these nanogenerators have a single dielectric layer moving bewteen the two electrodes, the induced triboelectrification on both sides of the dielectric stratum boosts the device capabilities of transferring charges between electrodes, resulting in increased Q_{SC} as compared with other kinds of triboelectric nanogenerators [4]. Attached-electrode contact-mode TENGs come second, while sliding-mode freestanding-triboelectric layer-based TENGs and attached-electrode TENGs come right after them, proving that contact separation is a better way to trigger triboelectrification in comparison with the sliding motion. Single-electrode contact separation TENGs come last, owing to their smaller voltages, transferred charges as well as lower charge transfer efficiencies as mentioned before [4].

1.3 Triboelectric nanogenerators as deformation sensors

In the first parts of this chapter a brief overview on triboelectric nanogenerators was given, illustrating the way these devices convert mechanical energy from the environment into electric energy, explaining how they do so with very high conversion-efficiencies and cataloguing them based on their working principle and their designs. The V-Q-x relationship of **Eq. 1**, which is valid for any triboelectric nanogenerator, is key into understanding the vast range of possible fields of applicability of TENGs. One such field of applicability is sensing deformation in objects under external loads, for example, in self-powered wearable electronics [7]. Specifically, the linear proportionality of the open-circuit voltage V_{OC} on the separation distance x can be used to estimate the deformation caused by an external load acting on the object to which the nanogenerator is attached. To this purpose, it becomes useful to utilise the capacitive behaviour of triboelectric nanogenerators mentioned in the first part of this chapter. When describing the way TENGs work, the assumption of infinitely large surfaces of charge exchange was made as compared with the thickness of the dielectric layers, of the air gap between them and of the two electrodes attached to each dielectric material; this assumption is what makes it possible to consider the charges on each surface of the two dielectric layers to be uniformly distributed after contact. Uniformly distributed charges also means costant electric potentials on the two opposing inner surfaces of the tribo-pair, which can be consequently thought of as nodes of the electrostatic system, where a node, in this context, is a surface or a volume characterised by the same electric potential [3]. Given that the electrodes also have the same electric potential throught their volumes, they can be also thought of as nodes of the system. So, a triboelectric nanogenerator such as the one depicted in **Fig. 1** can be represented by four nodes in total, one node per dielectric layer and one node per electrode. An equivalent capacitance is formed between two nodes when the electric field lines connecting them are not screened by the field lines connecting other nodes [3]. Again, considering the system of **Fig. 1**, owing to the infinitely large inner surfaces of the dielectric layers, the field lines connecting the two nodes corresponding to the two dielectric materials completely block the field lines connecting the two electrodes, so that the system can be represented by three equivalent capacitances: two for each dielectric layer and one for the air gap between them [3]. In a conductor-to-dielectric nanogenerator, being missing one of the dielectric layers, the number of equivalent capacitors will be two, as depicted in **Fig. 8**.

For the triboelectric device of **Fig. 8**, the transferred charges from the two electrodes (node 1 and node 3 in the figure) under short-circuit conditions can be obtained by using the equivalent capacitances of the system [3]:

$$Q_{SC} = \frac{S\sigma}{1 + C_1(x)/C_2(x)} \tag{18}$$

Obviously, the value of Q_{SC} calculated through this equation has to match the results of **Eq. 8**. As for the open-circuit voltage between electrodes, recalling **Eq. 3**, it can be expressed as:

$$V_{OC}(x) = \frac{Q_{SC}(x)}{C(x)} \tag{19}$$

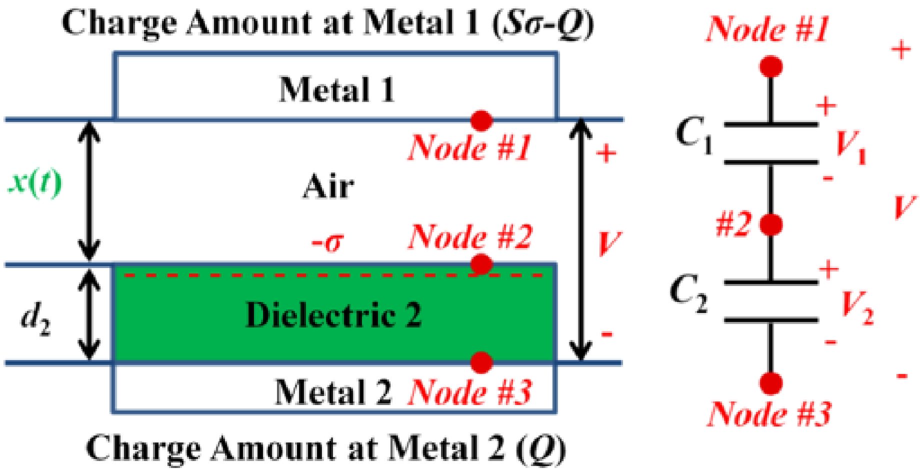

Figure 8: Eqivalent capacitances of a conductor-to-dielectric attached-electrode TENG. Reproduced from Ref. 28

where $C(x)$ is the total equivalent capacitance of the system, which, for the capacitors in series of **Fig. 8**, is the sum of each capacitance. It is possible to measure the deformation of the device under external loads by evaluating how each equivalent capacitance between two nodes varies as the separation distance x varies. A reference state is used for which the electric potential difference between electrodes measured with an electrometer is set to zero [8]. Any subsequent variations of the separation distance x under extarnal loads will affect each capacitance of the system, resulting in different values of the electric potential difference measured at the electrodes with the electrometer. Still, considering a system such as the one of **Fig. 8**, when the separation distance is zero, i.e. when the dielectric material touches the top electrode, the first capacitance C_1 will be infinite while the second capacitance C_2 will be a finite number. The tranferred charges under short-circuit condition will therefore be zero or, in other words, there won't be any charges at node 3 [3]. When the separation distance is sufficiently large, C_1 goes to zero while C_2 does not change. In these conditions Q_{SC} reaches its saturation value $S\sigma$ and the amount of charges at node 3 will correspond precisely to the saturation value of Q_{SC} [3]. As x goes from these two extremes, the amount of transferred charges changes, so does the open-circuit voltage and so does the electric potential difference as obtained in **Eq. 1** at the two electrodes, measured with the electrometer.

Using this concept, Aifang Yu et al. developed a conductor-to-dielectric TENG sensor. A probe is connected to a the upper layer of a conductor-to-dielectric triboelectric nanogenerator working under contact-separation mode, same as the one depicted in **Fig. 8**. The probe axis is perpendicular to the parallel planes on which sit the different layers of the nanogenerator. When a moving object touches the probe, it forces it to bend accordingly to the direction of motion of the object itself. As it bends, the probe acts on the upper layer of the nanogenerator to which is connected: the hemiplane of the layer on which sits the projection of the deformed probe is tilted down, while the other hemiplane of the layer is tilted up, as shown in **Fig. 9** down below.

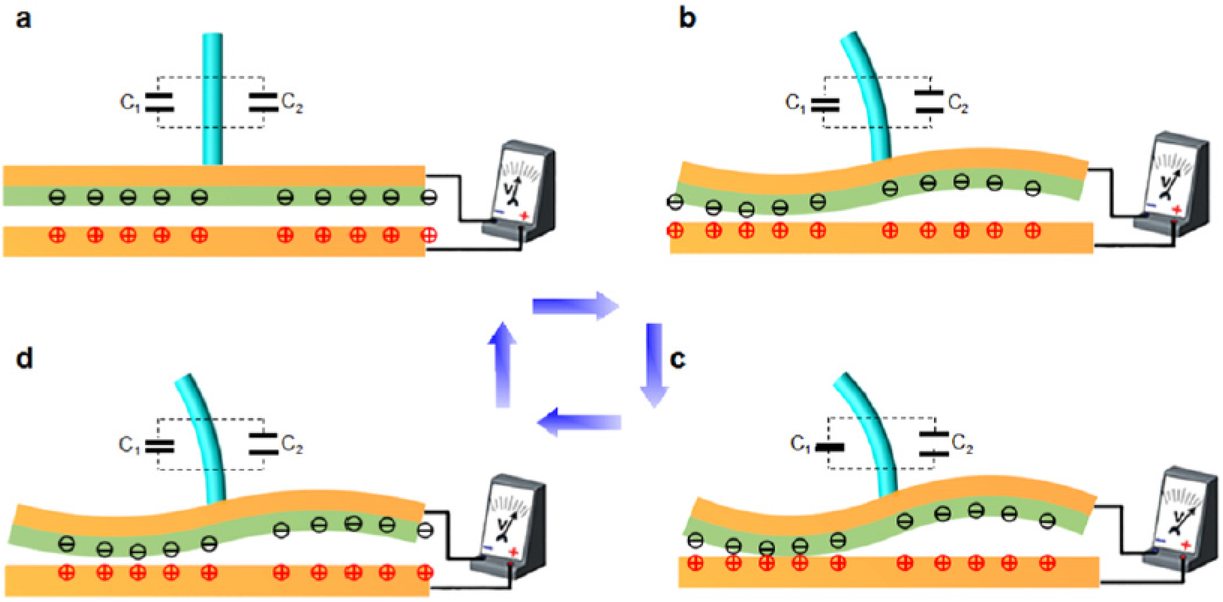

Figure 9: Scheme of a conductor-to-dielectric TENG deformation sensor. Reproduced from Ref. 8

The upward and downward motions of the two hemiplanes trigger contact electrification on the inner surfaces of the triboelectric pair and this, coupled with electrostatic induction, creates a potential difference between the two electrodes. The equivalent circuit of the system so far described consists of two capacitors connected in parallel. At $t_0 = 0s$, the system is in the configuration depicted in **Fig. 9a**. The open-circuit output voltage is proportional to the separation distance $x(t_0)$ [8]:

$$V_{OC}(x) = \frac{Q_{SC}(x)}{C_1(x) + C_2(x)} = \frac{\sigma x(t_0)}{\epsilon_0 \epsilon_r} \tag{20}$$

When the probe is bent under an external load, the upper layer of the triboelectric nanogenerator is forced to buckle. The equivalent capacitance of the system changes; in particular, the capacitance corresponding to the tilted-down hemiplane is reduced in respect to its value in the undeformed configuration, while the capacitance corresponding to the tilted-up hemiplane is increased. If the probe bending is great enough for the dielectric layer to touch the lower electrode on the tilted-down hemiplane, charge neutralisation will occur on the interface between the inner surfaces of the tribo-pair, and the equivalent capacitance will go to zero [8]. At $t_1 = t_0 + \Delta t$, in **Fig. 9c**, the dielectric layer and the lower electrode are directly in contact with one another; the corresponding capacitance C_1 is null and only the right half of the triboelectric nanogenerator contributes to the output electric potential difference of the system [8]:

$$V'_{OC}(x) = \frac{Q_{SC}(x)}{C'_2(x)} = \frac{\sigma x(t_1)}{\epsilon_0 \epsilon_r} \tag{21}$$

When the external load is released, the probe goes back to its initial position, **Fig. 9a**, and so do the two capacitances and the output voltage, going back to their original values.

To set a reference state, it is convenient to use the undeformed position of the probe, to which is to be associated a 0 V value of the electric potential difference, between electrodes, as measured with an electrometer. Any subsequent deformation of the probe will result in an offset of the measured voltage on the electrometer from this reference state. The open-circuit voltage measured on the electrometer will increase as the separation distance between the tribo-pair increases, until it reaches its maximum value. This means that there exists a limit beyond which it is not possible to continue to bend the probe via an external load. Moreover, the sensitivity of the triboelectric sensor is directly correlated with the dimensions of the probe; Aifang Yu et al. found that smaller probes make for more sensitive sensors, but at the same time, they also found that excessively small probes show fast saturation trends for the open-circuit voltage, thus making it difficult to measure the deformation of the probe beyond this point of saturation.

1.4 A brief introduction to soft robots

Soft robots are a particular kind of robots specifically designed to mimic the mechanical properties of soft bodied animals, such as the octopus. To achieve this, they are usually built in highly compliant materials, like gels, silicone rubber or generic elastomeric materials which grant them greater fluidity of movements as well as higher structural flexibility when compared with the more common rigid robots currently employed. In order to imitate the mechanical properties of these soft bodied animals, the majority of soft robots work as pneumatic actuators: their geometry is characterised by hollow structures, working as inflating air chambers, connected to the exterior and to one another through air channels. Owing to the high compliancy of the materials with which these actuators are commonly built, when a pressurised fluid is forced inside the actuator via a pipe connected to the air channels, the mounting pressure inside the chambers causes the material to strain. This deformation mostly impacts the thin walls of the soft robot chambers, whose volumes greatly increase as the pressure inside them increases. In order for the actuators to work, it is therefore necessary to control the high strains to which the chambers walls are subjected during inflation, by reducing the volume of the fluid pumped into the chambers during the working phase or by either varying the walls thickness or the chosen material during the design phase. As a consequence of the augmented volume of the chambers, the actuator bends, allowing it to move, in some applications, under alternating cycles of inflation and deflation.

The soft robots motion is achieved by creating areas of different deformations in their body. Generally, to do this, a strain limiter is embedded inside the actuator. The soft robot can be divided in two parts, one corresponding to the inflatable chambers and one corresponding to the portion of its body where the strain limiter has been implanted. When a fluid is pumped into the chambers, it forces them to increase in volume resulting in the deformation of the robot; the strain limiter, being stiffer than the material with which the actuator is built, prevents the part surrounding it to deform to the same extent as the chambers. This different behaviour of the actuator, assuming that the strain limiter sits at the lower half of the robot while the chambers part consitutes the upper half of the robot, prompts a downward bending of the actuator. By controlling the strain rate, and with it the rates of inflation and deflation of the chambers, it is possible to control the motion of the robot itself.

The properties of soft robots so far described, make them very interesting in those fields of application where precision of movements is required. Their great flexibilities also allow them to perfectly adhere to an object, possibly to insure good gripping if need be. Moreover, the possibility of controlling the rate of deformation and strain of the actuator allows them to take hold of object which normal robots are not able to. This means that soft robots can be used where rigid robots cannot, for example, when dealing with delicate objects. To this purpose deformation sensors are essential in ensuring the correct strain rate and the correct overrall deformation of the robot, especially when dealing with delicate objects. In this context, it is therefore possible to use triboelectric nanogenerators powered sensors to measure the deformation of the body of the robot in order to properly control its behaviour during the working phase. As already mentioned, most soft robots are of the pneumatic kind, where a pressurised fluid is pumped into its chambers prompting a variation in volume of the chambers themselves; this, coupled with the presence of a strain limiter, for simplicity's sake placed at the lower half of the robot body, creates areas of different deformation which cause the robot to bend and even crawl under successive cycles of inflation an deflation. An imbedded triboelectric sensor could be inserted precisely where the strain limiter commonly sits; this way, the active layers of the triboelectric sensor will carry out a double purpose, forming the tribo-pair with which to trigger the electrification of the device under the external load and acting as the strain limiter of the robot.

As a matter of fact, in the last part of the previous subchapter it was described how triboelectric sensors can correlate the electric potential difference measured at the two electrodes with the separation distance between the tribo-pair of the triboelectric device. Using this property it becomes apparent how the use of triboelectric sensors can be implemented in soft robots to measure the deformation caused by inflation. A reference state must be set, for simplicity, corresponding to the undeformed configuration. When air is injected into the robot chambers via a pipe, the chambers walls start to strain and the chambers volume increases. The presence of the strain limiter, in this case the triboelectric sensor, limits the deformation at the base and consequently the robot bends downward. As the robot bends, the active layers of the triboelectric device get closer, prompting a variation in the voltage as measured with an electrometer. At different stages of the inflation process, the electrometer will measure different electric potential differences at the electrodes, directly correlated with the amount of pressure exerted over the triboelectric sensor. Since soft robots are not particularly large in dimensions, very sensitive triboelectric sensors are necessary to correctly measure the voltage associated with the strain on the robot. In such a configuration, contact-separation mode triboelectric sensors could represent the most suitable choice.

1.4.1 Deformation in soft robots

To have a measure of the bending the soft robot is subject after its chambers have been inflated, it is first necessary to evaluate the pressure increase inside the air chambers when said air is pumped into the device. For the sake of simplicity, the study will be done considering a single chamber, as they are all geometrically identical. Therefore, assuming that an ideal gas approximation is good enough for air and given that inflation can be assumed to be an isothermal transformation and recalling the ideal gas law for an isothermal process, it is possible to write that:

$$pV = const \tag{22}$$

When injection is achieved via a syringe that draws air directly from the environment and pumps it right into the air chambers of the device, the flow of air injected can be assumed to be at atmospheric pressure, thus not pressurised. At $t_0 = 0s$, when the robot is still in its undeformed configuration, the pressure inside its air chambers can be also assumed to be equal to that of the ambient. After inflation the volume of the chambers increases but not enough for the pressure inside them to stay constant, which will therefore also increase. The equation of above can be rewritten as:

$$p_0V_0 = p_1V_1 \tag{23}$$

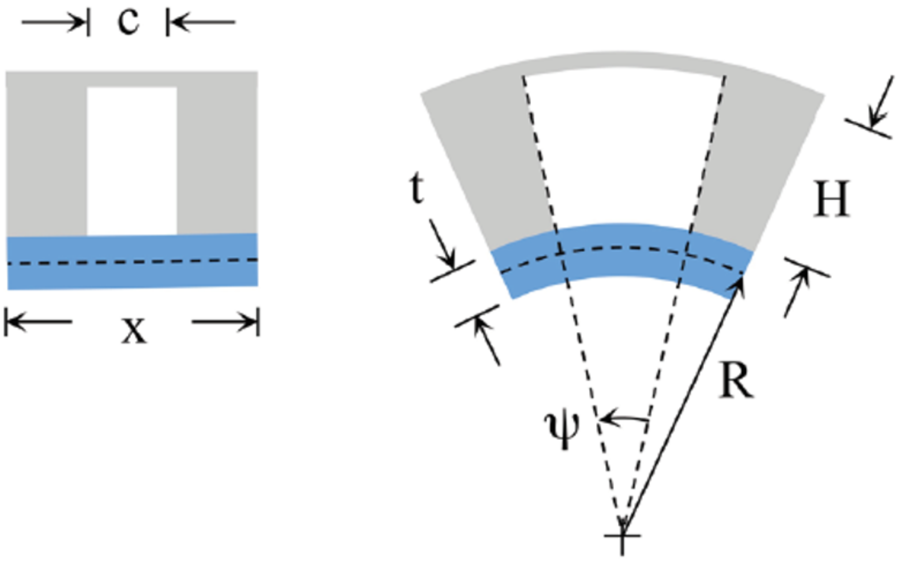

Figure 10: Robot air chamber before and after inflation. Reproduced from Ref. 9

Pressure inside the chambers causes the robot to deform and bend, with the bending curvature being directly dependent upon said pressure. Moreoever, the flow of air inside the chambers also affects the flexural rigidity, D, of the silicone rubber of the robot body [9]. The potential energy of both the enclosed air and the elastomer (polydimethylsiloxane), in the absence of an external moment is given by the following equation [9]:

$$\Pi = \frac{1}{2}Dk^2x - pV \tag{24}$$

In this equation, the curvature is assumed to be constant along the whole length of the strain limiting layer placed at the bottom of the robot body. To explain why, it is necessary to consider the trend of the bending moment at any given section of the device. In soft robots, since the neutral axis does not correspond to the axis of vertical symmetry, a bending momentum arises. Assuming that the robot in question can be approximated in its behaviour by a beam in deflection, the bending curvature can be obtained by the following relation:

$$k = \frac{\partial^2 v}{\partial x^2} = -\frac{M}{D} \tag{25}$$

where v represents the beam's deflection and M represents its internal bending moment. At any given section of the robot, this bending moment does not change, being only function of the vertical position of the neutral axis. As for the flexural rigidity of the device, this is given by the mechanical properties of the material, i.e. Young's modulus, and by the geometric properties of the cross section, i.e. its area moment of inertia:

$$D = \frac{Ewt^3}{12} \tag{26}$$

And being both the bending moment and the flexural rigidity of the strain limiter constant in respect to x, it must be that the bending curvature k of the robot is constant too. Having established this and going back to the results of **Eq. 24** it can be noted that for the static equilibrium of the system, the potential energy has to be stationary with respect to the bending curvature of the robot [9]:

$$\frac{\partial \Pi}{\partial k} = 0 \tag{27}$$

Considering now the bent condition for the robot as the one depicted on the right in **Fig. 10**, the volume of the air chamber of **Eq. 2** can also be expressed as a function of the curvature [9]:

$$V \approx \frac{1}{2}\psi \left[(R + H)^2 - R^2 \right] w \tag{28}$$

where, from **Fig. 10**, $\psi = c/R = kc$ is the angle of the arclength c along the strain-limiting layer, R is the bending radius (reciprocal of the bending curvature k) and w and H are respectively the chamber width and height. With these equations at hand and considering the stationarity of the potential energy with respect to k, as previously justified, it is possible to measure the bending curvature of the chamber when the pressure p is applied to its walls by the flow of air as [9]:

$$k_p = 6\frac{pcH^2}{Ext^3} \tag{29}$$

And the corresponding chamber volume can be rewritten as [9]:

$$V_1 = \frac{1}{2}k_p c \left[\left(k_p^{-1} + H \right)^2 - k_p^{-2} \right] w \tag{30}$$

Same as with the curvature, the flexural rigidity is also dependent upon the mounting pressure inside the air chambers, as already anticipated at the beginning of this subchapter. In particular, when there is no pressurised fluid inside the device, the flexural rigidity of the system almost corresponds to that of the sole strain limiter; when pressurised air is pumped into the device, though, the new flexural rigidity, D_p which is a function of the pressure of the flow of air, is given by the following equation:

$$D_p = \lim_{M \to 0} \frac{M}{\Delta k} \tag{31}$$

where M is an externally applied bending moment which prompts the change in the bending curvature, Δk from the k_p value estimated with **Eq. 29**. Of course, the application of an external moment has to be included in the formulation of the minimum potential energy principle of **Eq. 24**, which therefore becomes [9]:

$$\Pi = \frac{1}{2} D k^2 x - p V_p ln \left(\frac{V}{V_p} \right) - Mkx \tag{32}$$

Again, considering, for the static equilibrium, that the potential energy is constant with respect to the bending curvature of the robot, it is possible, in turn, to evaluate the curvature itself in this new configuration using Taylor expansion about $M = 0$ through the following equation [9]:

$$k \approx k_p + \frac{6M}{w} \left[\frac{1}{Et^3} + \frac{x}{6cpH^3 + Et^3 x} \right] + O(M^2) \tag{33}$$

whence the flexural rigidity can be expanded as:

$$D_p = \lim_{M \to 0} \frac{M}{\Delta k} = \frac{Ewt^3(6cpH^3 + Et^3 x)}{12(3cpH^3 + Et^3 x)} \tag{34}$$

or, using another Taylor expansion about $p=0$ [9]:

$$D_p \approx D + \left(\frac{cH^3 w}{4x} \right) \tag{35}$$

The results of **Eq. 33** and **Eq. 29**, which refer, respectively, to a system where an external bending moment has been applied to the robot and to a system where no such external moment exists, are obtained for a single air chamber of the soft robot. As mentioned above, though, since the robot is built with air chambers identical to one another and since the limiting strain layer extends to the whole length of the robot body, it is possible to extend the results of **Eq. 33** and **Eq. 29** from the single i-air chamber to the n-air chambers which constitute the device.

For the use intended in this work for the soft robot, the inflation of the chambers is achieved via a syringe which draws air from the environment and injects it into the device at a pressure which is close to the atmospheric pressure of the environment itself. In a system such as this one, which uses unpressurised air as the inflating fluid, there are no bending moments that are applied to the robot from the exterior. The bending curvature is thus given by **Eq. 29**, the volume of the single air chamber after inflation is given by **Eq. 30** and the potential energy of the system is given by **Eq. 24**.

1.5 An introduction to the next chapters

In this chapter an overview on triboelectric nanogenerators/sensors and soft robots was given, including a general description of their respective working principles and a general outlook to their possible future applications. As mentioned in the abstract, the objective of this work is to embed a triboelectric device inside a functioning soft robot. The triboelectric device, working as a deformation sensor, is used to evaluate the deformation of the robot when this is inflated: by measuring the electric potential at its electrodes through an electrometer, the triboelectric sensor can indirectly give an indication of the extent of the deformation of the robot. The work is divided into two parts: experimental testings and computer-aided simulations. In the second chapter, is a description of the design and building processes for the soft robots and for the robot-embedded triboelectric devices, including the various failed attempts to build soft robots in highly compliant materials, such as the Ecoflex silicone rubber mixture. In the third chapter is the creation of the COMSOL model with which to simulate the behaviour of the robot-embedded triboelectric device, along with the enunciation of the fundamental equations and variational formulation for the electrostatic problem. Finally in the last chapter are reported the testing results and the simulation results.

2 Soft robots and triboelectric nanogenerators

2.1 Introduction

In the previous chapter it was described how triboelectric nanogenerators only need two modes of motion for their active layers, vertical contact-separation and lateral sliding, in order to convert mechanical energy from the environment into electric energy. These simple modes of motion can be the results of either a direct or indirect external stimulus acting on the device, so long as the stimulus produces a displacement of the active layers of the device necessary for the electric potential build-up between its two electrodes and the consequent current flow between the two. This property, i.e. the ability to generate an electrical output from indirect external loads, is particularly useful when the device is used to sense the external stimuli acting on the system, as is the case with triboelectric sensors. Given that the purpose of this work is to investigate whether it is possible to use these devices as deformation sensors for soft robots, it becomes necessary to find a way to insert a functioning sensor into the robot body without reducing the ability of the robot to operate as it was intended to. In this chapter are the various steps followed into building a functioning triboelectric sensor embedded into the body of a soft robot, starting from the choice of material for the soft robot body and from the geometry of the triboelectric sensor. Given the characteristics of the system, only the simplest geometries are considered for the sensor, such as the one depicted in **Fig. 2** and **Fig. 8**, as to insert with ease the sensor into the soft robot body and to not excessively increase the overall stifness of the robot with too thick of a triboelectric sensor. The choice of materials for the sensor As for the soft robot, the geometry adopted is one very tipical for the most common type of soft robots, pneumatic actuators.

2.2 Building the soft robots

The first step in building a triboelectric sensor-embedded soft robot is finding the right material for the soft robot body. As already mentioned, due to their high compliances, elastomeric materials represent the most common choice for these kinds of actuator. In this project, soft robots were built in silicone rubber, owing to its mechanical properties, its weight, its ease of use and ease of processing. Two different mixtures of silicone rubber were used: initially the soft robot was built in the Ecoflex mixture, while afterwards it was built in the Mold Star mixture. As declared by their manufacturer, the mechanical properties of the two mixtures are the following [11]:

Mechanical property	Ecoflex	Mold Star
Relative density	1.07 g/cm^3	1.18 g/cm^3
Tensile Strength	1.4 MPa	2.8 MPa
100% Modulus	0.07 MPa	0.38 MPa
Elongation at break	900%	440%
Tear Strength	6655 N/m	15411 N/m

As evident from the table above, Ecoflex soft robots are lighter and present significantly higher elongations at break than Mold Star robots, while these other robots, on the other hand, are more than twice as tear-resistent, have higher tensile strengths and higher 100% Moduli. In many applications, pneumatic soft robots experience severalfold increases of their volumes, resulting in high strains on the material, which are particularly accentuated on the chambers walls. Moreover, having cycles of inflation and deflation in succession means that soft robots work under fatigue conditions, severely reducing their life spans [10]. All these issues limit the adoption of excessively compliant materials, on which wall tearing could become too problematic. As a matter of fact, the Ecoflex silicon rubber, which present good flexibility and low tear resistance, has proved to be not particularly suited for this particular kind of applications as will be described in the following sub-chapter. The Mold Star silicone rubber, on the other hand, has proved to be more apt to the project scope although this material too came with its very own issues, as will be described in a while.

2.2.1 Ecoflex robots

The first soft robots assembled were built in the Ecoflex silicon rubber mixture. The geometry of these robots was directly taken from the website *softroboticstoolkit.com*, from an already existing pneumatic actuator. The robot thus obtained is made of two parts, an upper part corresponding to the chambers plus the air channels connecting them and a lower part corresponding to the base of the robot; between the two is the strain limiter. In the undeformed configuration, the robot dimensions are as follows:

- 112 mm x 15 mm for the surface at the base;
- 18 mm for the robot height;
- 6 mm x 11 mm x 15 mm for the inner volume of the air chambers;
- 2 mm x 2 mm x 4 mm for the air channels volume;
- 1 mm for the thickness of the chambers walls.

The robot is assembled by mixing a 1:1 ratio of the two parts of the Ecoflex mixture, mixture which is then poured into a mould where it is left to cure for about 4 hours. The two-case mould used to build the soft robot is shown in the images above, drawn with the software Solidworks, and then printed with a 3D printer in PLA (polylactide). The strain limiter used for this actuator is a common paper sheet. To build the robot, these steps were followed:

- 40 g of mixture are prepared by mixing parts A and B in a 1:1 ratio;
- the mixture is then poured into the two cases;
- a sheet of paper, cut in the same dimensions as the inner surface of the base case, is placed on top of the mixture of the base case;
- the mixture is then left to cure for four hours, after which time the upper part of the robot is extracted from its case, while the lower part is left inside its own case;

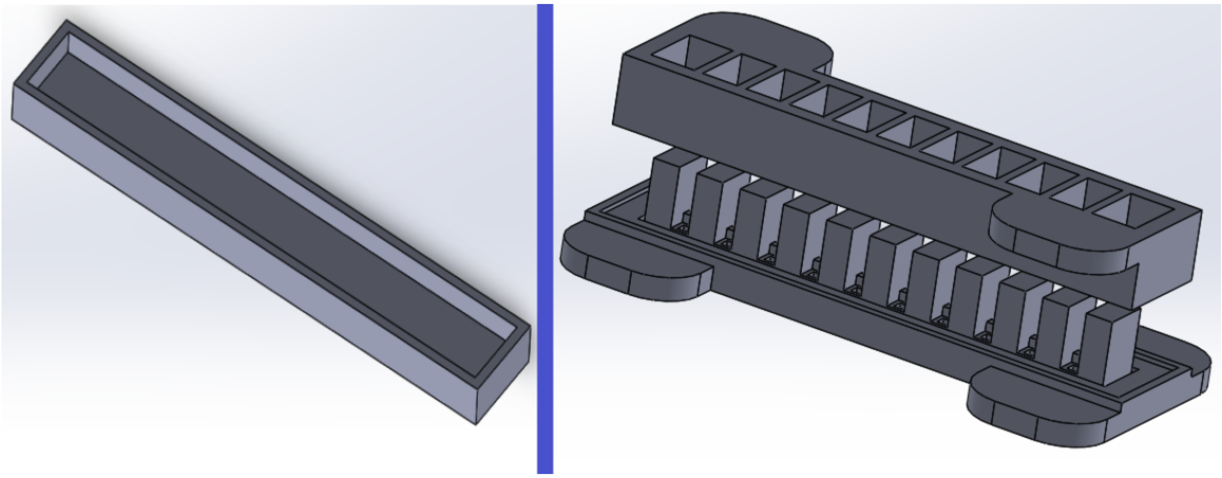

Figure 11: Base case and chambers case of the mould.

- an additional 10-gram mixture is prepared to be used as the connecting stratum of the two parts of the robot body;
- these additional 10 grams are poured right on top of the still-encased base, completely covering the paper sheet;
- at this point, the upper part of robot body is placed above this fresh mixture and gently pressed to ensure good binding between the two parts
- the mixture is then left to cure for additional four hours.

In **Fig. 13** a picture of the Ecoflex robot.

The soft robots built using such moulds dont have an in-built pipe cavity to account for the rubber tubing with which to pump air inside the chambers. On the contrary, in order to inflate the robot, it is first necessary to tear a small hole right in the middle of the out-facing wall of one of the two external chambers, (see **Fig.14** for reference). The air pipe is then forced-in into the hole, but no other measures are adopted to properly seal the tubing, resulting in the emergence of air leaks during inflation. Other than this design mishap, the Ecoflex prototype came with several other flaws. Since the mixture, in these first attempts, didn't go under any cycle of vacuum pumping to eliminate excess air, the finished robot presented an extremely high amount of air cavities throughout its whole body. Being as the actuator was completely covered with air bubbles, it was impossible to properly inflate its air chambers as the air that was being injected via the pipe escaped through these very cavities. This was especially accentuated near the base of the air chambers, due to the geometry of the mould which made it more difficult for the mixture to properly fill it, resulting in a greater density of air cavities compared with other parts of the robot body. Therefore, every time a new robot was built using the Ecoflex silicone rubber, some additional mixture had to be prepared in order to fill every air bubbles present on the surface. This, in turn, meant that before testing the robot it was necessary to wait for the rubber in the freshly filled cavities to cure, adding even more time to the already lengthy process.

Figure 12: The Ecoflex mixture curing inside the chambers case.

Figure 13: The Ecoflex silicone rubber soft robot. This prototype is missing the air-pipe used for air injection

Yet even with this precaution, the air leak problem represented itself after several cycles of inflation, mostly because the air bubbles surfacing on the inner walls of the chambers could not be properly dealt with. As a matter of fact, even if air could not escape through these inner cavities as they were not connected to the outer surface of the robot, their presence inside the chambers still hindered a correct inflation of the actuator after several cycles. This was mostly due to the elastic properties of the chosen material (Ecoflex). The high compliancy of the Ecoflex silicon rubber leads to significant deformations of the robot, with the air chambers more than doubling in size at each inflation; this, coupled with thin chamber walls, caused the tearing of the walls themselves, being this material particularly low tear-resistant. Now, while the air bubble problem on the exterior walls could be addressed by pouring-in more material, the tearing of the chambers could not be solved in any way other than reducing the amount of air injected into the chambers. At the same time though, pumping lower volumes of air during inflation could only delay the issue from occurring, which indeed represented itself after a handful of cycles of inflation and deflation. As the first tearing appeared on one of the chambers walls, the robot had to necessarily be discarded. All these limitations made it impossible to embed a triboelectric sensor inside the Ecoflex robot.

2.2.2 Mold Star robots

To circumvent this issue, the Mold Star silicone rubber was chosen as the next material with which to build the robot. Being stiffer, this material offers better mechanical properties, in particular higher tensile strength and tear strength, as compared with the Ecoflex silicone rubber; properties which reduce the deformation of the chambers after inflation, thus preventing wall tearing. Still, this new robot came with its own flaws. Uncured Mold Star mixture is more viscous than Ecoflex, so properly filling the mould becomes more difficult. Thus, with this new mixture, bigger and more frequent air bubbles formed at the base of upper case of the mould, right where the geometry becomes more complex. Consequently, while wall tearing is basically solved thanks to its mechanical properties, the air bubble problem becomes even more accentuated. To address this issue, a vacuum pump was then used: the uncured silicon rubber is subjected to two cycles of vacuum pumping, one when the mixture is still inside the mixing cup, to eliminate most of the air, and a second one when the mixture has been poured inside the two cases of the mould. In the first cycle, once ensured that the mixing cup is not filled to the brim, the pressure is lowered as far down as the vacuum pump allows, while in the second cycle the pressure is kept higher (halfway through the scale) to prevent the mixture inside the mould from spilling over as the pressure inside the vacuum diminishes.

Unlike the Ecoflex robots, the Mold Star robots could therefore be tested for more than a handful of cycles before the material degraded under inflation. This made it possible to finally try to embed the triboelectric sensor in place of the paper sheet strain limiter. In **Fig. 14** is a picture of the Mold Star robot under inflation. As shown from the picture, it is evident how the increase in volume of the air chambers in Mold Star actuators is less dramatic than that of Ecoflex actuators. The higher stiffness of Mold Star silicone rubber impacts in two different ways the behaviour of the robot during inflation, one direct and one indirect. Directly, for the same quantity of air injected into the chambers, it reduces the strain of the material, thus limiting the volume increase of the chambers and indirectly by affecting the amount of air pumped into the actuator; high stiffness means that higher pressures are needed for the same quantity of air to be injected into the robot.

An issue that was common to both the Ecoflex robots and the Mold Star robots came with the air pipe insertion. As already mentioned, in the first-attempt design, the tubing was

Figure 14: The finished Mold Star silicone rubber soft robot during inflation.

forced into the robot via a small hole torn on the out-facing wall of one of the two external chambers, like shown in **Fig. 14**. Then, since this pipe could not be properly sealed, some air leakage was always present during inflation. To solve this problem, a new design of the mould was adopted, with a pipe cavity already built-in. In the new mould, the tubing has to be inserted from the base of the robot and not from one of the external chambers. From the base, the pipe still emerges right inside one of the two external chambers, but of course this time coming from below not from the side. In order to do this, the geometry of the base case had to be modified to account for the pipe cavity. Other than modyfing the lower half of the mould, a seal for the air pipe was created on SolidWorks to be glued on the strain limiter, thus reducing the amount of air lost due to the improper adherence of the pipe with the body of the robot. The outer diameter of the seal matches with the diameter of the hole created on the new case, while the inner diameter matches with the outer diameter of the tubing. The base of the seal is a parallelepiped of dimensions 9,5 mm x 10 mm x 1.5 mm while the cylinder in which the air pipe is going to be inserted has a height of 3 mm from the base.

The presence of a seal made it necessary to slightly modify also the upper case of the mould, to account for the fact that the base of the seal emerges from the mixture poured in the base case. In its original design, the upper case presents small bumps throughout its whole length, whose purpose is to facilitate the binding between the two parts of the robot by increasing the surface of contact between cured material and fresh mixture. Not modifying this case would mean that, once the two parts of the robots are being bound

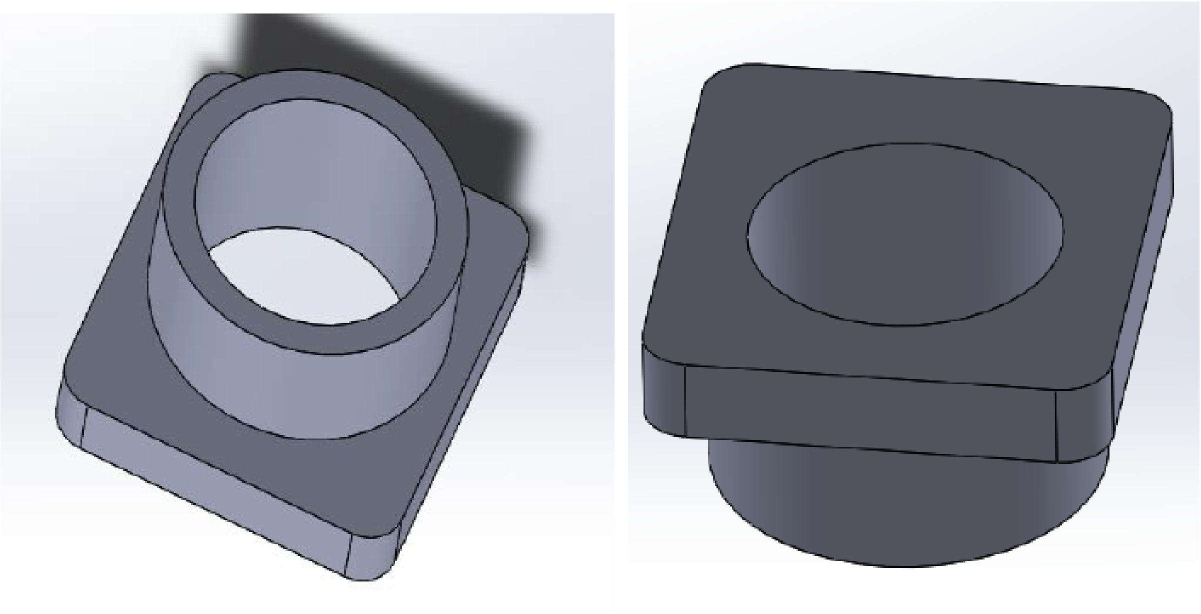

Figure 15: The seal as seen from above and below. When the seal is inserted into the robot pipe cavity, the strain limiter is glued at the base of the cylinder.

with one another with the extra mixture, the emerging seal and the bumps right above it get into contact, preventing proper adhering of the lower half of the robot body with the upper half which gets tilted up as consequence of the contact with the seal. So, in order to accommodate the seal inside the robot, two of the bumps extruded from the bottom half of the upper case are eliminated, precisely those that are placed right above the seal.

The strain limiter also had to be adapted to the new geometry of the robot; if initially the strain limiter was a rectangular sheet of paper having the same area as the base of the robot, after the adoption of the seal as a mean to insert the air-pipe from the base, a hole had to be cut on the surface of the strain limiter; the diameter of the hole matching the outer diameter of the seal cylinder. Once the hole on the strain limiter has been cut, the seal cylinder is insterted right into it. Between the two, glue is poured to insure good binging between seal and strain limiter. The new step-by-step process becomes as follows:

- a 40-gram 1:1 mixture of Mold Star part one and part two is mixed inside a small cup and then subjected to a first cycle of vacuum pumping to eliminate air bubbles;
- the mixture is poured into the upper case mould and the lower case mould and then subjected to a second cycle of vacuum pumping to eliminate the residual air inside the mixture;
- on top of the still-fresh mixture of the base case is placed the strain limiter with the hole cut on the strain limiter coaxial with the hole carved on the base case;
- the mixture is then left to cure for four hours inside the two halves of the mould;
- once the material has cured, glue is poured on top of the strain limiter, around the circumference of its hole;

- the seal, with the air pipe already inserted inside its cilynder, is introduced into the holes of the base case and of the strain limiter with its base facing upwards;
- after letting the glue to dry for ten minute, an additional 10-gram mixture of Mold Star is prepared and then poured on top of the strain limiter;
- the base of the seal is coplanar to the fresh mixture free surface. The upper half of the robot body is extracted from its case, placed on top of the fresh mixture and gently pressed to ensure good binding. The side with the two missing bumps is positioned right above the emerging base of the seal.
- the material is left to cure for additional four hours.

The process described is a very lengthy one, mostly due to the curing phases of the material, requiring more than 10 hours to build a single robot. Therefore, to reduce this time and before finally embedding the triboelectric layers into the robot, a new mould made of ABS was printed with the 3D printer. The geometry and design of the ABS mould was the same as the one just described. By using ABS, curing the rubber could be achieved with a drier in less than 25 minutes, thus greatly speeding up the process.

2.3 2.3 Embedding the triboelectric layers into the soft robots

The robots thus built show almost no air bubbles on the chamber walls nor do they show air leakage from the pipe cavity. Plus, with the mechanical properties of the Mold Star silicon rubber, the tearing of the walls is practically always prevented if not for high numbers of inflation/deflation cycles. Having solved the most pressing issues of the first prototypes, it became possible to embed the triboelectric sensor inside the robot, in place of the strain limiter. To this scope, in the first chapter, the four main catogories of triboelectric nanogenerators were described, along with a way to correlate voltage as measured with an electrometer with the separation distance or lateral displacement of the active layers of the triboelectric devices. Deformation sensors of the attached-electrode contact-mode and sliding-mode TENGs categories were therefore chosen as the possible solutions to implement in soft robots.

Considering the actuators of **Fig. 13** and **Fig. 14**, the triboelectric device would have to be placed between the base and the air chambers of the robot, with a stratum of silicone rubber binding the two together. In the first prototypes, the strain limiter adopted was a sheet of paper; common paper sheets are 0.1 mm thick, a thickness which does not constitute an obstacle to the correct connection of the two parts of the robot body. Triboelectric devices, on the other hand, present several layers of materials which are stacked one on top of the other, greatly exceeding the 0.1 mm thickness of paper. So, to embed the sensor into the actuator, the mould had to be slightly modified in order to accomodate for a thicker strain limiter; to do so, the base case walls were doubled in height thus allowing for a thicker strain limiter and for additional material to work as the binding stratum between base and chambers. The layers, rectangle-shaped, were also reduced in size by 1 mm on each margin, so that no layer would appear on the surface of the base of the robot. As a matter of fact, in the first attempts to embed the triboelectric sensors, when not reduced in size the sensors surfaced along the lateral faces of the base, leading to air leaks but also to the improper isolation of the electrodes of the device.

2.3.1 Contact-mode triboelectric sensor

The first sensor to be embedded was the attached-electrode contact-separation mode triboelectric nanogenerator of **Fig. 2**. Four total layers constitute the body of the nanogenerator. These are the steps followed to assemble the device:

- on a subtle sheet of nylon is glued a thin layer of copper. The dimensions of the nylon sheet are the same as the paper sheet described before, provided with the same hole as to account for the pipe seal;
- the copper layer, which is a couple of centimetres shorter in length than the nylon sheet, is glued on top of it starting from the edge of the nylon sheet which is opposite to the pipe hole;
- before gluing the two together, another foil of copper, less than 0.5 centimetre deep and a 3 cm long, is placed half-length between the two, with its free half emerging from the edge opposite to the pipe hole (see **Fig. 16** for reference). This copper foil will constitute part of the external circuit connecting the electrodes of the triboelectric nanogenerator to the electrometer, while the first copper layer will be one of the two electrodes of the device
- this first combined stratum of copper plus nylon is placed on top of the still fresh mixture inside the base case, the hole carved on the case being coaxial with the hole cut on the nylon sheet; since electrodes have to be isolated inside the body of the device, the copper layer of the first combined stratum faces downward and is directly in contact with the fresh mixture inside the mould, while the nylon layer faces upward.

The nylon sheet will have a double purpose: replace the paper sheet as the strain limiter of the robot and work as one of the two dielectric layers of the tribo-pair of the triboelectric device. As the strain limiter, on the layer of nylon will be glued the pipe seal, ensuring that no air leakage occurs during inflation at the point of insertion of the tubing. The cylinder of the seal will thus be inserted into the case and strain limiter holes, with the tubing already wedged into the seal cylinder. To complete the triboelectric device is the second combined stratum of dielectrics plus electrode. In particular, the other dielectric layer is made of Kapton tape:

- this Kapton tape layer has the same dimensions as the copper layer serving as the first electrode;
- glued on the Kapton tape is a layer of copper, with equal length and depth, to serve as the second electrode of the generator;
- in a similar fashion to the other part of the device, between the dielectric and the electrode is placed a copper foil to work as the external circuit connecting the electrodes;

- this second stratum is placed on top of the other with the Kapton layer facing the nylon sheet;
- on top of the now complete triboelectric sensor is poured a small quantity of fresh mixture to ensure good binding bewteen the two parts of the robot; the pipe seal base is coplanar with the free surface of the fresh mixture;
- the upper part of the robot is placed on top of the fresh mixture and gently pressed as to avoid any obstructions on the air channels connecting the chambers.

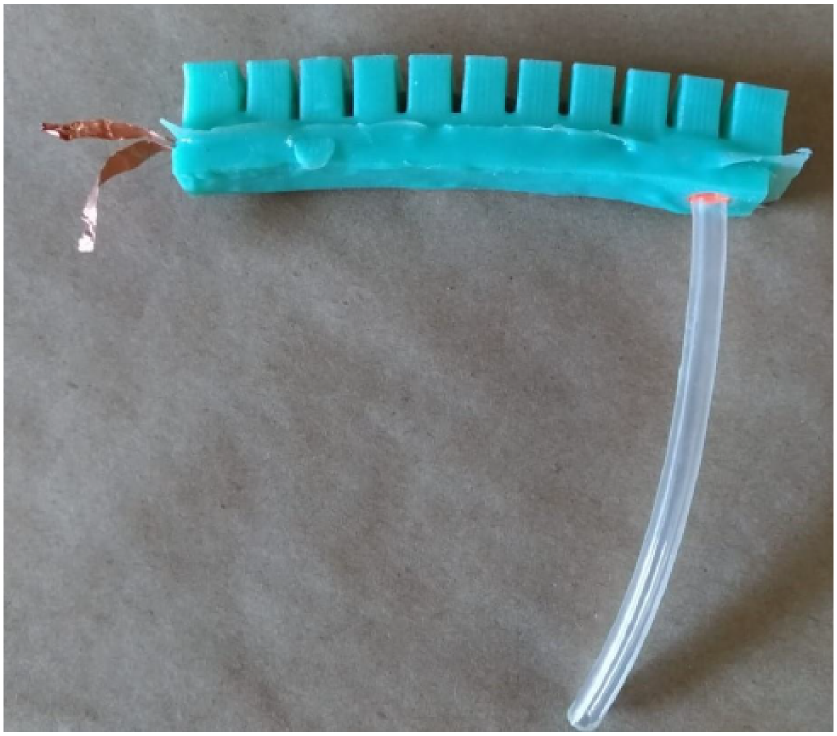

Figure 16: The triboelectric sensor-embedded soft robot. On the left, the two copper foils forming the external circuit to be connected with the electrometer. At the tubing insertion is noticeable, in bright orange, the pipe seal of **Fig. 15**.

When air is pumped into the chambers, the nylon layer limits the dilatation of the lower half of the robot body, which consequently bends downwards. As it bends, the layers of dielectrics, nylon and Kapton, are brought into contact, pressed one upon the other by the top and bottom strata of silicone rubber. This contact causes the accumulation of opposite charges on the now touching surfaces of the dielectric layers, that is, one of the two surfaces will be positively charged while the other will be negatively charged. The triboelectrication effect causes these surface charges to be transferred between the two triboelectric materials, until electrostatic equilibrium is reached. As air is pumped out of the chambers during the cycle of deflation, the robot goes back to its undeformed configuration. The pressure forcing contact between the layers is released and the dielectric pair separate. The electric potential difference generated by the polarised charges of the tribo-pair inner surfaces will drive electrons from the bottom electrode to the top electrode, in a short-circuit condition. The electric potential difference, given by the V-Q-x relationship of **Eg. 1** can be then measured by the electrometer. The more sensitive is the triboelectric sensor, the more accurate is the voltage measured at the two ends of the copper foils comprimising the external circuit of the device.

2.3.2 Contact-mode triboelectric sensor, second configuration

The prototype of **Fig. 16** was modified by splitting the triboelectric layers into three sensors, each sensor to be placed at a different position inside the robot base: two triboelectric devices embedded at the two edges of the robot and one at its centre. This was done to measure the electric potential difference at different sections of the actuator, to account for different values of the separation distance between the tribo-pair going from the pipe cavity to the robot free edge. Considering the triboelectric sensor-embedded robot of **Fig. 16**, the electric potential difference could only be measured on the edge opposite to the point of pipe insertion, i.e. to the left side, where the two copper foils emerge from the body of the robot. Now, while the assumption of uniformly distributed charges on the inner surfaces of the tribo-pair can still be considered valid for the system in study, the non-planar displacement of the dielectric layers (as was instead the case of the system in **Fig. 1**), consequence of the bending of the robot, means that the assumption of an uniformly thick air gap between the layers of dielectrics along the whole length of the robot cannot be accepted anymore. This is because of the non-spatially evenly distributed load acting on the tribo-pair, which varies significantly going from one end of the actuator to the other.

The dielectric layers are brought into contact by the combination of two different factors. The first contribution to their vertical displacement is given by the pressure in the chambers when air is injected through the tubing. As the pressure inside the chambers mounts, a vertical load acts on the stratum of silicone rubber connecting the upper half and the lower half of the robot; right underneath this stratum, and encased by the lower half of the robot constituting its base, is the triboelectric sensor. The load, via the stratum also acts on the triboelectric sensor. The other contribution is consequence of the differential strain at the base of the robot. The presence of the strain limiter causes the robot to behave anisotropically under deformation, forcing the actuator to bend; this bending results in a force which is the exerted over the triboelectric sensor from above and below, further bringing into contact the layers of dielectrics. With good approximation, the bending curvature of the actuator can be considered constant end to end, but the resulting force applied to it cannot. On the free edge the load will be at its minimun value, while at the centre it will reach its maximum. Consequently, the thickness of the air gap separating the tribo-pair will also be the greatest at the free edge and the smallest at the centre of the actuator.

As already mentioned, in the system depicted in **Fig. 1** and **Fig. 2**, the displacement of the tribo-pair was vertical and the planes on which sat the two dielectric stayed parallel at every cycle of contact/separation, which made for a costant separation distance along the length of the two dielectric layers; since in the robot-embedded-TENG system this could not be accomplished, this second configuration was tested to see if dividing the triboelectric sensor into three smaller sensors could better estimate the behaviour of the robot under inflation. Moreover, for smaller triboelectric nanogenerators, due to the reduced deflections which come from shorter bodies, approximating the $V-Q-x$ relationship as obtained for the system of **Fig. 2** becomes sensibly more accurate than with bigger sensors, so that a better correlation can be established between measured voltage at the electrodes and deformation of the robot.

In this configuration, the strain limiting nylon conserves its original dimensions, as do the copper foils working as external circuits and the Kapton tape, while the two copper electrodes are cut in three parts, each measuring 2 cm:

- a centimetre away from the pipe hole is glued the first 2 cm-long copper layer on top of the nylon sheet;
- the other two are glued at the centre and at the edge of the nylon sheet all equally distanced from one another;
- between each dielectric and electrode pair is placed, half-length, a copper foil, this time though stacked orthogonally in respect to the direction of maximum dimension of the nylon sheet.

Once prepared the two combined strata of the triboelectric sensor, the step-by-step process is the same as the one described for the other triboelectric device.

2.3.3 Sliding-mode triboelectric sensor

A third prototype was built with the intention of testing a sliding-mode driven nanogenerator. This, however, proved to be impossible due to the way the robot deformed. Let's assume that the behaviour of the robot under inflation can be described by the deformation of a beam under a distributed normal load. The beam has a fixed end, a clamp, but it's free on its other end; the fixed end corresponds to the pipe cavity end of the robot while the free end of the beam corresponds to the other edge of the robot. Considering the beam of **Fig. 17**, when the distributed vertical load w_0 is applied on the beam, the beam bends downwards. The dashed line represents the neutral axis; the upper fibers of the beam, as a result of flexure, are in tension while the lower fibers are in compression. Using this property of beams, the sliding-mode sensor was built to obtain the $V-Q-x$ relationship, thus correlating the displacement of the robot from it undeformed configuration to the electric potential difference measured at the electrodes.

The sensor was placed along the neutral axis of the equivalent beam layer; placed above the neutral axis was the dielectric layer, while below were two coplanar electrodes. So, the sensor built was of the conductor-to-dielectric kind. In this prototype the Kapton layer was eliminated; neither one of the electrodes was glued on the nylon sheet and, being coplanar, they were placed side by side on the first curing material of the base, each one measuring 3.5 cm along the x-direction of the robot (**Fig. 17**). This was the process followed to build the sensor:

- on each one of the two electrodes is glued the same copper foil used in the other prototypes for the external circuit, orthogonally with respect to the direction of maximum length of the electrode;

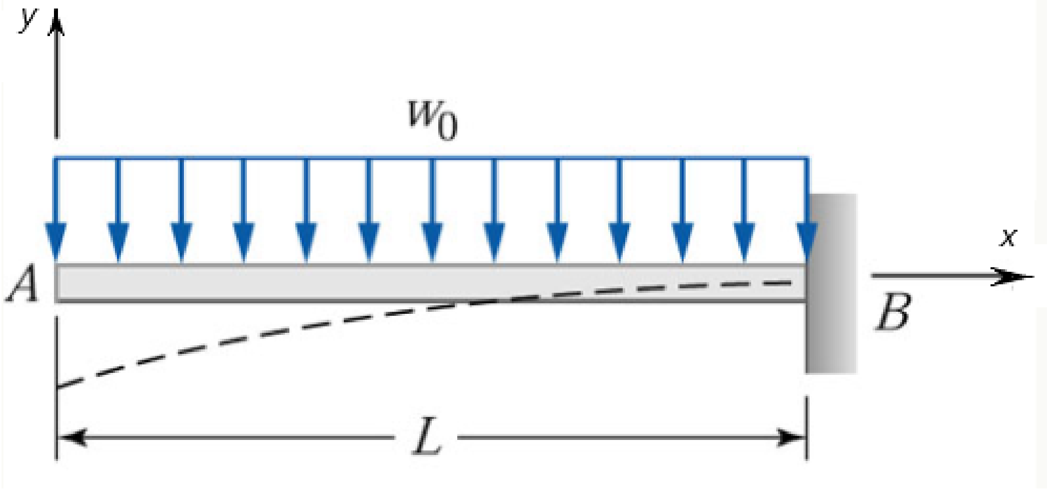

Figure 17: Uniformly distributed load on a beam. Reproduced from Ref. 32.

- no nylon was put on top of the curing mixture of the base case, so this time the Sil-Poxy adhesive has to be poured directly on top of the silicon rubber to glue the seal pipe;
- having holes of the same diameter as the pipe hole, two nylon sheets of equal dimensions, but smaller length-wise and depth-wise than the nylon sheets of the other prototypes, are inserted (stacked one on top of the other) between the pipe seal and the silicon rubber of the base. The lower nylon sheet being intended to work as the sole dielectric layer of the device, building the electric potential difference between the electrodes as it moved from one electrode to the other during inflation. The upper nylon sheet, on the other hand, being there to allow the movement of the lower sheet: with a single layer of nylon, when the two halves of the robot are bound together with the mixture, any movement of the layer itself becomes impossible as it is working as a strain limiter. With two sheets, the mixture is poured on top of the upper one, which thus works as the strain limiter, while the lower one, shielded by the other, is able to move in the small plane between the already cured base and the upper layer;
- mixture is then poured to bound the two parts of the device and the material is left to cure.

As anticipated, though, due to the limited deformations achieved by the Mold Star rubber and due to the geometry itself of the device, it was impossible to have any sliding of the free nylon sheet. This dielectric layer, constrained as it was around the seal cylinder, showed barely any relative movement with respect to the two electrodes. In conductor-to-dielectric sliding-mode nanogenerators, for the device to work it is necessary that a region of the dielectric layer overlaps with both electrodes, one electrode at a time. Under an external load, the dielectric layer slides over the two electrodes; as it moves, a portion of the dielectric layer inner surface that initially overlapped with the first one of the two electrodes, ends up overlapping with the other electrode, thus allowing for the charges to distribute uniformly on the non-overlapping portions of the dielectric layer inner surface. In the prototype built here though, no such relative movement was registered between the ”free” nylon sheet and the two copper layers and even for this sensor triboelectrification was mostly vertically contact-driven.

3 Creating the COMSOL model

3.1 Introduction

In the first chapter it was mentioned how triboelectric nanogenerators function thanks to the coupling effects of contact electrification and electrostatic induction to convert mechanical energy into electric energy. In other words, the principles of electrostatics can be used to adequately describe the working mechanism of TENGs in its entirety. As such, as already shown in part **1.3**, it becomes possibile to define an equivalent system for the TENG which uses equivalent capacitors to represent the effects of the application of an external load on the electric properties of the nanogenerator. Having already built several functioning prototypes of the device, the objective at hand is now to develop a model in the simulation environment with which to study the behaviour of the triboelectric nanogenerator/sensor under the application of an external load. In this, while the $V-Q-x$ relationship as expressed in **Eq. 1** gives a good understanding of the core principles which trigger electrification in tribolectric nanogenerators, it is still a too rudimental fomulation if the creation of the model in the simulation environment is to be obtained. Effectively, in order to implement such a simulation, it is more useful to utilise the results of the equivalent circuit using the capacitive properties of TENGs, since for a system such as the equivalent one, a more general formulation is of easier derivation. Therefore, the creation of the COMSOL model used to simulate the behaviour of the nanogenerator has to be preceded by the derivation of this variational formulation with which to describe it.

But before even doing that, it is first necessary to obtain the fundamental equations which are to be used to represent the physics of the problem as the crucial step to create a functioning model for the study of the behaviour of the device. Once these equations are obtained, it will be possible to derive the variational formulation from the equivalent capacitor circuit.

3.2 The physics of the triboelectric problem

3.2.1 Deriving the fundamental equations

Being as it is an electrostatics-governed system, the laws which apply to electrostatics in general also have to apply to a triboelectric nanogenerator at any given condition. Considering the scalar quantity of the electric potential, ϕ, the electric field of a system can be expressed by the following equation:

$$\mathbf{E} = -\nabla\phi \tag{36}$$

Electrostatics follows Gauss's laws, which states that "*the flux of the electric field* ***E*** *generated by a system of charges through a closed surface is proportional to the algebraic sum of the electric charges enclosed by the surface*" [15]. In its integral form, this law can be also written as follows [15]:

$$\Phi_E = \oint_S \mathbf{E} \cdot \mathbf{u}_n dA = \frac{Q}{\epsilon_0} = \int_V \frac{\rho}{\epsilon_0} \cdot dV \tag{37}$$

where dA is the infinitesimal element of area of the hypothetical surface through which passes the electric flux, Φ_E, generated by the electric field $\mathbf{E}$, $\mathbf{u}_n$ is the outward-pointing normal vector of said infinitesimal element of area, Q is the electric charge enclosed by the hypothetical surface, ϵ_0 is the vacuum permittivity, ρ is the total electric charge density of the system expressed per unit of volume and dV is the volume element enclosed by the hypothetical surface.

Guass's law of **Eq. 37** can be equivalently written in its differential form by using the divergence theorem:

$$\nabla \cdot \mathbf{E} = \frac{\rho}{\epsilon_0} \tag{38}$$

Thus, combining the results of **Eq. 36** and **Eq. 38** yields:

$$\nabla^2 \phi = -\frac{\rho}{\epsilon_0} \tag{39}$$

which is the Poisson's equation for electrostatics. Considering now dielectric materials, it is then possible to define the electric induction $\mathbf{D}$ generated by the electric field acting upon a dielectric medium [15]:

$$\mathbf{D} = \epsilon_0 \mathbf{E} + \mathbf{P} \tag{40}$$

where $\mathbf{P}$ is the electric polarisation, a vector field of the density of electric dipole moments in a dielectric material, which - in a linear, homogeneous and isotropic dielectric with instantaneous response to changes in the electric field - is directly proportional to the electric field itself:

$$\mathbf{P} = \chi \epsilon_0 \mathbf{E} \tag{41}$$

where χ represents the electric susceptibility of the dielectric material. Therefore, introducing the relative permittivity of the dielectric medium which is function of its electric susceptibility, $\epsilon_r = 1 + \chi$, and given that the absolute permittivity of the dielectric ϵ is the product of the relative permittivity times the vacuum permittivity, it is possible to express **Eq. 40** as follows [15]:

$$\mathbf{D} = \epsilon \mathbf{E} \tag{42}$$

Recalling again the results of Gauss's law of **Eq. 38** yields [15]:

$$\nabla \cdot \mathbf{D} = \rho_f \tag{43}$$

with ρ_f being the number of free charges per unit volume. Finally, combining the results of **Eq. 36**, **Eq. 42** and **Eq. 43** yields:

$$-\nabla \cdot (\epsilon \nabla \phi) = \rho_f \tag{44}$$

which in absence of space charge becomes:

$$\nabla \cdot (\epsilon \nabla \phi) = 0 \tag{45}$$

also known as Laplace's equation. This equation represents the partial differential equation for the electrostatic system considered, from which to develop the finite element analysis to be solved in the simulation environment. The constitutive relation, which is a function of the relative permittivity of the materials of the system, is in turn given by the electric induction **D** as defined in **Eq. 40**.

Eq. 38 represents the first one of the four Maxwell's equations describing electromagnetism. Electrification in triboelectric nanogenerators and sensors is now understood to be correlated with the displacement current, time derivative of the electric displacement field **D** as defined by **Eq. 40** and **Eq. 42** [13] [14]:

$$\mathbf{J} = \frac{\partial \mathbf{D}}{\partial t} = \epsilon_0 \frac{\partial \mathbf{E}}{\partial t} + \frac{\partial \mathbf{P}}{\partial t} \tag{46}$$

Therefore, the output characteristics of TENGs consequence of the application of an external load can be traced back to this equation, which is a more rigorous formulation than the V-Q-x relationship already introduced in the first chapter. This equation shows again that the nature of the electrification mechanism in triboelectric devices is given by electrostatic induction, in the form of the electric field **E**, and by the contribution of the accumulation of polarised charges on the opposite surfaces of the active layers of the device, expressed by the polarisation density **P**. In other words, **Eq. 46** confirms the results of the $V - Q - x$ relationship.

3.2.2 Variational formulation and algebraic formulation

As already mentioned, in the absence of space charge, Poisson's equation of **Eq. 44** becomes Laplace's equation as expressed in **Eq. 45**, representing the partial differential equation for the system at hand. Introducing the weight function $\omega(x, y, z)$ and solving this equation by integration over the volume of a 3D domain, Ω, yields [16]:

$$\int_\Omega \nabla \cdot (\epsilon \nabla \phi) \omega dV = \int_\Omega (\epsilon \nabla^2 \phi) \omega dV \tag{47}$$

which, by partial integration, can be also rewritten as [16] [17]:

$$\int_\Omega \epsilon \nabla \cdot (\omega \nabla \phi) dV - \int_\Omega \epsilon (\nabla \phi \cdot \nabla \omega) dV = 0 \tag{48}$$

From this, using the divergence theorem on the first integral of the equation it is possible to write that:

$$\oint_{\partial\Omega} \epsilon (\omega \nabla \phi \cdot \mathbf{n}_n) dS - \int_\Omega \epsilon (\nabla \phi \cdot \nabla \omega) dV = 0 \tag{49}$$

Recalling **Eq. 36**, in any given system, the electric field points from regions of high electric potential to regions of low electric potential and it is therefore equal to the negative gradient of the electric potential of the system itself. Considering now **Eq. 49**, from the definition of electric field as enunciated, the term between brackets on the first integral, which is the scalar product of the gradient of the electric potential and the outward normal to the surface, can be further understood to be the normal component of the electric field **E**:

$$\epsilon(\nabla\phi \cdot \mathbf{n}_n) = \epsilon E_n \tag{50}$$

Subsituting this term in the previous equation and in turn introducing the surface charge density as defined by $\sigma = \epsilon E_n$ yields [16]:

$$\oint_{\partial\Omega} \sigma\omega dS - \int_{\Omega} \epsilon(\nabla\phi \cdot \nabla\omega)dV = 0 \tag{51}$$

or alternatively:

$$\int_{\Omega} \epsilon(\nabla\phi \cdot \nabla\omega)dV = \oint_{\partial\Omega} \sigma\omega dS \tag{52}$$

The equation thus obtained represents the weak formulation of Laplace's equation of **Eq. 45**. From this equation it is possible to obtain the equivalent matrix formulation for the electrostatics problem via discretisation of the domain. Considering a finite element with m nodes, by defining the 1 x m shape function **N** and the m x 1 nodal potential vector $\boldsymbol{\phi}_e$, it is possible to interpolate the electric potential $\phi(x, y, z)$ and the weight function $\omega(x, y, z)$ from the respective nodal values of the element at hand [16] [17]:

$$\phi_e(x, y, z) = \sum_{i=1}^{m} N_i\phi_i = \mathbf{N}\boldsymbol{\phi}_e \tag{53}$$

$$\omega_e(x, y, z) = \sum_{i=1}^{m} N_i\omega_i = \mathbf{N}\boldsymbol{\omega}_e \tag{54}$$

Adopting the same shape function for the gradients too, it is possible to render the results of **Eq. 52** as a function of the interpolated values for the finite element characterised by the outer surface S_e which encloses the volume V_e [16] [17]:

$$\int_{Ve} \epsilon(\nabla\phi_e \cdot \nabla\omega_e)dV_e = \oint_{Se} \sigma_e\omega_e dS_e \tag{55}$$

or equivalenty, using the transpose operator [16]:

$$\int_{Ve} \epsilon(\nabla\phi_e)^T(\nabla\omega_e)dV_e = \oint_{Se} \sigma_e\omega_e dS_e \tag{56}$$

Expanding the gradient operators from the shape function **N** [16]:

$$\boldsymbol{\phi}_e^T \left\{ \int_{Ve} \epsilon \left[\left(\frac{\partial \mathbf{N}}{\partial x}\right)^T \left(\frac{\partial \mathbf{N}}{\partial x}\right) + \left(\frac{\partial \mathbf{N}}{\partial y}\right)^T \left(\frac{\partial \mathbf{N}}{\partial y}\right) + \left(\frac{\partial \mathbf{N}}{\partial z}\right)^T \left(\frac{\partial \mathbf{N}}{\partial z}\right) \right] dV_e \right\} \boldsymbol{\omega}_e = \left(\oint_{Se} \sigma_e \mathbf{N} dS_e \right) \boldsymbol{\omega}_e \tag{57}$$

which, since the weight function is arbitrarily chosen becomes [16]:

$$\boldsymbol{\phi}_e^T \left\{ \int_{Ve} \epsilon \left[\left(\frac{\partial \mathbf{N}}{\partial x}\right)^T \left(\frac{\partial \mathbf{N}}{\partial x}\right) + \left(\frac{\partial \mathbf{N}}{\partial y}\right)^T \left(\frac{\partial \mathbf{N}}{\partial y}\right) + \left(\frac{\partial \mathbf{N}}{\partial z}\right)^T \left(\frac{\partial \mathbf{N}}{\partial z}\right) \right] dV_e \right\} = \left(\oint_{Se} \sigma_e \mathbf{N} dS_e \right) \tag{58}$$

In **Eq. 58**, the quantity between curly brackets represents the capacitance $\mathbf{C}_e$ of the finite element at hand, while the second term of the equation represents the element charge $\mathbf{Q}_e$. From this equation, it is apparent how the element capacitance takes the form of a matrix while the element electric charge takes the form of a vector. So, **Eq. 58** can be rewritten in the matrix form of the problem [16] [17]:

$$\mathbf{C}_e \boldsymbol{\phi}_e = \mathbf{Q}_e \tag{59}$$

Extending the results as obtained for the i-element of **Eq. 59** to the n-elements of the system yields:

$$\mathbf{C} \boldsymbol{\phi} = \mathbf{Q} \tag{60}$$

The equation thus obtained correlates the electric charge transfer with the electric potential of the system. As evident, this is in direct analogy with the force-displacement correlation expressed by the $\mathbf{Ku} = \mathbf{F}$ stiffness relation that exists in structural mechanics. Same as the with the analysis of structure, where either the force or the displacement can be specified at any given point of the domain, also in this case it is not possible to specify both the electric potential and the electric charge at any point of the domain [16]. Moreover, the electric charge vector of **Eq. 60** accounts for the boundary conditions of the system just like the force vector $\mathbf{F}$ in structural mechanics [17].

As mentioned at beginning of this subchapter, Laplace's equation, in its weak formulation, is to be solved by integration over a 3D domain. The algebraic formulation, is also derived for such a domain. The stated purpose of the COMSOL model is to predict the behaviour of the triboelectric sensor when the soft robot in which this is embedded deforms under the application of a load, i.e during inflation. In this, the accuracy of results guaranteed by a 3D model over a 2D one is outweighed by the longer computing times of the former over the latter. Consequently, the domain can be scaled down froma 3D one, Ω, to a 2D one, $\partial\Omega$ for the use intended for the COMSOL model.

In general, the shape function $\mathbf{N}$ can be espressed by the following matrix multiplication [18]:

$$\mathbf{N} = \mathbf{P}\mathbf{A}^{-1} \tag{61}$$

where $\mathbf{P}$ is the matrix of the linear polynomials which describe the shape function using a polynomial approach, while $\mathbf{A}^{-1}$ is the inverse matrix of the matrix whose constant coefficient are the polynomials $\mathbf{P}$ evaluated at the nodes of the finite element. For a triangular-shaped finite element with one node at each vertex, the two matrixes are repectively [18]:

$$\mathbf{P} = \begin{bmatrix} 1 & x & y & 0 & 0 & 0 \\ 0 & 0 & 0 & 1 & x & y \end{bmatrix} \tag{62}$$

$$\mathbf{A} = \begin{bmatrix} 1 & x_1 & y_1 \\ 1 & x_2 & y_2 \\ 1 & x_3 & y_3 \end{bmatrix} \tag{63}$$

and its inverse:

$$\mathbf{A}^{-1} = \frac{1}{2A} \begin{bmatrix} x_2y_3 - x_3y_2 & x_3y_1 - x_1y_3 & x_1y_2 - x_2y_1 \\ y_2 - y_3 & y_3 - y_1 & y_1 - y_2 \\ x_3 - x_2 & x_1 - x_3 & x_2 - x_1 \end{bmatrix} \tag{64}$$

where the element area is given by [16][18]:

$$A = \frac{1}{2} det \mathbf{A} \tag{65}$$

So, the shape function for the 2D problem is given by [16]:

$$N_i = \frac{1}{2A}(a_i + b_i x + c_i y) \tag{66}$$

where a_i, b_i and c_i represent the coefficient of $\mathbf{A}^{-1}$ of **Eq. 64**. Now that the shape functions for the 2D problem have been obtained, it is possible to obtain the element capacitance for a 2D domain [16]:

$$\mathbf{C}_e = \frac{\epsilon s}{4A} \begin{bmatrix} {b_1}^2 + {c_1}^2 & b_1b_2 + c_1c_2 & b_1b_3 + c_1c_3 \\ b_1b_2 + c_1c_2 & {b_2}^2 + {c_2}^2 & b_2b_3 + c_2c_3 \\ b_1b_3 + c_1c_3 & b_2b_3 + c_2c_3 & {b_3}^2 + {c_3}^2 \end{bmatrix} \tag{67}$$

where s is the thickness of the triangles which constitute the 2D domain of the element.

3.2.3 Boundary conditions

So, the algebraic formulations for 2D and 3D domains have been derived from the fundamental equations of electrostatics. Until now, the boundary conditions of the system have not yet been addressed. Given the physics of the problem, it is convenient to consider both Dirichlet and Neumann conditions as the boundary conditions of the system: recalling the results of **Eq. 58**, at any given point of the domain, either the electric potential or the electric charge could be specified. The triboelectric device is implanted into the soft robot to work as a deformation sensor, where the deformation of the robot is to be correlated with the change in voltage as measured at the electrodes of the sensor. For this to be implemented, it is not possible to impose Dirichlet conditions on the boundary of the domain other than in one of the electrodes intended to be used as the reference electrode of the system: for this electrode alone it is valid the imposition of a constant voltage on the boundary.

From chapter 1, a triboelectric nanogenerator/sensor is made of several layers of different materials: in its most basic design, two metal layers functioning as the electrodes and two dielectric layers functioning as the layers of charge exchange. As stated, the domain of the element is reduced from a 3D one down to a 2D one, corresponding to the longitudinal section of the triboelectric device (see **Fig. 18** for reference). From the figure below it is possible to recognise the right-end portion of the robot-embedded triboelectric device: in green is the silicone rubber, consituting the lower half of the robot inside which is encased the triboelectric sensor, in light brown are the two layers of copper working as electrodes, in blue are the two dielectric layers and in gray is the air gap separating them.

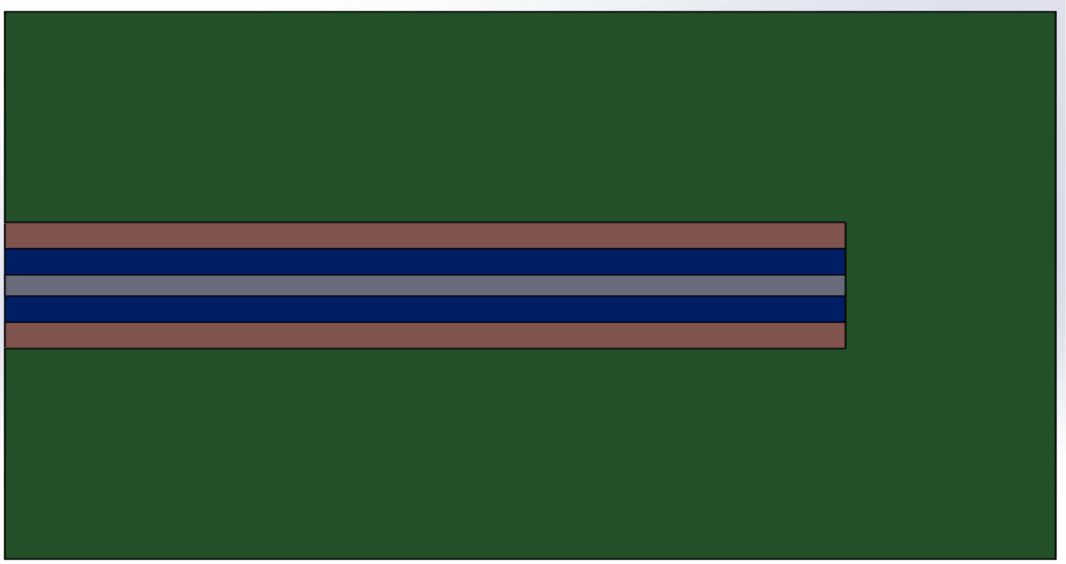

Figure 18: 2D domain of the COMSOL model.

Having already addressed the reference electrode, the boundary condition can be stated for the dielectric layers, arbitrarily imposing surface charge densities on the two dielectric layers. Neumann boundary conditions specifies the normal derivative of a solution on the boundary of the domain. In **Eq.**, the normal derivative of the electric potential gave the normal component of the electric field, which multiplied by the permittivity of the medium gave in turn the surface charge density:

$$\sigma = \epsilon E_n \tag{68}$$

From this, the Neumann condition for the two dielectric layers is [19]:

$$\sigma = -\epsilon \frac{\partial \phi}{\partial n} \tag{69}$$

Once the boundary conditions are imposed, it is possible to solve the electrostatic problem for the triboelectric device.

Imposing the density of charges on the dielectric layers of the sensor is justified by the electrical properties of triboelectric nanogenerators/sensors. Ideally, as the triboelectric sensor is encased inside the soft robot body, it is insulated from the exterior, being completely surrounded on all sides by silicone rubber. In order for it to be completely insulated, though, it is necessary to coat the triboelectric device from the silicone rubber itself. This is because polydimethylsiloxane, i.e. silicone rubber, is also a dielectric material, meaning that it can undergo polarisation of charges with the presence of an electric field. So, assuming that such insulation can be guaranteed, the triboelectric sensor as it is described in part **2.3** is connected to the exterior only via two copper foils attached to the two electrodes and working as the external circuit of the system. In such conditions, charge decay becomes negligible over time on the surfaces of the dielectric layers [3][20]. Moreover, in insulators the hypothesis of uniformly distributed charges over the surface, in this case over the two inner surfaces of the dielectric materials, can be considered a valid assumption. Finally, considering surface charge densities on these surfaces as different from zero at time $t_0 = 0s$ is also justifiable by the intrinsic capacitive properties of triboelectric sensors, as already mentioned in the first chapter [3][8][21].

3.3 Building the model

3.3.1 The first models

In **Fig. 19** is depicted the model of the portion of the triboelectric sensor corresponding to a single air chamber at the edge of the robot body. In its lower half it is recognisable the triboelectric sensor embdedded into the robot. When the chamber is being inflated, the robot bends downwards, causing the dielectric layers of device to come into contact. This, in a similar fashion to what has been described in chapter 1, triggers the triboelectrification of the device, prompting the generation of an electric potential difference at its electrodes. Simulating the mechanical behaviour of the robot and the mechanical and electrical behaviours of the sensor encased into the robot during deformation would be extremely time consuming using a model such as the one depicted in **Fig. 19**. Effectively, studying the behaviour of the robot at its air chambers defeats the purpose of the study, which is to find the relation that exists between vertical displacement at its base and voltage at the sensor electrodes, as it unnecessarily complicates the physics of the problem. Better would be to find a way to replicate the deflection of the robot along the strain limiter caused by a given volume V_a of air injected into the air chambers without actually having to simulate the injection itself. This can be easily done by assuming that the robot deforms like a beam, clamped at one of its edges, under the application of a distributed load. In particular, once the pressure inside the chamber has been estimated through the ideal gas law, as shown in **part 1.4.1** of the first chapter, the distributed load can be immediately calculated from the knowledge of the area at the base of the air chambers.

Another issue that comes with a 3D model is the number of finite elements with which to divide the robot and the robot-embedded sensor. Even using the *physics-controlled mesh* tool of the COMSOL software, where the triangles of the mesh adapt to the geometry of the model, that is, finer triangles at the edges and coarser triangles elsewhere, the problem concering the number of finite elements could not be circumvented. This is because, given the small dimensions of the layers consituting the triboelectric sensor, around 0.25 mm thick for the air gap and the copper layers, the finest mesh triangles had to be chosen for the solution of the simulation to converge. Too thick the triangles and the mesh would not be able to guarantee the convergence of the solution. Still, the higher accuracy guaranteed by less thick triangles could not outweigh the longer processing time needed for the simulation to run. So, even having discarded the portion of the robot corresponding to the air chambers during inflation, the model as depicted in **Fig. 19** proved to be too complex to be used for the study of the device in the simulation environment.

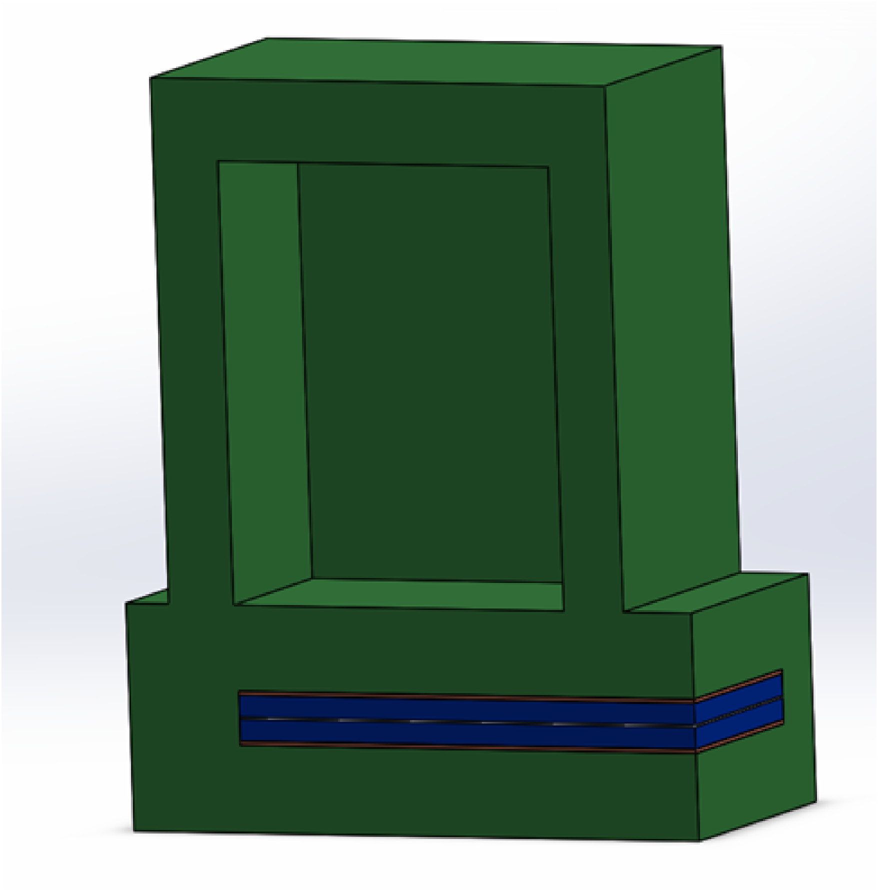

Figure 19: COMSOL model of a single air chamber with the triboelectric sensor visible in the lower half of the robot body.

Therefore, the robot-embedded triboelectric sensor model had to be simplified in order to reduce the computation time: a 2D model was adopted representing the longitudinal section of the triboelectric layers. The device is encased at the base of the soft robot, working as its strain limiter as well as its deformation sensor. As mentioned, being of less interest, the upper half of the robot body corresponding to the air chambers was eliminated to further reduce the computational time and the complexity of the model. Moreover, from part **1.4.1** it was proved that the bending curvature at the base can be considered constant throughout the whole length of the strain limiter; thus, the study could be reduced from that of the triboelectric device in its entire length to the study of a single section of the device whose length was comparable to that of a single air chamber of the robot (see **Fig. 10** for reference).

To study the device, two chambers were analysed, one at the edge (connected to a single chamber on one of the edges) and one in the middle (between two other chambers). The first one of these two models can be seen in **Fig. 18**, the second one in **Fig. 20**. The geometry of the models is the following: at the centre is a thin layer representing the air gap between the active layers of the triboelectric device (in gray in **Fig. 18** and **Fig. 19**); the two dielectric layers of the device sit directly above and below the air gap (in blue in **Fig. 18** and **Fig. 19**) while the two copper layers (in light brown) are respectively at the top and at the bottom of the upper and lower dielectric layers; the silicon rubber encasing the triboelectric device is in green.

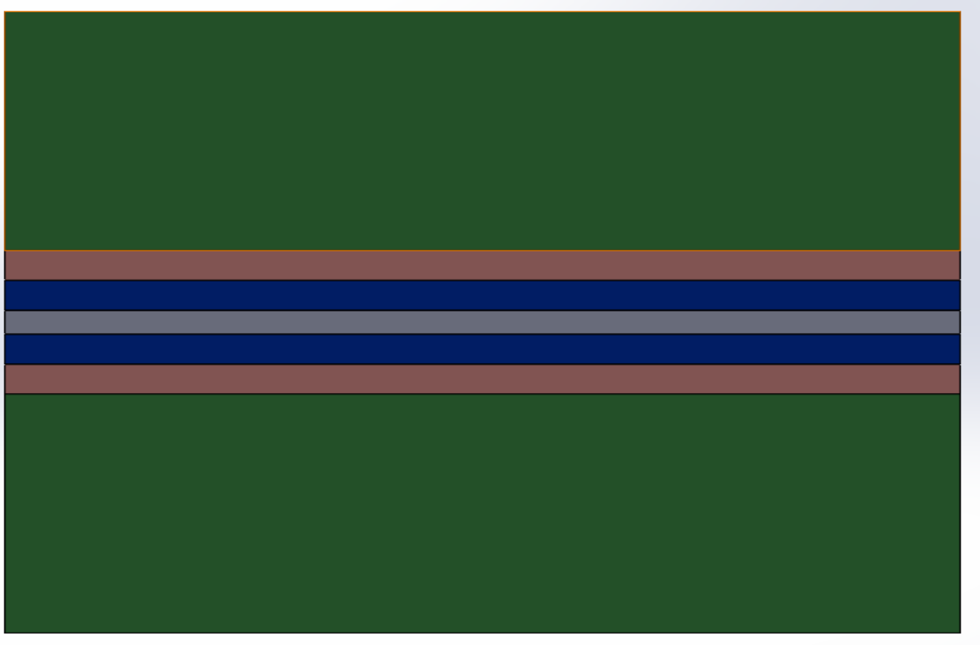

Figure 20: 2D domain of the COMSOL model.

As mentioned, the deflection of the robot along its strain limiter is assumed to be equal to that of a beam that bends under the application of a vertical distributed load. The force per unit area to be applied on the model was estimated to be the same as the pressure exterted from the air inside the chambers on the surface area at the base of the chambers themselves. This pressure could be immediately calculated from the ideal gas law, by knowledge of the volume of air injected into the actuator with the syringe during the testings of the prototypes of chapter 2. In the first model, an equivalent concentrated load was applied on one of the two ends of the model, with the other end being constrained. The vertical displacement at the free edge of the model, caused by this load, had to be consistent with the one calculated using the static beam equation of **part 1.4.1**. In the model of **Fig. 18**, the constrain, a clamp, was applied on the left end, where the continuity of the structure is interrupted, while on the free right end was applied the concentrated vertical load. It is worth noting that in these initial phases, the study was a non-time dependent one, so that the behaviour of the device could only be guessed for the final vertical displacement from its undeformed condition; the in-between stages of deformation of the device from its configuration at rest to its fully deformed one could not be obtained with this first model study.

For the mechanical properties, only the linear elastic material model and the non-linear elastic material model were initially chosen for the study of the device. Every layer of **Fig. 18** and **Fig. 20** was assumed to show a linear elastic behaviour under the application of a load, with the only exception being the two dielectric materials, for which the non-linear elastic material model was used. So, in this first simulation, both the layer of air and the layer of silicon rubber were assumed to behave like linearly elastic materials. For the air gap this was because, in structural mechanics, the COMSOL software does not allow the user to choose gas-like mechanical properties for any of the model parts and this meant that a solid-like behaviour had to be considered for the air gap. A different approach would have been to completely discard the air gap between the dielectric layers, but since the relationship that exists between deformation of the robot and electric potential at the electrodes can only be inferred from the variation in thickness of the air gap under the application of an external load, this solution could not be implemented. As for the the silicone rubber, even though the hyper-elastic properties of the material were already known, it was assumed that the deformation at the base behaved similarly to the that of the strain limiter. As said, for the sake of simplicity, a linear elastic model was chosen for the silicone rubber.

Due to the mechanical properties adopted for the layers of the device, in this model the deformation caused by the equivalent load applied to its free end was significantly smaller than the deformations shown by the prototypes of chapter 2. Moreover, the curvature of the device was non-constant along the longitudinal section, which is in contrast with the results of **part 1.4.1** for soft robots, where the bending curvature was proved to be constant along the strain limiter whole length. Then, owing to the small ratio between length and height, the model presented significant shear stresses, as its behaviour under the external vertical load could not be assumed to be similar to that of a beam under the same loading conditions. Indeed, for beams, a ratio of height to length equal or larger than 1/10 ensures that shear stresses at the cross section are basically negligible when compared with normal stresses [22]. In the models of **Fig. 18** and **Fig. 20**, the ratio of height to length is obviously lower than 1/10 which means that, with the vertical load applied at their free ends, shear stresses cannot be overlooked anymore in the evaluation of total stresses at the cross sections of the device.

This becomes clear when analysing the stresses in the two models as depicted in **Fig. 21** and **Fig. 22**. At the left edges of the two models is the constraint, a clamp, while at free edges, on the right, is the vertical concentrated load. It is immediately noticeable how the bending curvatures for both models are not constant along the beam's x-axis (longitudinal). The reasons for this, as already explained above, are to be attributed to the mechanical properties chosen during the model-building stage for the simulatation the behaviour of the various layers of the triboelectric sensor. As said, this result was not consistent with the theoretical findings of **part 1.4.1** nor with the direct empirical findings of the inflation tests on the soft robot prototypes of chapter 2. In **Fig. 22** is the middle chamber model, in **Fig. 21**, the edge chamber one. For both, the peak stress was reached along the thin copper layers working as the electrodes of the device; significant shear stresses were particularly evident in the middle chamber model, while in the edge chamber model, the presence of silicone rubber surrounding the triboelectric sensor on its free edge partially mitigated shear stresses in the cross section at this end. This was because, while in the middle chamber model the free end cross sections of the triboelectric device and of the silicone rubber coincided, in the edge

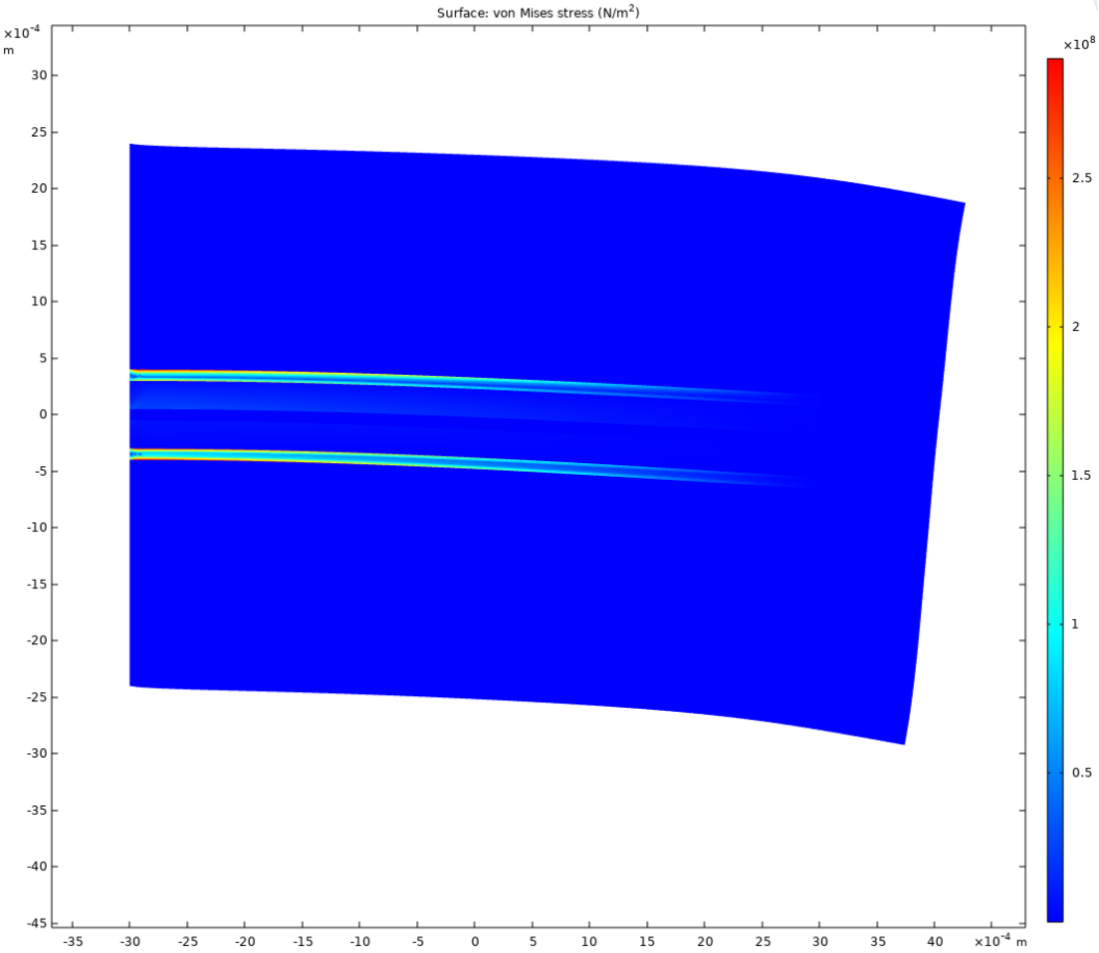

Figure 21: 2D domain of the ”edge chamber” COMSOL model.

chamber model the presence of additional rubber material at the end of the triboelectric layer meant that the load was applied to the end cross section of the sole silicone rubber, while in the middle chamber model, as the two cross section coincided, it was applied to both. Still, analysing the deformation at the free end cross section, shearing is visible throughout the whole height of the section itself even if the shear stresses seem to be lower than in the middle chamber model. As expected, in both models peak stress was reached at the cross section corresponding to the constrained end of the element, along the thin copper layers (bright colored in both figures), being particularly high on the top copper layer. Given the geometry of these first models, that is, dielectric layers more than twice as thick as the copper layers, stresses were significantly lower in the formers as compared with the latters, especially on the bottom dielectric layer. As for the silicone rubber surrounding the device, stresses were almost negligible at every cross section, starting from the constrained end and ending with the free end of the model. Other than this, in the middle chamber model of **Fig. 22**, shearing came visibly in the form of sliding, as evident from the figure. Interrupting the continuity of the robot-embedded triboelectric sensor withouth ensuring that the two halves of the device separated by the air gap stay coplanar led to the sliding of the bottom half underneath the top half as visible from the figure. Had this been ensured, then it is safe to

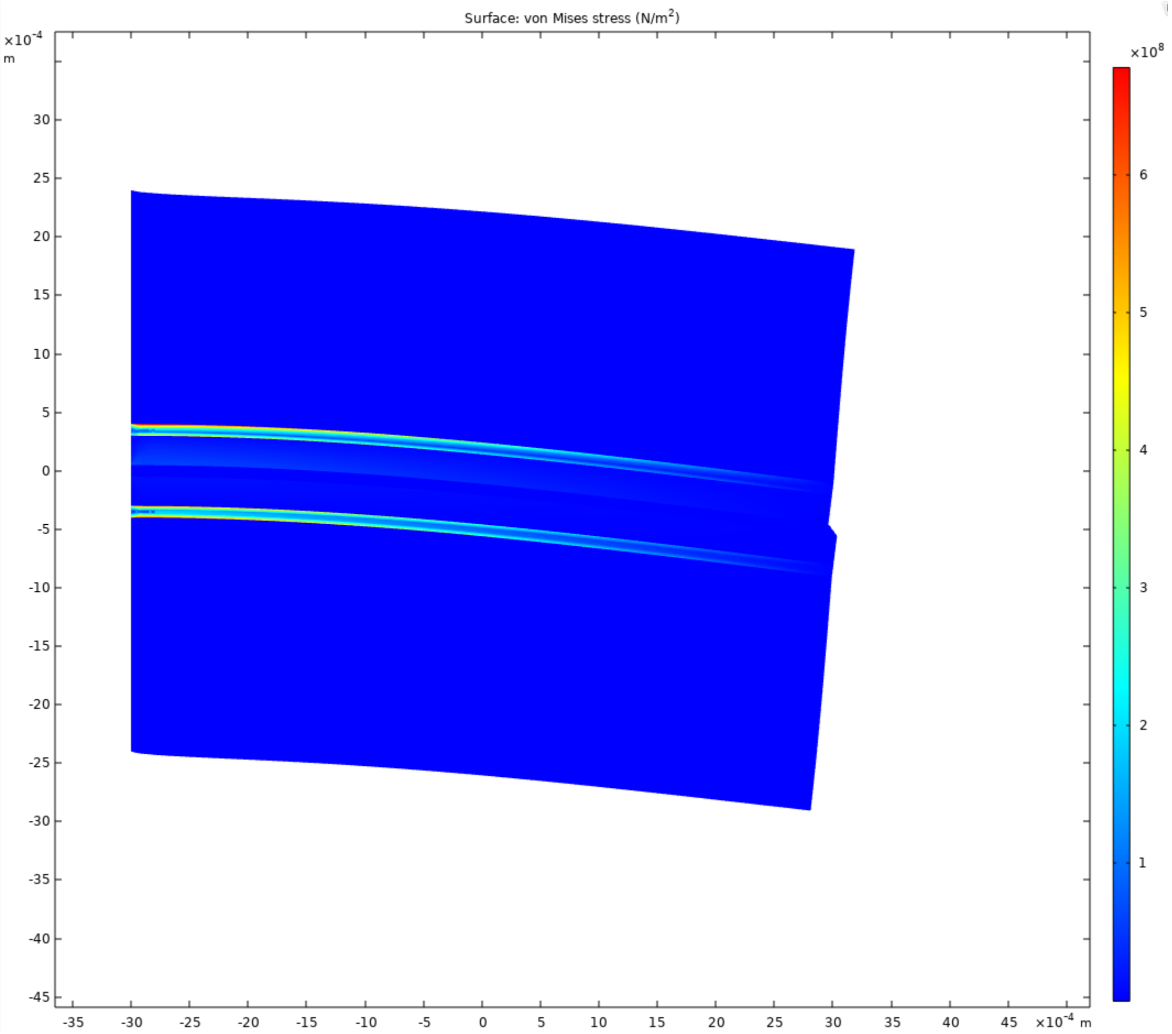

Figure 22: 2D domain of the "middle chamber" COMSOL model.

expect that the shear stresses at the cross section of the free end of this element would be even greater than they already were in the model so far described.

Having the models these many flaws, little to no attention was given to the electrostatic part of the analysis at this stage of the model development. Therefore, before analysing the electric behaviour of the triboelectric sensor after deformation, which is the scope of the work, it became necessary to fix the model in order for it to have a mechanical behaviour consistent with direct testing and theoretical results.

3.3.2 Improving the models

The first step was changing the mechanical properties of the various component of soft robot and triboelectric sensor. In particular, for the robot body the hyperelastic material model was adopted. Due to the limitations of the COMSOL software, as already explained in **part 3.3.1**, for the air gap between the dielectric layers a solid material model had to be adopted, specifically, it was also chosen the hyperelastic model over the linear elastic model of the first simulations. For both the air gap and the silicone rubber, a Mooney-Rivlin solid model was used to simulate their behaviour under deformation. In this model, the strain energy density function **W** is a linear combination of two invariants of the left Cauchy-Green deformation tensor **B**.

Considering a body in space in its undeformed configuration, it is possible to define the Lagrangian coordinate X of a material point of the body as the position of said point relative to a coordinate basis, whereas its Eulerian coordinate x is the point position in the deformed configuration [23][24]. Two material points on the undeformed body are identified by the Lagrangian coordinates X_P and $X_p + dX$. After deformation, the position of the two is given by their Eulerian coordinates, which are function of both the Lagrangian coordinates and time [23]:

$$x_p = f(X_P, t) \tag{70}$$

$$x_q = f(X_P + dX, t) \tag{71}$$

The deformation gradient tensor for the two material points whose relative positions change after deformation is given by the following equation [23]:

$$\mathbf{F} = \frac{\partial f}{\partial X} = \frac{\partial x}{\partial \mathbf{X}} \tag{72}$$

From this tensor, the left Cauchy-Green tensor is in turn given by [23][24]:

$$\mathbf{B} = \mathbf{F}\mathbf{F}^T \tag{73}$$

For an incompressible Mooney-Rivlin material, the strain energy density function is directly dependant upon the first and second invariants of the unimodular component of the left Cauchy-Green tensor. In particular, defined these invariants as [25]:

$$\overline{I}_1 = J^{-2/3} I_1 \tag{74}$$

$$\overline{I}_2 = J^{-4/3} I_2 \tag{75}$$

where J is the determinant of the tensor **F**, the strain energy density function can be defined as [25]:

$$W = \sum_{i,j=0}^{N} C_{ij} (\overline{I}_1 - 3)^i (\overline{I}_2 - 3)^j + \sum_{k=1}^{M} D_k (J-1)^{2k} \tag{76}$$

where C_ij is a material constant, obtained from experimental, data related to the distortional response via the shear modulus, μ, while D_m, also a material constant, is related to the volumetric response via the bulk modulus, κ. For a compressible material, such as common rubber, $N = M = 1$ and the strain energy density function becomes [25][26]:

$$W = C_{01}(\overline{I}_2 - 3) + C_{10}(\overline{I}_1 - 3)^j + D_1 (J-1)^2 \tag{77}$$

So, for the COMSOL model, the three material constants had to be found for the silicone rubber and the air gap. For the sake of simplicity, silicone rubber was assumed to have the same mechanical properties as common rubber. Owing to this, since the bulk modulus of rubber is known from literature, it was immediately possible to calculate D_1 constant, given that this is related to the bulk modulus by the relation: $\kappa = 2D_1$. Regarding the other two constants, they are defined as $\mu = 2(C_{10} + C_{01})$. Since the shear stress for rubber is also known, all that was necessary for the estimation of these constants was finding plausible values for them from the literature. C_{10} was assumed to be equal to $0.37MPa$, while C_{01} to $0.11MPa$.

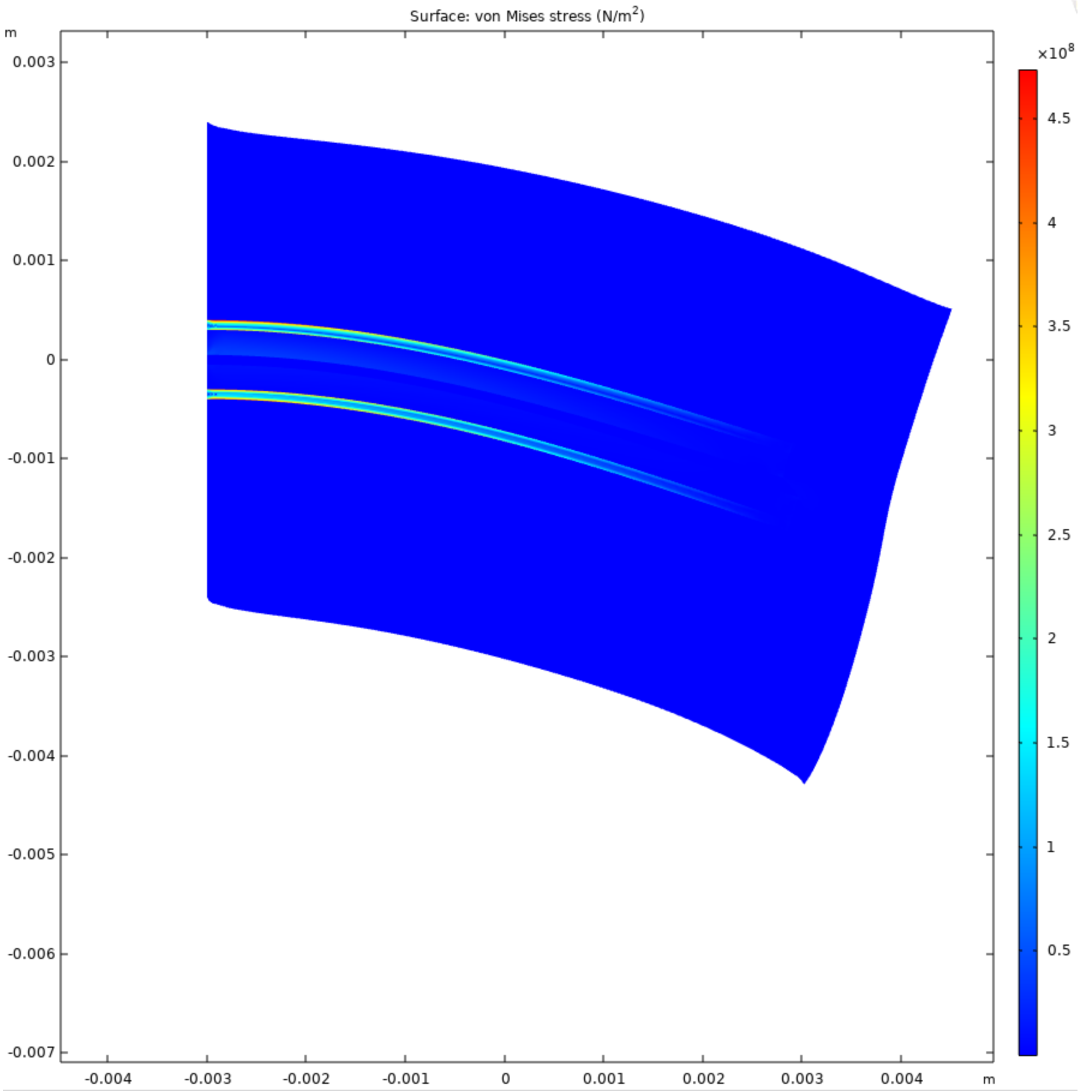

Figure 23: 2D domain of the new "edge chamber" COMSOL model.

For the air gap, a bulk modulus of 1 atm was considered, from which the D_1 constant could be immediately obtained. As for the other two constants, they were derived from those of the silicon rubber, scaled down to a twentieth of their values. For the dielectric layers, the same non-linear elastic material properties were chosen as in the previous models,

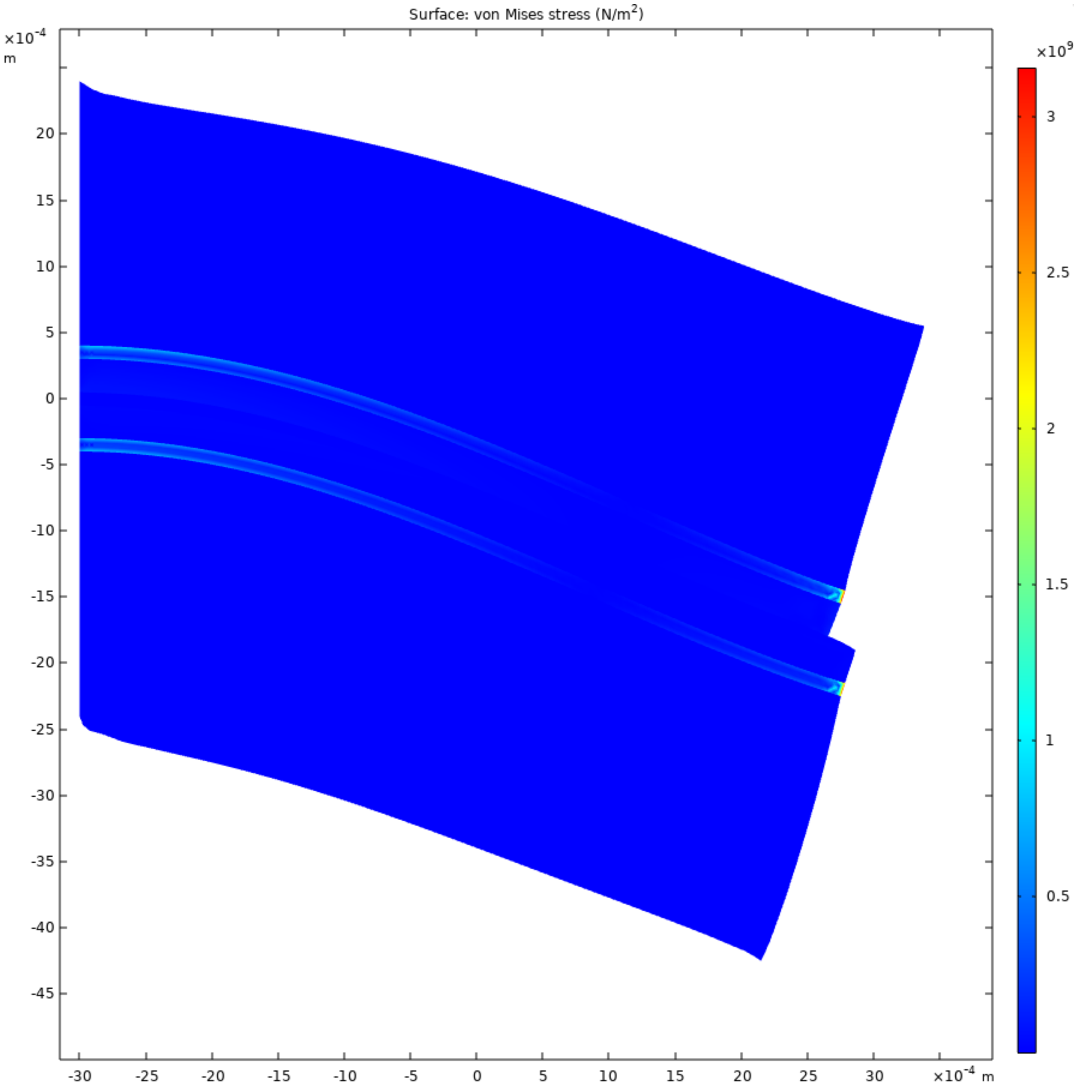

Figure 24: 2D domain of the new "middle chamber" COMSOL model.

while for the copper layers the linear elastic material property was obviously still valid. The loading condition was the same as the previous simulations: a concentrated vertical load at the element free edge, with the other edge costrained through a clamp.

In **Figg. 23** and **24**, are represented the two models with the new mechanical properties for the silicone rubber and for the air layer. As evident from both figures, the issues already present in the first models, represented themselves in the new ones. The bending curvature was not constant neither in the middle chamber nor in the edge chamber model along the x-axis direction (longitudinal). Same as with the previous simulations, shearing was observable in both models: as a matter of fact, it was even more accentuated than before, due to the higher displacements allowed by the mechanical properties of the hyperelastic material model adopted for the silicone rubber. What changed now is that, while for the edge chamber element model the peak stress was reached at its constrained end, along the copper layers of the triboelectric sensor and same as with the first simulations, in the middle chamber model stresses were the highest at the free end of the element. For the same reasons as explained in the previous subchapter, shearing deformation came visibly in the form of sliding for the middle chamber element model, with its lower half sliding underneath the upper half. Again, the fact that the load was being applied at different cross sections of the two models also meant that the shear stresses were significantly different at the end cross sections of the triboelectric layers.

So, while on one hand the extent of vertical displacement achieveable by these new models was far greater than that of the previous ones and was also closer to what could be observed in the experimental testing of the prototypes built in chapter 2, most of the flaws registered in the first simulations still persisted. The problem was addressed in stages: first it was necessary to eliminate the presence of shear stresses anywhere in the various layers which consitute the device, then it was necessary to guarantee constant or near constant bending curvatures along the whole length of the device. The first problem was of immediate solution, instead of analysing a single portion of the robot-embedded triboelectric sensor the length of a single chamber, the whole triboelectric device was to be analysed at once. As for the second problem, with the COMSOL software it is not possible to impose the bending curvature on a beam that is being deflected by an external load. For this reason a distributed load was applied on the uppermost layer of the device, i.e. the exposed top surface of the soft robot body, and whose value was the same as the pressure of the chambers time the total area of the bases of the chambers. To have a constant curvature along the x-direction, once the value of the force was known, a simple equation was assembled so that the arctangent of the vertical displacement to the x-coordinate ratio remained the same from the constrained end to the free end of the element model.

In **Fig. 25** is reported the result of the new simulation for the element model in its entire length. As immediately noticeable, every point on the cross section at the free end of the model sits on the same plane, or in other words, all points on said section can be identified by a set of outward-pointing parallel normal vectors to the local surface surrounding each point. In this model, the height to length ratio was obviously significantly greater than the 1/10 minimum limit imposed by continuum mechanics. This prevented shear stresses to be considered negligible at any section of the device, which explains why at the element free end all points could be described by the same normal vector. It is important to mention how the peak stress is reached approximately at the middle section along the x-direction of the model, which is actually a result to be expected given the way the robot bends. From this middle section moving towards the two ends, stresses show symmetrical behaviour at cross sections placed at the same distance from the middle section along the x-axis direction. In the previous models, not considering shear stresses at the free extremity, the peak stresses were only ever reached at the constrained end of the element where the continuity of the material was interrupted by an ideal cut of the cross section that is normal to the x-axis of the longitudinal direction. If one were to ideally cut the element of **Fig. 25** in a finite number of n-elements, each having the same length as the others, consistent results would be observed for each i-element. Going by that logic, proceeding to cut the model until the element of the fixed reduced length has one of its ends coinciding with one of the two edges of the soft robot, the constrain would have to be placed precisely where the continuity of the material is interrupted by this cut, that is in the same section as the one depicted in **Figg. 21** and **23**. Moving from the extremity towards the centre of the device, the two

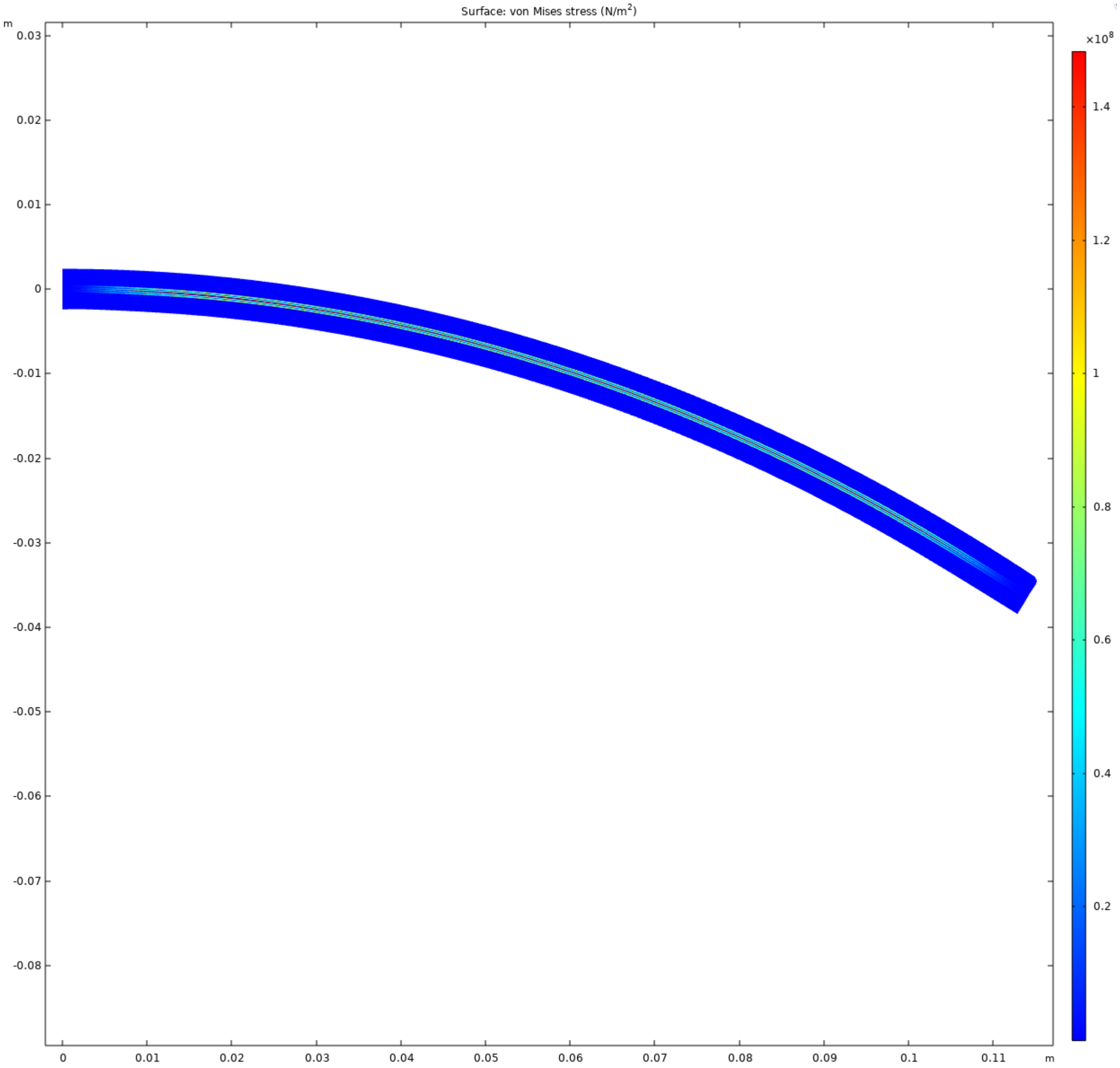

Figure 25: 2D domain of the COMSOL model for the device in its entirety.

element edges thus show analogous trends for the distribution of stresses along the x-axis, which again is a behaviour that is to be expected given the nature of deformation in soft robots. Regarding the distrution of stresses along the y-direction of the xy plane on which sit the 2D domain of the element model, this is quite different from what had been observed in the previous simulations. With the change in mechanical properties, the thickness of the each layer constituting the triboelectric device was kept constant moving from one layer to the other; in the previous models, the dielectric layers were more than twice as thick as the copper and air layers, which meant for higher stresses to accumulate on the thinner layers. Now, as said, every layer presented the same thickness and the higher stresses along the y-direction were reached in the interface bewteen dielectrci layers and air gap, at the middle cross section along the x-direction. This of course is physically impossible, but is a consequence of the limitations of the COMSOL software, which does not allow the use of gas-like properties for a given part of the model in the study of structural mechanics. So, having to adopt a solid material model for the air gap came with the distribution of stresses also along the whole length of the air gap itself. Other than the distribution of stresses, the mechanical properties of the air gap also affected the vertical displacement under the external load.

In **Fig. 14** is a prototype of the actuator built in the material whose mechanical properties were chosen for the simulation of the behaviour of the device under inflation. Comparing the extent of deformation in the physical propotype with that of the simulation model, it becomes apparent how the former presents displacements along the x and y directions which are far greater than those of the latter. Two factors are at play here. In **Fig. 14**, the strain limiter was still the paper sheet placed at the lower half of the body robot; common paper is usually 0.1 mm thick. The triboelectric sensor, in its more basic design as presented in **Fig. 2** is decidedly thicker than the original paper strain limiter: each layer of the device can be assumed to be about 0.25 mm thick, that is, 1 mm thick for the whole sensor, excluding of course the air gap. Having a strain limiter ten times as thick as sheet paper and with mechanical properties that are far stiffer than paper means that the vertical displacement caused by the same external load acting upon the device is reduced in the tribo strain limiter as compared with the paper strain limiter. Still, the physical sensor-embedded prototypes showed significantly larger vertical displacements than what is being depicted in **Fig. 25**, even though the distributed load of the simulation was derived to be the same as the equivalent load in the physical prototype caused by the inflation of the chambers. This is where the second factor, the air gap mechanical properties, affects the behaviour of the device during deformation. In the physical prototype air obviously has gas-like mechanical properties: given that pressure in the air gap between dielectric layers stays low even at the maximum vertical displacement when the two dielectric materials are forced into contact, the resistance exerted by air can be considered with good approximation to be basically negligible in its effects on the deflection of the robot. In the simulation model, though, the air gap is assumed to behave like a solid, specifically like a hyper-elastic material whose constants in the Mooney-Rivlin solid model are derived from those of the polydimethylsiloxane of the robot body. So, with greater mechanical properties than a gas, the simulation model air gap significantly reduced the vertical displacement achieveable with the same vertical load. Even with the limitations just described and owing to the fact that some of the issues proper of this model could not be circumvented, specifically the adoption of solid-like mechanical properties for the air gap, the model could be considered a good enough tool to study the behaviour of the device during deformation.

3.3.3 Electrostatics models study

Once an adequate model for the study of the mechanical behaviour of the device was found, it was finally possible to focus the attention on the electrical properties of the triboelectric sensor. The problem at hand follows the equations of **part 3.1**. As already explained, the boundary conditions for the 2D domain of the element model had to necessarily be in the form of Neumann conditions, which in the electrostatic problem correspond to the definition

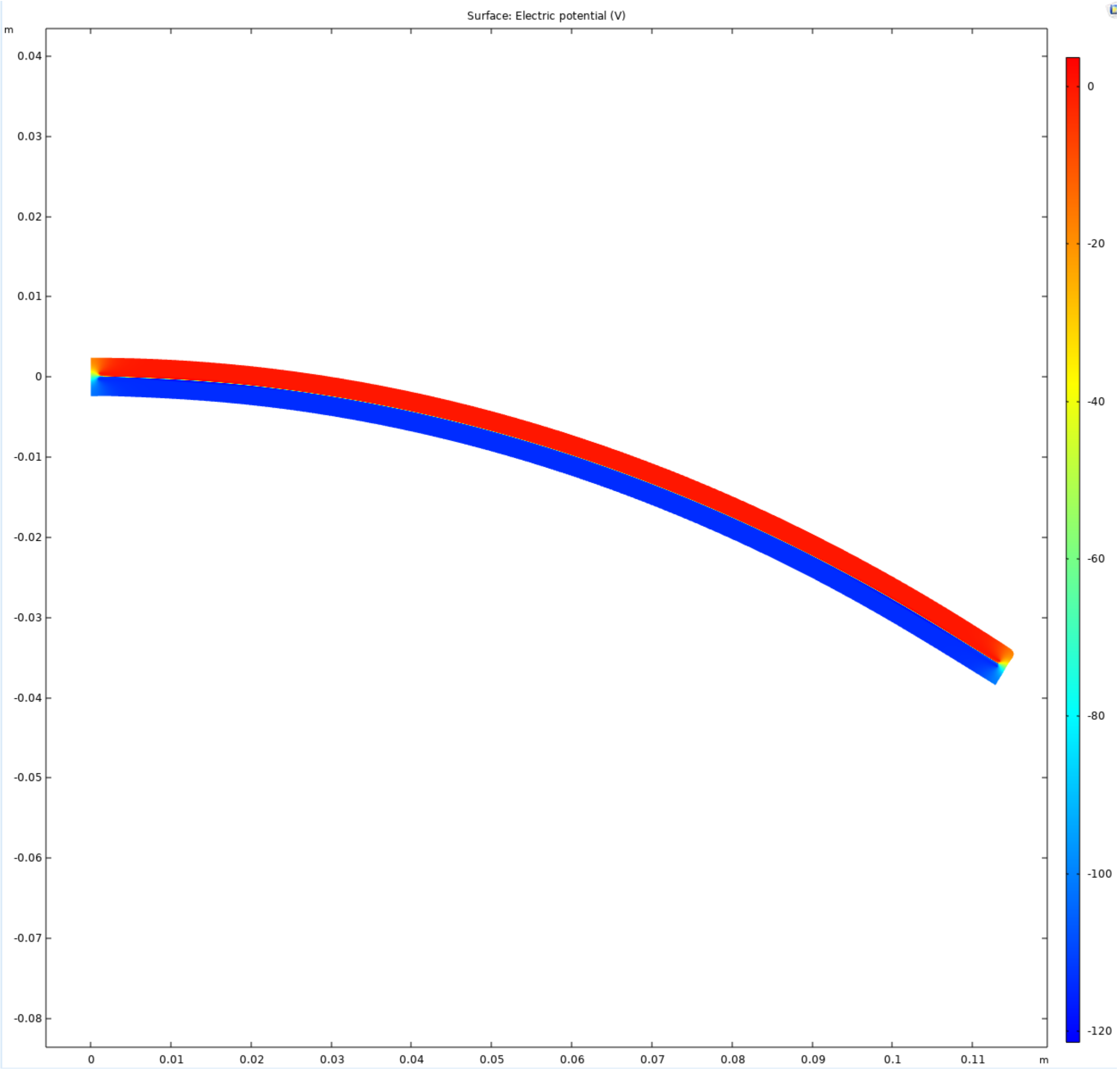

Figure 26: Electric potential of the COMSOL model for the device in its entirety.

of a surface charge density on the boundary. This is achieved in two different ways: a first one is to banally assume a uniform distribution of charges on the inner surfaces the two dielectric layers, which given the electrical properties of TENGs is a valid assumption as already explained in the previous chapters. So, for the upper layer of dielectric material, Kapton, an arbitrarily chosen density of $10\mu Cm^{-2}$ was assumed, while for the lower one, nylon, the density was set at $-10\mu Cm^{-2}$. The second way in which the Neumann conditions could be implemented on the element model, was to establish a reference state for the electric potential and a floating potential at a different feature of the domain to represent the effect of the electric field on said feature. Since the purpose of this work is to find a way to correlate the deformation of the soft robot with the electric potential measured at the electrodes of the triboelectric sensor, it was obvious that one of the electrodes had to represent the reference state while the other had to have a floating potential condition to evaluate the variation in potential from the undeformed position to the deformed one after inflation. Specifically, the upper copper layer constitutes the reference electrode, while the lower copper layer is used to measure the voltage at different stages of deflection from the reference state, so it is where the floating potential boundary condition is set. This is in analogy with the structural mechanics study of the previous part: using a reference state for one of the electrodes is the electrostatic equivalent of placing a constraint in a structure, while considering a floating potential for the other electrode is the electrostatic equivalent of allowing the structure to show displacement under the application of an external load. The surface charge densities on the two dielectric defines the electric potential difference between the electrodes from the outset. The deformation of the robot forces the layers to come into contact prompting the redistribution of charges on the two inner surfaces of the dielectric materials, thus causing a variation on the electric potential difference at the two electrodes of the device.

Same as with the structural mechanics study, also at these initial stages of the electrostatics study the condition of the system is static. The vertical load corresponds to the pressure at the maximum value of volume V_a of air injected into the chambers, so the observable electric potential trend in the element model also corresponds to the configuration of maximal expansion of the volume of the air chambers, i.e. maximal vertical displacement at the strain limiter. In contrast with the mechanical study of the device, where for the air gap between dielectric layers solid-like properties had to be chosen for the simulations to run, for the electrostatic study the COMSOL software allows for the air medium to have the actual electrical properties of air. Thus, it was possible to define, for the stratum separating the two halves of the triboelectric sensor, the usual properties of air, that is, its relative permittivity ϵ_r.

In **Fig. 26** is the electric potential in the 2D domain of the element model. From that figure, the upper half of the robot presents surface voltages of 0 V due to the presence of the reference electrode which fixes the voltage to that value. The lower half presents of voltages of about -110 V, -117 V to be more specific, in the condition of maximum deformation from the steady-state. As said, the electric potential difference is for the system in a static condition of loading and it is function of the surface charge density assumed for the upper dielectric layer and for the lower dielectric layer. For this reason, if different values of the surface charge densities were assumed for the two dielectric materials, even with the same amount of vertical displacement, the electric potential difference generated between the two electrodes would change accordingly with the new densities of charges on the surfaces. Of course, what matters is the electric potential difference measured at different levels of deformation from the undeformed configuration. Obviously at this stage this cannot be assessed yet, but it will be once the study of the behaviour of the robot is extended to the consideration of time-dependent cycles of loading. Going back to **Fig. 26**, both halves of the silicone rubber encasing the triboelectric sensor show the same values of the surface voltage as the two electrodes of the sensor. This is obviously a consequence of the dielectric properties of silicone rubber: the presence of an electric fields generated by induces the generation of polarised charges, these charges accumulate in accordance with the field lines of the electric field. In the system of **Fig. 26**, charges accumulate such that in the robot half corresponding to the reference electrode, the same electric voltage as the electrode is reached by the material surrounding it, and the same happens with the other half of the robot where the silicone rubber presents the same electric potential as the second electrode. At the two ends of the robot body encasing the triboelectric sensor, the surface electric potential trend is similar to that observed in the air gap between the dielectric layers.

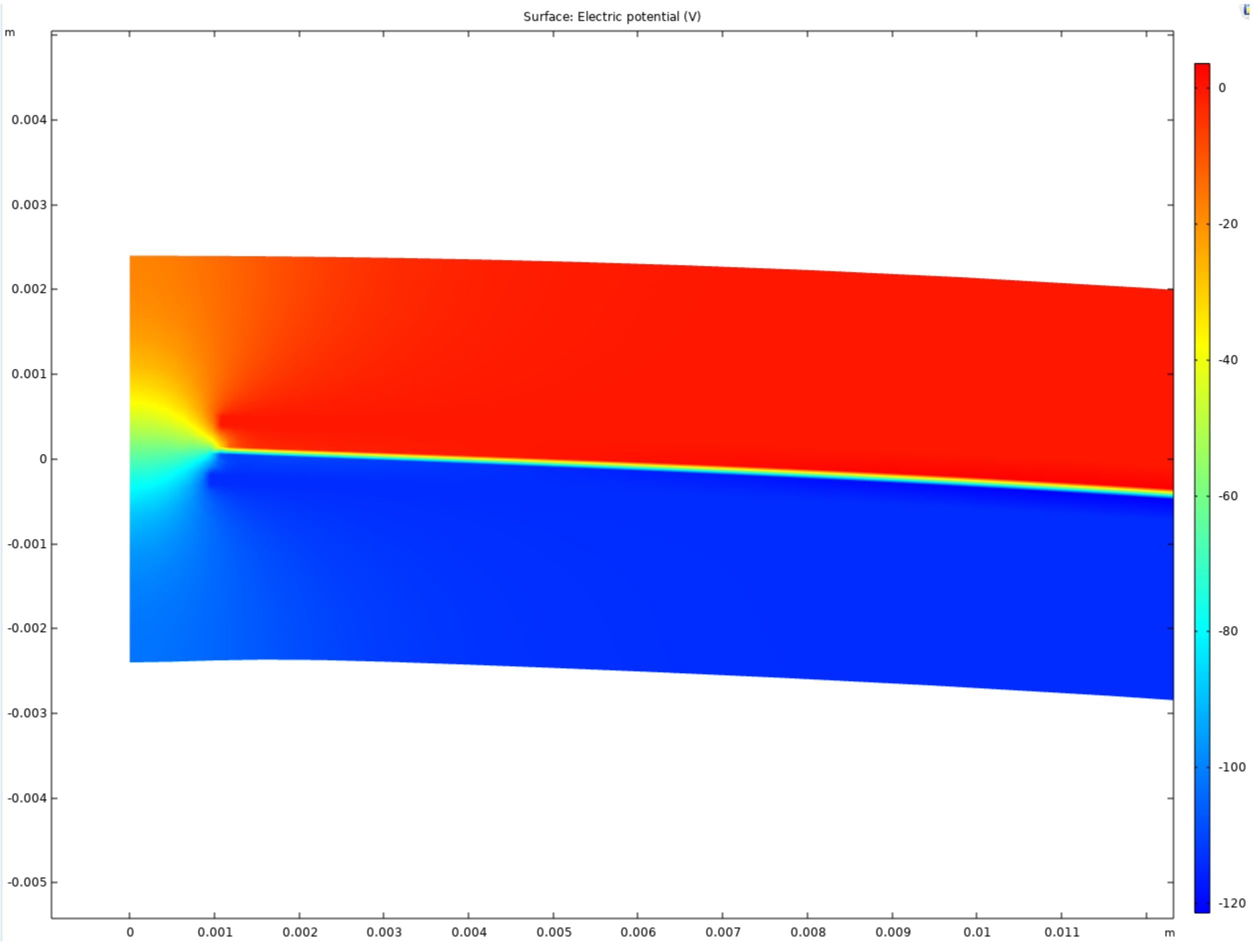

Figure 27: Detail of the surface electric potential of the COMSOL model.

In **Fig. 27** is a detail of the model of above which shows the surface electric potential trend in the device. The two darker spots in the left are the electrodes of the triboelectric sensor: in dark red is the reference electrode and in dark blue is the other electrode. These electrodes of course run through the whole length of the robot body, but given the dielectric properties of the silicone rubber, they are only ever discernible at the very ends of the robot, where the surface electric potential of the polydimethylsiloxane goes from the value of the reference state to that of the other electrode. It's precisely the colour contrast generated by this transition of the electric potential in the silicone rubber that makes it possible to identify the two electrodes in the darker spots on the left. As for the dielectric layers and the air gap separating them, the same transition is observable. The behaviour shown by the simulation as it is already makes the case for the introduction of a shielding coat between the triboelectric sensor and the silicone rubber in order to avoid the dielectric polarisation of the robot body, which could potentially affect the measurement of the electric potential difference at the two electrodes.

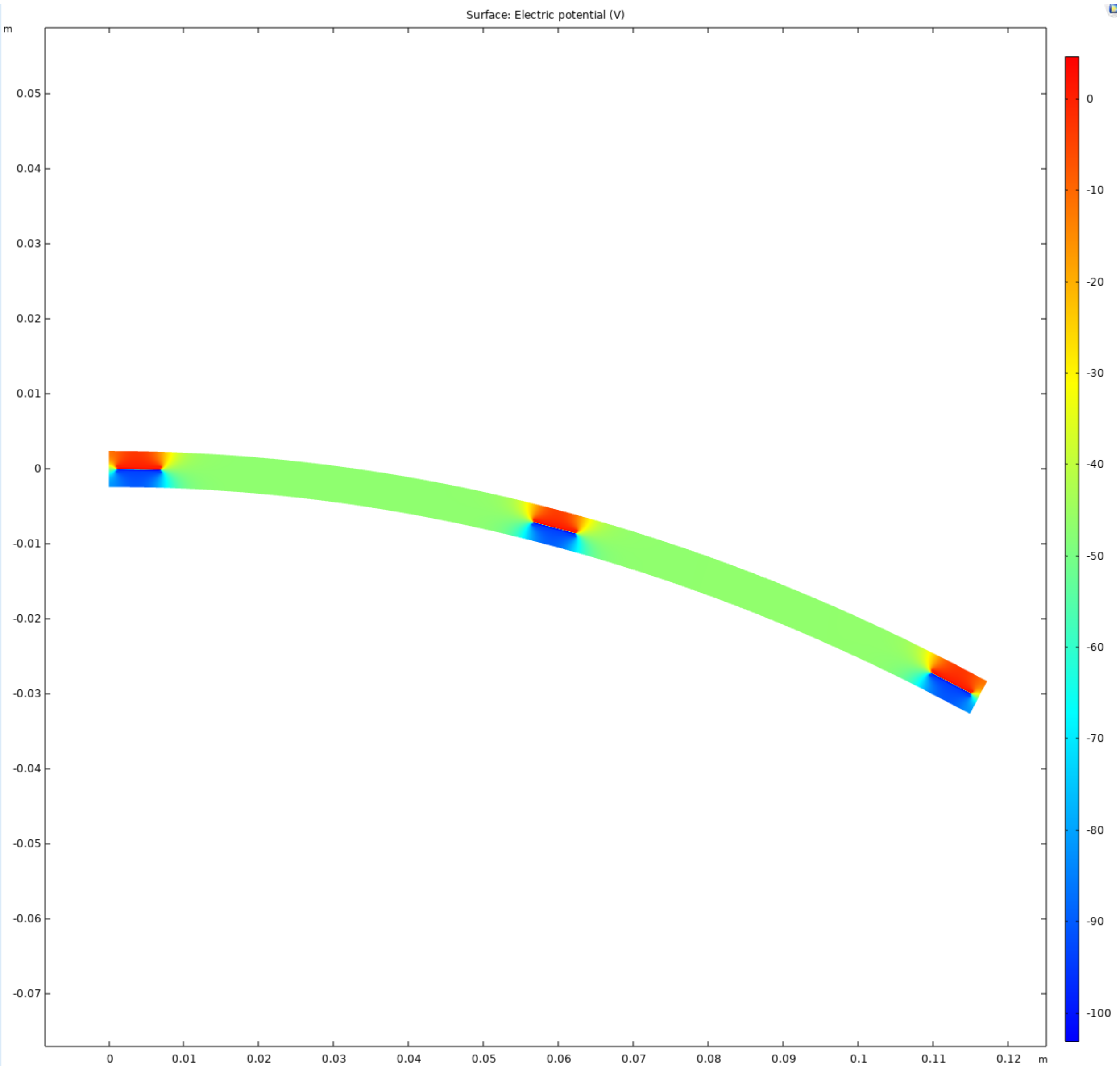

Figure 28: 2D domain of the COMSOL model for the device in its entirety.

In chapter 2, several prototypes were developed to find the best fit for the triboelectric sensor to be encased into the robot. One of such prototypes was built cutting the triboelectric sensor in three parts and placing each part at different positions inside the robot. Specifically, these smaller parts, working as different triboelectric sensors, were positioned at the two ends of the robot body and at its centre. In **Fig. 27** is the result of the simulations for this different prototype of the robot-embedded triboelectric sensor. Non visible, is the strain limiter running from one end to the other of the robot body along the x-direction. Same as in the physical prototype, here too the strain limiter is a sheet of nylon. Other than the robot strain limiter, this sheet of nylon is also one of the two dielectric layers of each one of the three sensors. In this model the dielectric behaviour of the silicone rubber is even more evident than in the previous one: in correspondence with the triboelectric devices, due to the presence of electric fields, the polydimethylsiloxane polarises, going from the same potential of the reference electrode to the potential of the second electrode in the portions of the material surrounding them. Between the triboelectric sensors, the surface electric potential in the silicone rubber reached the middle value registered in the air gap between the dielectric layers, which is halfway between the value of the reference electrode and the value of the other electrode.

4 Comparing the results

4.1 Introduction

As mentioned before, the scope of this work is to study the usability of soft robot-embedded triboelectric devices as deformation sensors for soft robots. In the previous chapter it has been shown how, once derived the governing equations of the triboelectric problem, it is possible to simulate the behaviour of triboelectric nanogenerators under the influence of external loads by correlation of the distance between the active layers of the tribo-pair and the potential difference at the electrodes, at any given time. For soft robot-embedded tribolectric devices, this distance between active layers is a function of the deformation of the soft robot encasing them, under the inflation of its air chambers. In its steady state, the system presents a potential difference at its electrodes that is function of the distance between active layers at time t_0 and of the surface charge density on the active layers of its triboelectric part; when an external load is applied on the system, in this study case in the form of an inflation of the robot air chambers, the distance between active layers changes and so does the potential difference. When the load is released, the surface charge density reverts to its initial value, same as the electric potential. In the simulation environment, with the models as described in the previous chapter, it is possible to have a measure of this change in the potential difference consequence of the deformation of the soft robot.

Simulation results alone are not enough to assess the merits of this triboelectric sensor-soft robot system as a way to correlate deformation with electric potential difference at the sensors electrodes. To better study the problem, it is necessary to compare these simulation results as obtained in **chapter 3**, with the behaviour of tailor-made prototypes working under external loads. Therefore, to study the feasibility of ”real life” sensors, in **chapter 2** it was described the step-by-step process adopted to design and built soft robots and triboelectric sensors, as well as the various assembling attempts for a functioning prototype of a soft robot-embedded triboelectric sensor. In this purpose, these three configurations were built for the assembled device:

1. *single layer contac-mode triboelectric nanogenerator*;
2. *three-way split layer contact-mode triboelectric generator*;
3. *sliding-mode triboelectric nanogenerator*;

Similarly, in the simulation envirnoment, three models were built for the same three configurations.

In the following pages are shown the tests conducted to study the behaviour of both the ”real life” prototypes and the COMSOL models. The tests are going to be described for the two environments in which they were carried out: the Purdue laboratories for the formers and the simulation environment for the latters. The comparison of the tests results between each type of prototype and its model counterpart is given at the end of this chapter. This comparison is of particular importance for several reasons, first and foremost since it represents a valuable instrument to evaluate the accuracy of the COMSOL models as compared with the "real life" system. Evaluating to what extent the former is capable of simulating the behaviour of the latter is of paramount importance since it enables us to predict the behaviour of more sophisticated prototypes for the system as intended, as well as giving useful information in regard to potential issues with the system itself. So, once the accuracy of the COMSOL model is assessed, this comparison of results can also be used as a way to appraise the actual capabilities of the system to accomplish the afore mentioned task of deformation sensor in soft robots. The comparison could also be useful to determine whether the device could be implemented in systems which extends beyond the realm of soft robotics.

4.2 Testing the prototypes

Let us consider the prototype shown in **Fig. 22** of **chapter 2**. Every prototype built is a soft robot in the form of a pneumatic actuator which deforms as a consequence of the inflation of its air chambers. In these kinds of actuator, a certain volume of pressurised gas is injected via a pipe into the chambers to achieve the intended deformation which could be used as a mean to produce several effects, ranging from motion for particual kinds of soft robots, to good grip for when the soft robot is used to grasp firmly delicate objects. Too big of a volume injected, and the robot could tear at the air chambers or in other vulnerable parts of its body; too small of a volume and the robot wouldn't be able to execute the tasks for which it was built.

For the two materials adopted for the soft robot body, EcoFlex and Mold Star mixtures, both presented elongations at break higher than 400 %. Given this property, the soft robots built with a strain limiter made of paper presented significant deformations during inflation before any laceration could form on their exterior walls. Most specimens could deform to such an extent that their two ends could touch each other as the robot inflated and bent downwards. Embedding the triboelectric sensor, with its thickness several times greater than paper meant that significantly smaller volumes of air could be injected before incurring in potential damages of the soft robot, notwithstanding the hyperelastic properties of the material.

In order not to compromise the material integrity of the soft robot bodies, the volume of air to be injected is measured with a graduated syringe. Therefore in all tests air is pumped into the chambers via a manual syringe connected with the air pipe insterted into the soft robot. Since the inflation is achieved manually, the rate of inflation as well as the amount of air pumped into the air chambers is non-constant for each cycle of inflation, as evident from the different heights of the peaks of load in the picture down below. Before testing, the external circuit of the device, given by the two copper foils visible on the left side of the device, is connected to an electrometer. At time $t_0 = 0s$, the device is in its undeformed condition and the electrometer, set to that reference state, reads zero as the potential difference at the electrodes' ends. The two dielectric layers of the triboelectric device are separated from one another by a thin stratum of air. In the picture below is shown a prototype being tested: on the left, behind the hand, is the electrometer, while on the background is the graph of the electric potential difference function of time. At each peak corresponds each impulsive load of inflation. As mentioned, the peaks have different heights due to the manually-controlled injection of air.

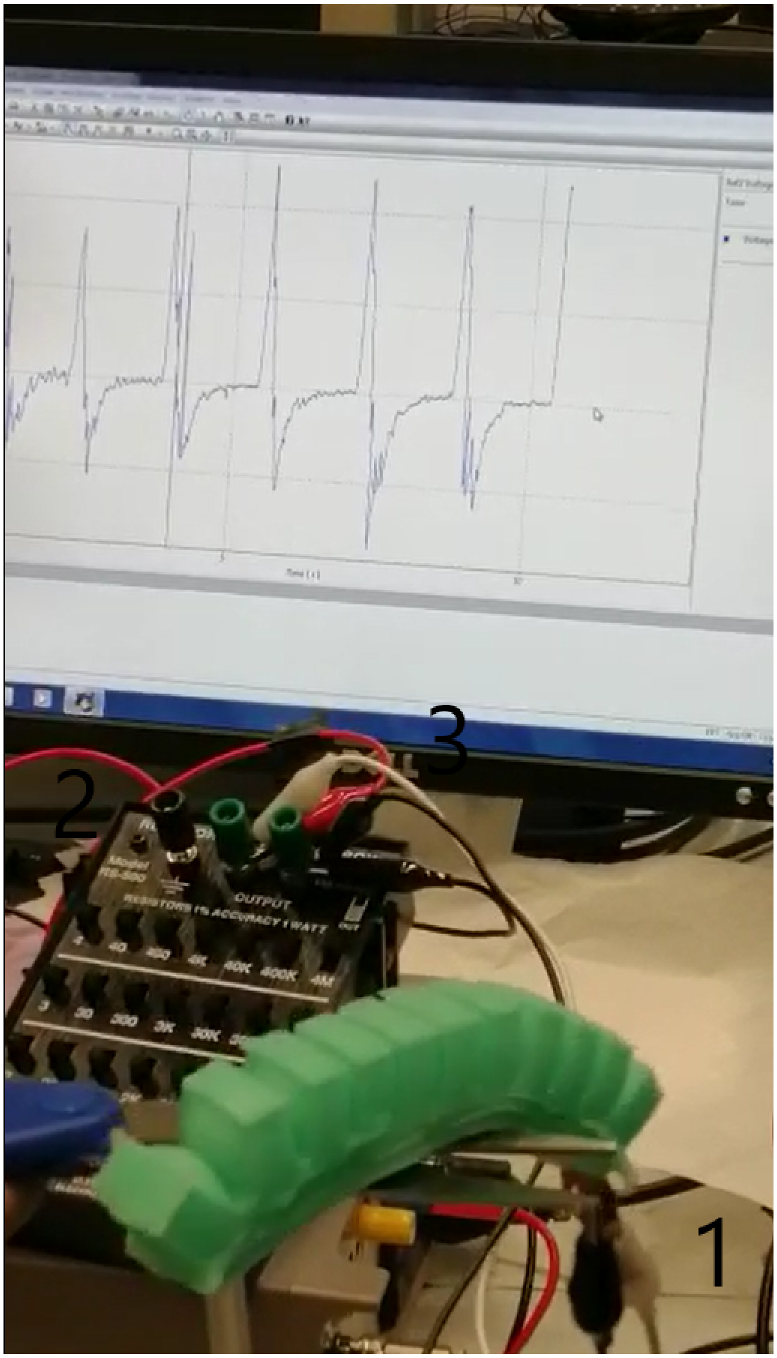

Figure 29: A prototype being tested. The black and white clips (1) connect the sensor electrodes to the resistance box (2), the red clip and the second black clip (3) connect the resistance box to the electrometer (not visible in the picture). The resistance box adds a 5 $M\Omega$ equivalent resistor in series with the circuit in order to reduce the voltage offset measured by the electrometer from the 0 V value.

When air is pumped into the chambers, the nylon layer limits the dilatation of the lower half of the robot body, which consequently bends downwards. As it bends, the layers of dielectrics of the triboelectric pair, nylon and Kapton, are forced into contact. This contact causes the accumulation of opposite charges on the interface surfaces of the dielectric layers, that is, as a result of contact one of the two surfaces will be positively charged while the other will be negatively charged. The two inner surfaces of the tribo-pair will present the same density of electrostatic charges of opposite charge. The triboelectrication effect is what causes these surface charges to be transferred between the two triboelectric materials. As air is pumped out of the chambers, the contact force is released and the two dielectric layers go back to their initial positions. As the air gap reforms, an electric potential difference is established between the two electrodes of the device. Via the extarnal circuit, charges will flow from the bottom electrode to the top electrode, in a short-circuit condition. After a certain time, the electric potential difference will revert to the steady state value, in our case to the 0 V value.

In the picture above the device is at the maximum deformation allowed by the material in the presence of the triboelectric sensor as the robot strain limiter. As mentioned in **chapter 2**, in order to avoid undesidered air leakage from the inflatable chambers, which would render the device unusable, the volume pumped into the chambers is set to a $15mm^3$ maximum threshold, which corresponds to a vertical downward displacement on the two ends of the device of approximately 3.5 cm from the undeformed configuration, or a degree of curvature for the soft robot of approximately 28°.

It is important to note that since the prototypes were all manually built and assembled, a constant air gap was impossible to ensure for each of these specimen. Therefore establishing a numerical correlation bewteen air gap and measured voltage could not be achieved.

4.2.1 Contact-mode triboelectric nanogenerator - single triboelectric layer

This is the simplest prototype amongst those designed and described in **chapter 2**. In this prototype, the triboelectric device runs throughout the whole length of the soft robot body. The soft robot bending forces the contact between the dielectric layers; as it inflates and deforms, a gradient in the air gap thickness can be expected between the tribo-pair along the x-axis of the device (see **Fig. 17** in **chapter 2** for reference). In this, the free end corresponding to the copper foils working as the external circuit of the sensor is the section where the air gap thickness is the least affected by the inflation of the air chambers.

As abundantly mendioned, the electric output of the device is function of the distance between the active layers of the triboelectric generator. The greater the initial distance, the greater the output. Having being manually built and assembled, in every prototype the air gap existing between the dielectric layers in the undeformed condition is not-constant along the xy plane on which it ideally rests. Due to the bumps and dips which are consequence of the curing process of the mixture in which the soft robot is built, the dielectric layers are therefore unevenly laid on the mixture surfaces. This means that with the manufacturing processes adopted to build and assemble the prototype, it is not possible to control the initial air gap thickness as well as ensuring that in no section on the zy plane the dielectric layers touch in their undeformed state.

Having said that, in the prototype in question, the initial distance between the tribo-pair can be assumed to be around 2 mm. Consequently, given the small entity of the air gap, the potential voltage measurable with the electrometer has to be quite contained. For

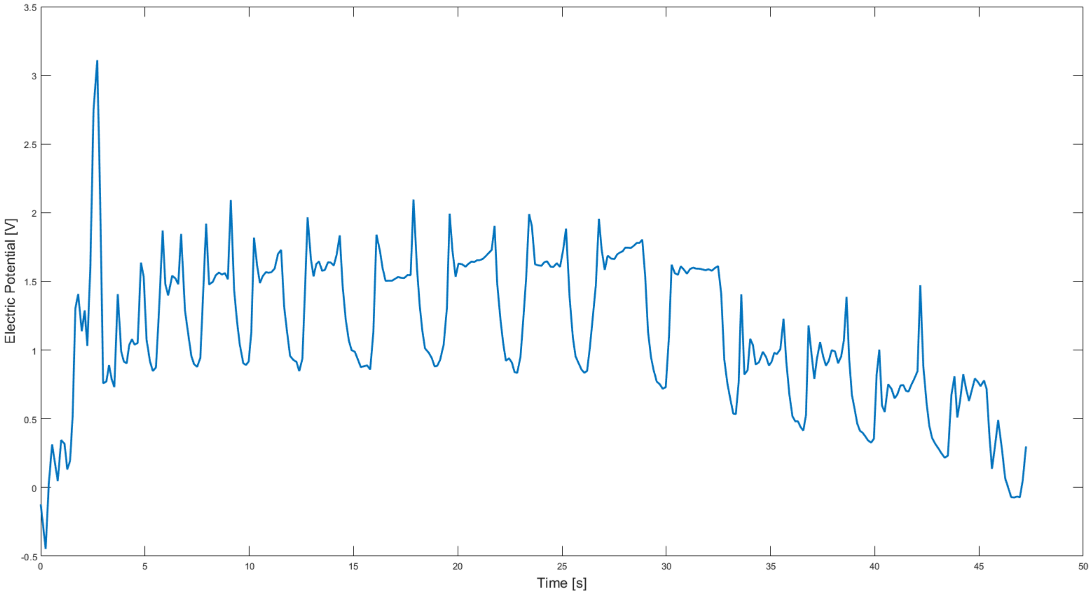

Figure 30: Electric potential difference during inflation.

the tests, the reference state is set to 0 V. In the figure above are shown the result of the electric potential difference trend of the first test, for each cycle of inflation. The first cycle corresponds to the highest peak of electric potential. From the reference state, a 3 V electric potential difference can be inferred for the highest deformation admissible of the soft soft robot; the sequent cycles hover around the 2 V value. As said, in order to not damage the specimen, for each of these cycles, a volume of approximately $15mm^3$ of air is pumped into the chambers. Of course, as the air injection is done manually, it is not possible to achieve the same level of deformation at each pumping and therefore it is impossible to reach the same values for the electric potential for each cycle of inflation. Except for the first inflation where the load is impulsive, the duration of every other cycle is prolonged, this was done as a way to also test the endurance of the soft robot material. Moreover, always concerning its endurance, the prototype is not left to completely deflate after each cycle of loading, hence the offset from the reference value in every cycle of load after the first one .

A second test was carried out with periodic and impulsive loading condition. Unlike the first test, now the prototype completely deflates after each cycle. In **Fig. 31** is the electric potential difference graph for this test. Corresponding to a 3.5 cm deflection , the maximum EPD is registered in the last cycle, with 2.8 V from the reference state (0 V) and 4.5 V from the valley (-2 V). This valley is a sort of rebound effect of the electric potential after inflation, where the voltage does not go back immediately to the reference value when the load is released, but instead continues to decrease as the prototype deflates to a level far lower than the reference value of the undeformed condition; after a small transient, the voltage reverts to the 0 V value of the undeformed condition. The other cycles have EPDs of around 2 V - 2.7 V from the reference state and 3 V - 4 V from their corresponding valleys.

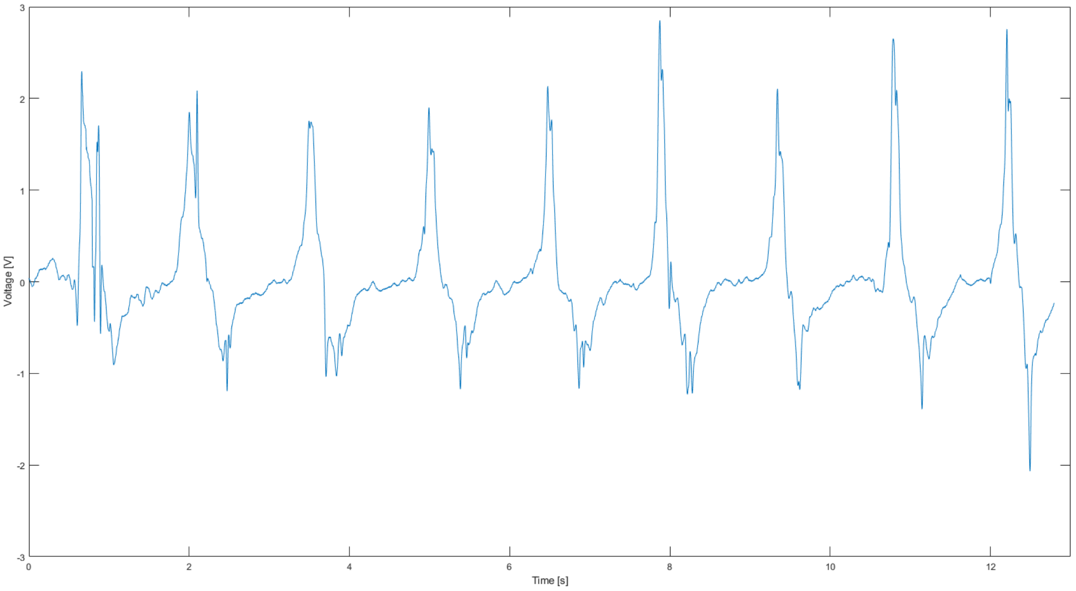

Figure 31: Electric potential difference during inflation.

From this first tests, the following observations can be made:

- The device is able to correlate deformation and electric potential;
- From the reference state, the peak value for the EPD is measured at 3.2 V, corresponding to an approximately 3.5 cm deflection at the soft robot free end for the first test, and 2.8 V for the second test;
- From the reference state, for every other cycle the EPD measured is around 2 V for a 2.5 cm deflection at the soft robot free end in the first test;
- From the reference state, for every other cycle the EPD measured is around 2 - 2.7 V for a 3.5 cm deflection in the second test;
- While a correlation can be inferred from the deflection of the soft robot, the same cannot be achieved with the air gap thickness between the tribo-pair since it is not possible to consistently measure and control the air gap at any stage of the building and testing phases;
- The collocation of the external circuit along the xy plane can affect the results of the test since the air gap is not-constant along the plane.
- Moreover, the air gap presents a thickness gradient during inflation due to the type of constraint acting on the soft robot. In future tests it would be interesting to examine how the results change depending on the positioning of the external circuit in respect with the constraint;

- Silicone rubber is a dielectric material so it can undergo the same polarisation of charges as the dielectric layers of the triboelectric sensor. This property certainly affects the test results; so the same tests should be carried out with the sensor properly insulated, as to reduce the effect of the silicone rubber polarisation on the results.
- Both the device assembling and testing are done manually. To reduce the human factor it is indicated to use a mechanised motor to control air pumping as to ensure the same volume of air to be injected during the same time span to increase the reproducibility of testings.

4.2.2 Contact-mode triboelectric nanogenerator - split triboelectric layer

Using the same basic working principle, i.e. contact-mode triboelectrification, a second prototype has been analysed. Since one the purposes of the study is to see if it is feasible to use the triboelectric device to accurately correlate the deformation of the robot during and after inflation whith the electric potential difference at the triboelectric sensor electrodes, some changes to its design have been applied as a way to reduce the effect of unevely laid dielectric layers and uneven thickenss of the air gap between them. Therefore, the triboelectric device has been split into three different smaller devices to measure the electric potential difference in different portions of the soft robot. This proves useful also in regard with the thickness gradient during inflation, consequence of the type of constraint acting on the device, as already mentioned before. One such sensor is placed at the centre of the device, one at the free end and one at the constrained end. The test results are shown below.

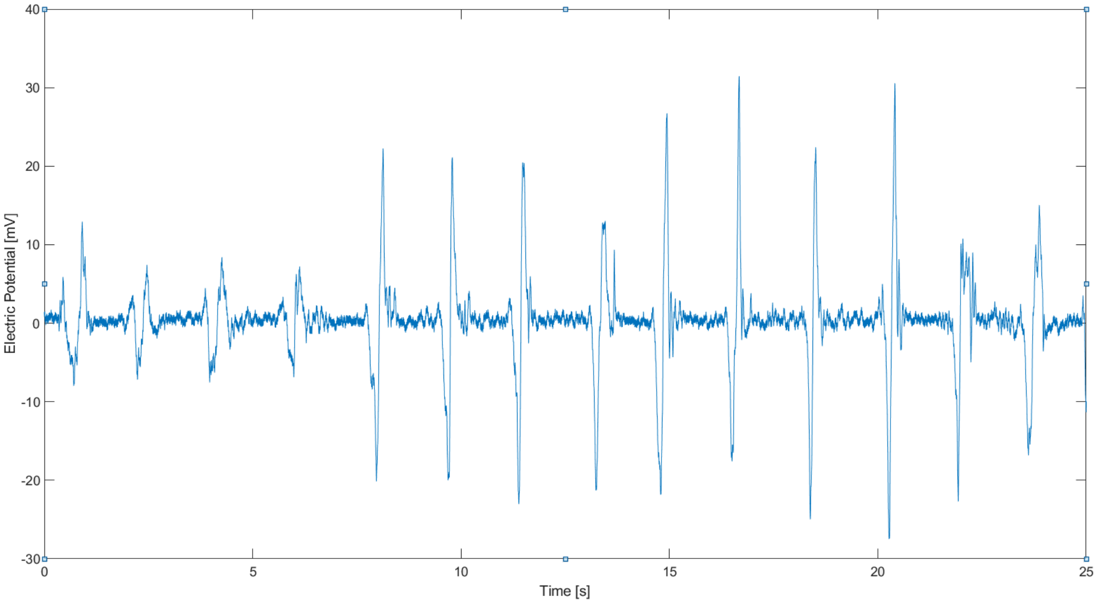

Figure 32: Electric potential difference during inflation for the central sensor.

Since in this prototype the noise was very tangible during the test, to obtain better results a cut-off frequency of $5Hz$ was used to eliminate background noise and the voltage was also scaled to a hundredth of its nominal value. A 5 $M\Omega$ resistor was also connected in

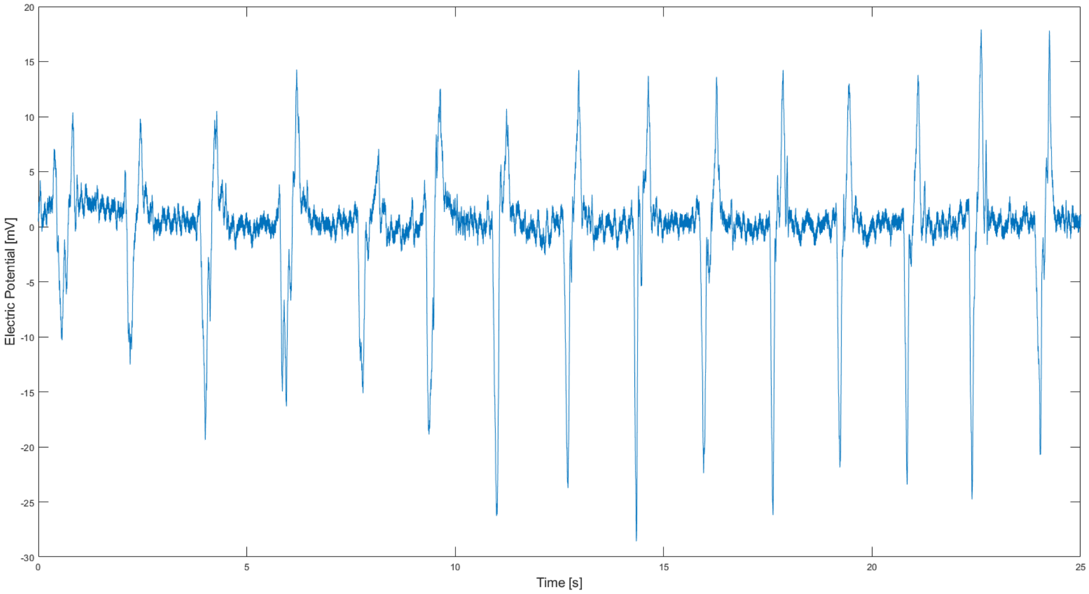

Figure 33: Electric potential difference during inflation for the sensor at the pipe end.

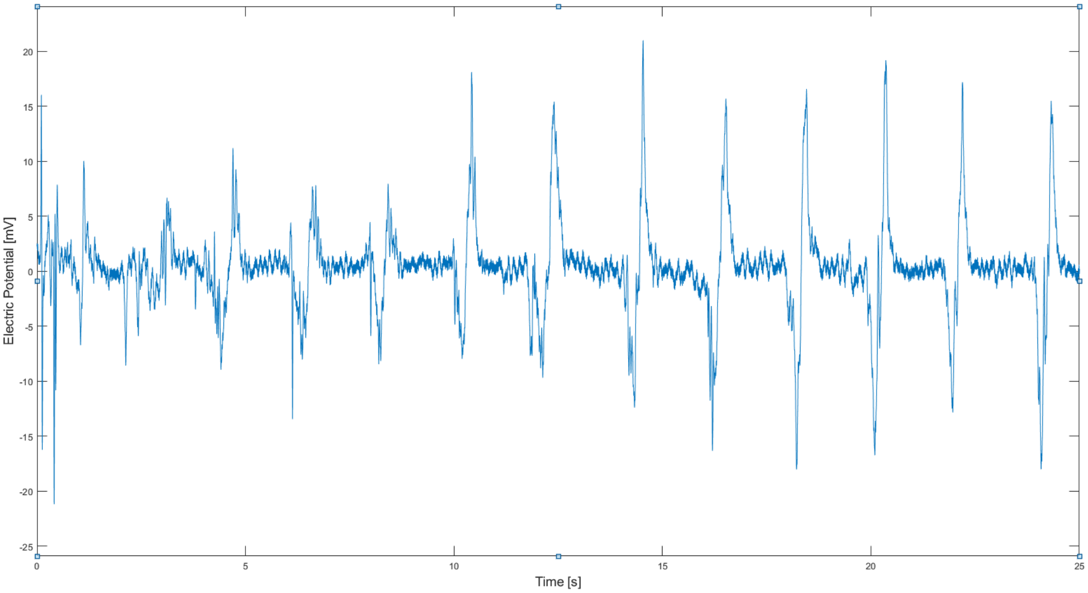

Figure 34: Electric potential difference during inflation for the sensor at the opposite end of the pipe end.

series with the circuit as to eliminate the systematic off-set off the 0 V value. This was done to be consistent with the previous measurements, where the reference state was set at that value. This way it was possible to eliminate the circuit noise to a great extent, making it possible to conduct the tests and get useful data with which to analyze the behavior of the device during inflation. As per the first prototype, also in this set of tests the inflation is achieved manually through a syringe. This time, though, having already tested the material endurance, the load (inflation) is always impulsive: each cycle lasts for about 1 s, with a volume injected of $15mm^3$ per cycle. Owing to the smaller dimensions of the triboelectric layers, the electric potential difference in this prototype is smaller than that of the first set of tests. In particular, in the center the peak EPD in a cycle is measured at around 58 mV. In the farthest end from the injection pipe, the peak EPD is measured at 43 mV, while at the closest edge it is measured a peak EPD of 36 mV, owing to the smaller deformations in proximity to the pipe. Since the strain limiter running throughout the length of the device consists of the nylon layer alone, deflection in this prototype is greatly increased, for the same volume of air in the chambers a deflection of 5 cm is reached as compared with the 3.5 cm deflection of the single triboelectric layer of the previous prototype.

A few observations:

- The sensors are able to correlate deflection with measured voltage at the electrodes.
- Measuring the electric potential difference at different cross sections yields different results owing to the air gap gradient caused by the type of constraint acting on the device;
- As expected, the peak value for the potential difference is measured in the central sensor since it is precisely there that the load forcing contact between the tribo-pair is the highest. On the constrained end the load is mitigated by the constraint itself, while on the free end it is mitigated by the non-continuity of the material;
- Due to the reduced dimensions of these sensors, the measurable voltage is smaller as compared with the sensor embedded in the first prototype. The reduced dimensions have a double effect on the measured EPD: on one hand they allow for a smaller charge density to accumulate during the polarisation of charges as consequence of the robot deflection. This reflects on the smaller potential difference established between the electrodes as the load is released. On the other hand, smaller dimensions increase the dielectric layers adhering, thus resulting in a reduced air gap thickness which in turn affects the measurable potential difference for the same principles as enunciated in the first chapter;
- Smaller dimensions also make the sensors more susceptible to circuit noise. The effects of the polarisation of the silicone rubber may also contribute to the noise as its influence on the triboelectrification of the device may be enhanced, reducing the accuracy of testing. It would be useful to insulate the sensor to have a measure of this effect on the test results.

4.2.3 Sliding-mode triboelectric nanogenerator

In the first two sets of tests, the sensors work by contact-mode triggered triboelectrification to gauge the deflection of the soft robots during inflation. As mentioned in **chapter 1**, this category of triboelectric generator/sensor is the easiest to build and assemble and it is also the one with the greatest electric output in relation with the external load applied to it. Sliding-mode triboelectric devices, on the other hand, present lower electric outputs under the same loading condition and they are also negatively affected by the reduced maximum distance allowed for these kinds of devices as compared with contact-mode ones. Nonetheless, building sliding-mode sensors would make it possible to reduce the device thickness as it would allow for the two tribo-pair not to be stacked one on top of the other as it was in the other prototypes.

Therefore, in the original intent, the last prototype tested was meant to use sliding-mode triboelectrification to trigger the triboelectrification of the sensor. This was to be achieved by designing the dielectric layer in a way that allowed it to glide on the electrodes as the soft robot bent under the external load, by ensuring its free motion along the plane on which it sits. So, in this prototype, the copper layers are coplanar, with the dielectric layer (nylon) sliding as the robot was inflated.

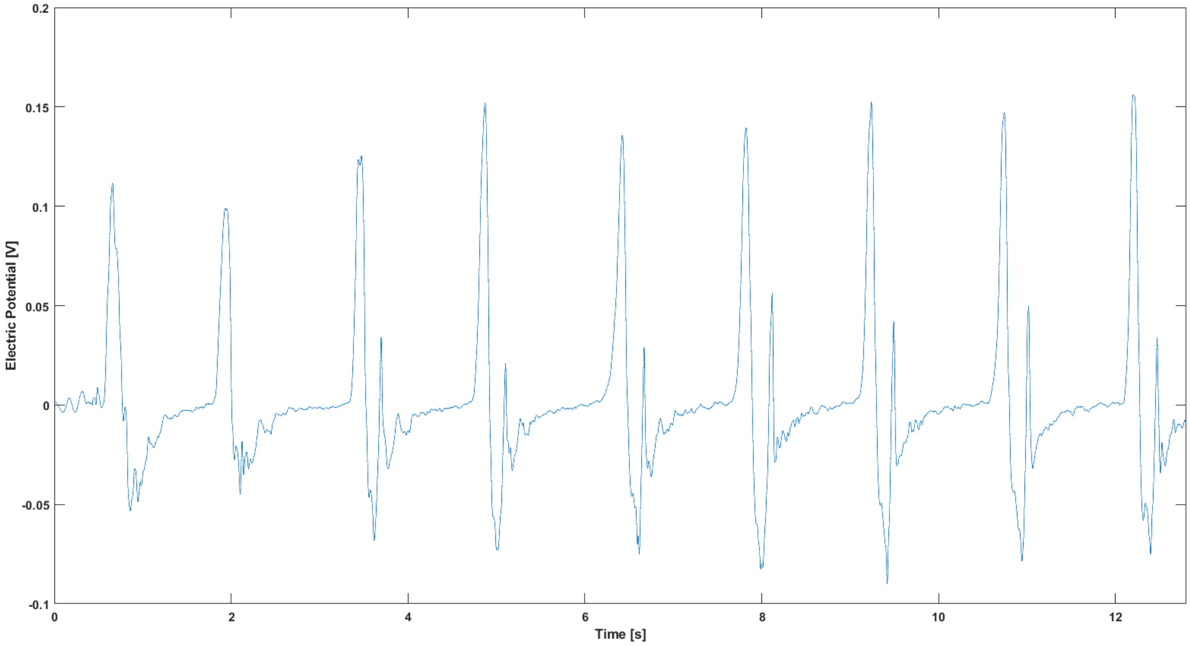

Figure 35: Electric potential difference during inflation.

Just like the previous set of tests, also in this case the circuit noise proved to be particulalry troublesome to conduct the test. It was again necessary to use a resistor to compensate the offset from the reference value and to cut-off frequencies higher than 5Hz and scale the voltage by a hundredth, as per the second prototype, in order to reduce the influence of the noise on the test results. The two copper foils of the external circuit emerge from opposite sides of the soft robot body, glued directly on each electrode and perpendicularly to their direction of maximum length, in those portions of the electrodes which are entirely covered by the moving dielectric layer during inflation. In **Fig. 35** are shown the results of the test for the prototype; as immediately noticeable, the peak electric potential difference is considerably smaller than that of the first prototype and closer to that of the second set of tests. In particular, the electric potential difference peak value was measured at 0.24 V. versus the 2.4 V of the first device. Unlike the first prototype though, this one proved to be more flexible due to its reduced thickness and thus more suited for this kind of applications where excessively thick sensors may hinder the robot ability to deform. The maximum deflection, although smaller that that of the second prototype, was 4.5 cm circa against 3.5 cm of the first prototype.

Some final observations on the behaviour of this prototype:

- much like the other two sensors, this one too is able to correlate deformation with voltage at its electrodes ends;
- though it was originally designed to have a sliding-driven electrification of the copper layers, in this prototype the electrification is still triggered by vertical contact. The planar motion of the dielectric layer, which is a given in sliding-mode triboelectrification, is extremely contained and the deformation of the robot has the same effect as in the other prototypes, i.e. forcing contact between the active layers of the device along the z-direction perpendicular to the plane. Unlike the other prototypes, though, here contact is established not between the two dielectric layers but instead between the only dielectric layer and the two coplanar electrodes. Thus, owing to the smaller exchange surface of the active layers, the measurable electric potential between electrodes is several times lower than that of the first prototype;
- the reduced measurable EPD is also a result of the reduced air gap thickness in the robot underformed condition. In a properly-designed sliding-mode triboelectric sensor this air gap effect would be negligeable on the polarisation of charges of the active layers, but since this prototype works under a contact-mode principle, then the initial air gap between dielectric layer and electrodes becomes as important as it is with the other two prototypes;
- also in this case the polarisation of charges of silicone rubber may have influenced the voltage gauging results;
- as mentioned above, its simple design allowed the robot to deform to a much greater extent under the same loading condition of $15mm^3$ volume of air injected as compared with the first prototype.

4.3 Simulations

Having tested the prototypes abilities to correlate deformation with electric voltage, the next step was running time-dependent studies on the various COMSOL models, as to compare the test results with the simulation results. For each prototype, the corresponding model was subjected to the same external load. Given that the deflection of the prototypes was known via direct measure during testing, the same value of deflection could be used during simulation to better adhere to the real life behaviour of each sensor. As described in **chapter 3**, the constraint is applied on one of the two ends of the model, while the other end is free from constraints. In order to achieve a periodic cycle of loading, the following sinusoidal equation was used:

$$y = -tan(\frac{x}{R})sin^2(4\omega t) \tag{78}$$

where R is the curvature radius of the soft robot during inflation. The curvature radius was changed for each model accordingly to the deflection measured for a given prototype, as to obtain consistent deflections between model and prototype. As for the angular velocity, it was arbitrarily assumed to be $30 rad/s$. The simulations duration was set to 25 s, a duration consistent with that of the tests. The tangent function was chosen to mimic the robot bending when one of its two ends are constrained: in the model the constrained end corresponds to the pipe-end of the prototype.

The mechanical properties of the materials are those enunciated in **chapter 2**:

- Mooney-Rivlin material properties for the silicone rubber and for the air layer separating the tribo-pair;
- non-linear elastic material properties for the dielectrics, nylon and Kapton;
- linear elastic material properties for the copper layers.

As mentioned in the same chapter, mechanical properties akin to those of solids had to be assigned to air too due to software limitations. The three models were thus created by taking direct inspiration from the prototypes. While for the contact-mode sensors it was easy to reproduce their functioning principle on COMSOL, for the sliding-mode model it was not possible to replicate the intended motion of the dielectric layer, so, much like its real life counterpart, this model too was contact-mode driven.

Regarding the electrical properties of the materials, one of the two copper layers is chosen as the reference state of the system while to the other electrode is assigned the "floating potential" property to evaluate the electric potential difference of the system under loading conditions. Nylon and Kapton represent the dielectric layers of the system, except for the sliding-mode model where only a sigle layer nylon is present. Arbitrarily, a surface charge density of 10 $\mu C m^{-2}$ is considered for the upper layer of dielectric, Kapton, while a -10 $\mu C m^{-2}$ for the lower layer of dielectric, nylon. This surface charge density is the same for the three models; the electric potential difference established in their steady state is obviously different considering the different surfaces of the tribo-pair: in the first model with the sensor running throughout the whole length of the soft robot, the electric potential different at time $t_0 = 0s$ is the highest, for the second model with the sensor split into three smaller sensors the electric potential at $t = t_0$ is the lowest, while for the third model it is mid range between the first two. As for silicone rubber, being a dielectric material, it undergoes the same polarisation of charges as the tribo-pair of Kapton and nylon in the presence of an electric field. This property is immediately noticeable by looking at the electric potential result of the COMSOL model.

In **Fig. 36** is represented the electric potential of the model at time $t = 14.5s$, when the robot bends under a cycle of inflation. To better distinguish between the various layers, black contours clearly separate each element of the model: the central yellow stratum is the air gap diving the tribo-pair; immediately above and below the yellow stratum are the two dielectric layers, nylon and Kapton and above and below them are the two copper layers with the same thickness as the dielectrics. Silicon rubber encases the sensor. In that figure it is immediately possible to pinpoint the reference electrode of the system, represented by the copper layer at the top (red); the "floating potential" electrode is the one at the bottom.

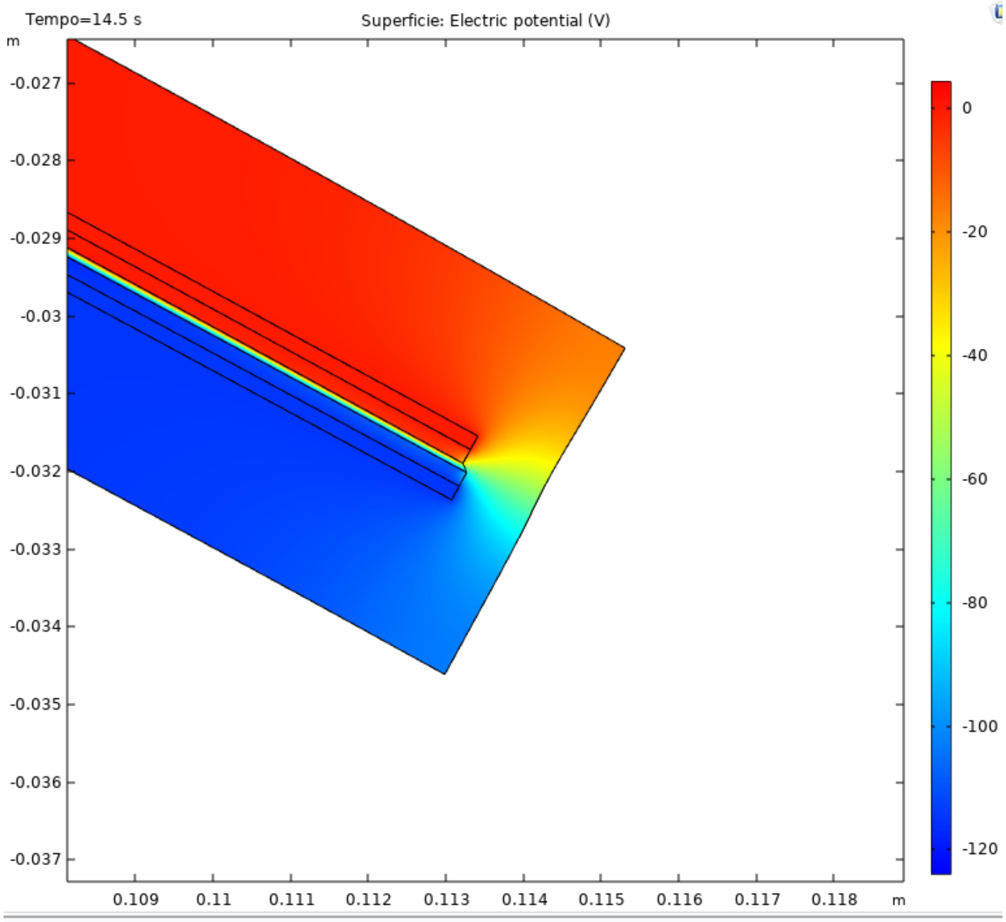

Figure 36: Detail of the polarised silicone rubber

The value of electric potential at this electrode is the result of the charge densities considered for the two dielectrics. In **Fig. 37** is a detail of the air gap separaing nylon and Kapton. The dielectric properties of air become apparent observing the image: the potential gradient covers almost the entire range of the system in the air gap alone; the intensity of colours also increases in the dielectric pair moving from the interface with air towards the copper layers, where the full intensity colours are reached. The change in colour intensity in nylon and copper is particularly evident on the lower right side of the image, where near the air stratum nylon has a light blue tonality while Kapton has an yellow-orange tonality. The same potential gradient is observable on the right side of **Fig. 36** on silicone rubber, due to the material dielectric properties.

In the prototypes, the electric potential difference is measured at the extremes of the copper layers, where establishing contact from the exterior via an external circuit is the easiest. Given this limitation of measurement, in the simulation environment the electric potential difference is evaluated on the external-most points of the copper layers. This points are obviously the 2D representation of the copper layer edge in the z-direction; expanding the image of **Fig. 36** from a 2D representation to a 3D one allows us to notice that silicone rubber polarises all along the interface interface with the triboelectric sensor. Now, while

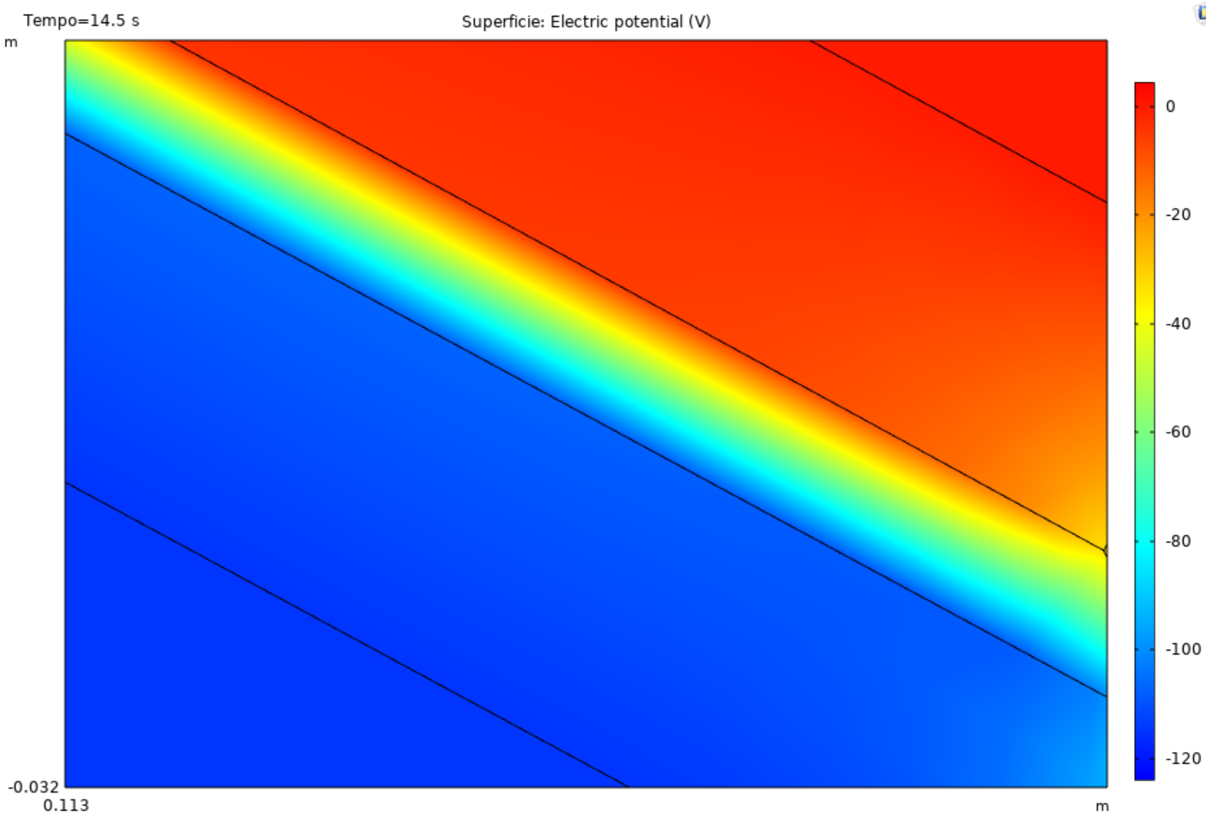

Figure 37: Detail of the polarised air gap

in the COMSOL model, being able to assign definite properties on each element basically eliminates the influence of this polarisation on the value of electric potential obtained via calculation on the considered point, in the prototypes this property of silicone rubber made evident by **Fig. 36** is not so irrelevant. Effectively, coating the sensor yields the same results in the simulation environment, but could yield very different results in prototype testing.

A final observation concerns the surface charge density adopted for the interface surfaces of nylon and Kapton. In order for the software to run its simulations it is essential to establish an electric potential difference between electrodes at $t = t_0$ which is different from zero. Choosing different values for σ affects both the initial EPD and the EPD established under external loads during the simulation. For example, with the surface charge densities adopted in these calculations, voltage at $t = t_0$ is -112 V and at the time $t = t_1$ of maximum deformation it is -117 V; with surface charge densities half in modulus to the first ones, the voltage is -56 V at t_0 and -59 V at t_1. Therefore, both the EPD of the reference state, t_0, and the potential difference between reference state and maximum deformation state change. Adopting one or the other, while affecting the numerical results, does not affect the overall behaviour of the models in which external loads cause the voltage to change from the steady-state value in accordance with the intensity of the load. Given the still rudimentary state of the robot-embedded sensors building, it isn't of particular importance having numerical results available to be compared between direct testing and COMSOL simulation, but having proof that model and prototype show the same response to external stimuli is for now of greater importance.

4.3.1 Contact-mode model - single triboelectric layer

The time-dependent trend of this first simulation is shown down below (the model is the one represented in **Fig. 26**). The loading condition is given by the sinusoidal function of **Eq. 78**. In the undeformed condition, the electric potential difference existing between upper electrode and lower electrode is slightly higher than -112 V; at the model maximum deflection, the electric potential difference approaches the -117 V value. The negative values of the EPD are the result of settings conditions: switching position between reference state electrode and floating potential electrode would yield EPDs of opposite values. As for their absolute values, they are obviously the result of the dimensions of the dielectric layers and of the surface charge densities assumed for them; changing either one would mean having different starting and final values, but the overall same trend under the same loading conditions.

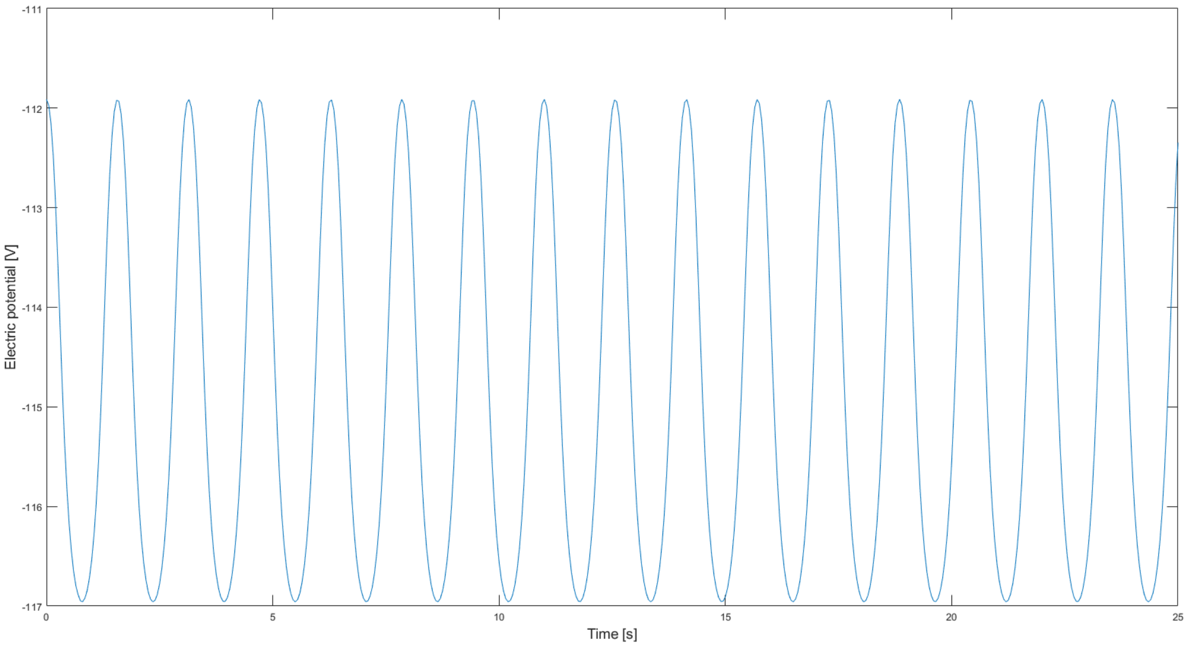

Figure 38: Time dependent simulation.

Compared with direct testings, the following observations can be made:

- the EPD measured during the tests in the maximum deflection condition, 3.5 cm, is around 3 V;
- the EDP calculated in the simulation environment in the maximum deflection condition is 5 V, so the two results are definitely comparable for this particular triboelectric sensor;
- silicone rubber polarisation, which in the prototypes influences the measurable potential difference, has a negligible effect on the simulation results;

- the loading condition in the simulation environment is a sinusoidal function, while in the tests it is a periodic impulsive load. In future simulations it would be interesting to run simulations where the loading conditions in the simulation environment better fit the loading conditions of tests;
- having to assign air solid-like properties might also influence the results of simulations; due to software limitations, though, this issue cannot be circumvented so that it is hard to measure just how much these properties affect the final results.

4.3.2 Contact-mode model - split triboelectric layer

From the first model, in the three-way split sensor the loading conditions expressed in **Eq. 78** have to be adapted to achieve comparable levels of deflection as the prototype shows under inflation during the tests. As explained, the different geometry of the system, now characterised by a single nylon layer running from end to end to work as the strain limiter of the soft robot, gives the model greater compliance under external loads. This has to be accounted for in the simulation environment by changing the curvature radius in the equation as to obtain the same deflection as the prototype during direct testing, otherwise the deflection would be far greater than what was observed on in the tests.

On each one of the three sensors the potential established at the undeformed condition is, in modulus, lower than that of the single sensor of the previous model. At rest the model registers a voltage of -108.5 V, while at maximum deflection the voltage is -112.8 V, which corresponds to an electric potential difference slightly lower than that of the first model. Moreover, unlike the tests, where measuring the EPD yielded different results for each sensor (see **Fig. 32**, **Fig. 33**, **Fig. 34** for reference), in the COMSOL model the trend and the interval of values for voltage are the same for the three sensors. In **Fig. 39** is the EPD graph of the model.

Comparing direct testing with COMSOL simulation it is possible to draw the following conclusions:

- model and prototype show very different behaviours moving from their contrained end to their free end, with electric potential difference changing cross section by cross section in the prototype, as shown in **Fig. 32**, **33** and **34**, while staying unchanged in the model;
- much like the first model, in this one too the loading condition is represented by a sinusoidal load when in the tests the loads were impulsive (and periodic);
- also in this case solid-like properties for the air stratum may affect the final results;
- the numerical results of direct testing and simulation are not comparable for this sensor due to the different scale adopted for the prototype testing due to circuit noise;

4.3.3 Sliding-mode model

The last model simulation results are represented in **Fig. 39**. The same issue that affected the prototype counterpart affects the model too, that is not having sliding-mode driven

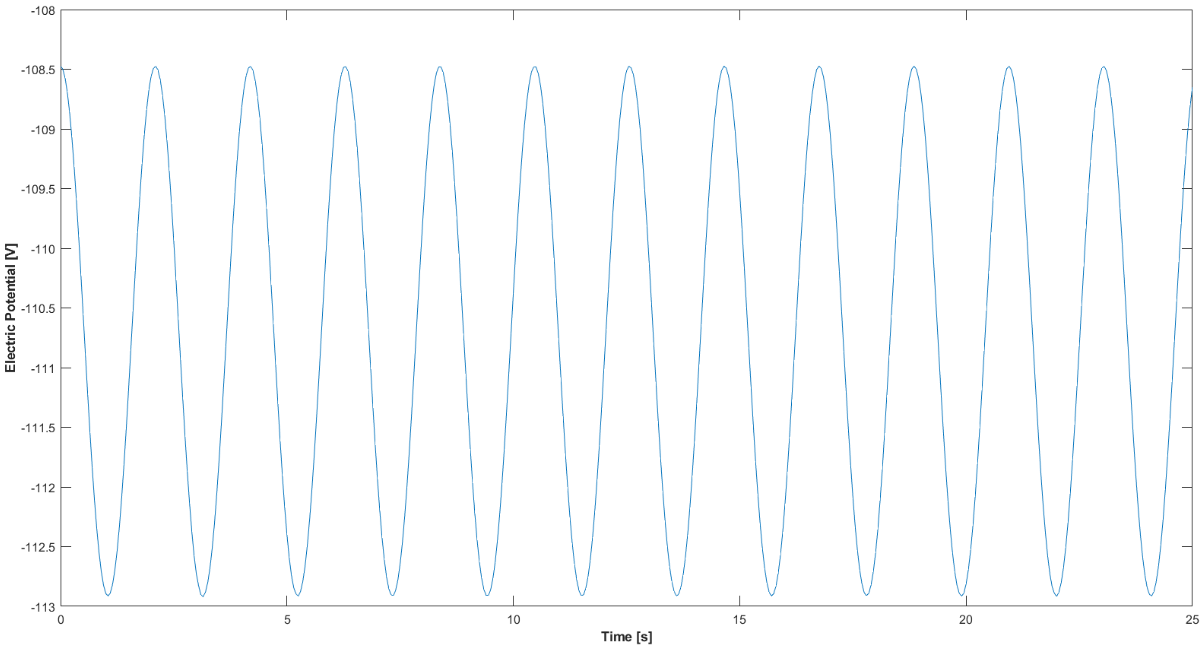

Figure 39: Time dependent simulation.

triboelectrification in the sensor in the intended working conditions. In particular, simulating the relative motion of the dielectric layer sliding on top of the two electrodes could not be achieved, thus the exchange of charges from the tribo-pair also could not be achieved. The model, therefore, actually operates like the other contact-mode sensors in which the external load forces contact along the vertical direction between the tribo-pair, instead of causing the longitudinal motion of the dielectric layer along the plane.

As for what sets the two systems apart, this one and the one adopted for the first to models, it is the arrangement of the active parts of the sensor inside the robot. In this case, the tribo-pair is made of each individual electrode and the dielectric nylon layer pressed on top of them, so that one half of the nylon layer sitting on top of one electrode functionally belongs to one element of the tribo-pair while the other half sitting on top of the other belongs to the other element of the tribo-pair. This is the so called "dielectric-to-conductor freestanding" configuration of triboelectric sensors already introduced in **chapter 1**, in which a single moving element, the dielectric material, is needed to trigger the electrification of the device. In this configuration, the same portion of the moving element, sliding along the plane, come in contact with the two electrodes prompting charge exchange and charge polarisation of the two; the greater the surface of this portion of the moving element the greater the charge exchange between electrodes.

Yet in the model, even though the nylon layer has to be electrically charged in the simulation environment due to software limitations, since one of the two electrodes has to be used as the reference state electrode of the system, charge polarisation is not achieved at time t_0 and the electric potential difference established between electrodes at this time is zero. In all other models, the reference state was always off-set by the presence of two electrically charged dielectric layers building up an electric potential difference at the electrodes different from zero, as evident from the results of **Fig. 38** and**39**. Considering again this current model, when the system is subjected to an external load, the nylon layer electrically charges the "floating potential" electrode, thus establishing a non-zero potential between the two electrodes, creating the trend described in the figure down below.

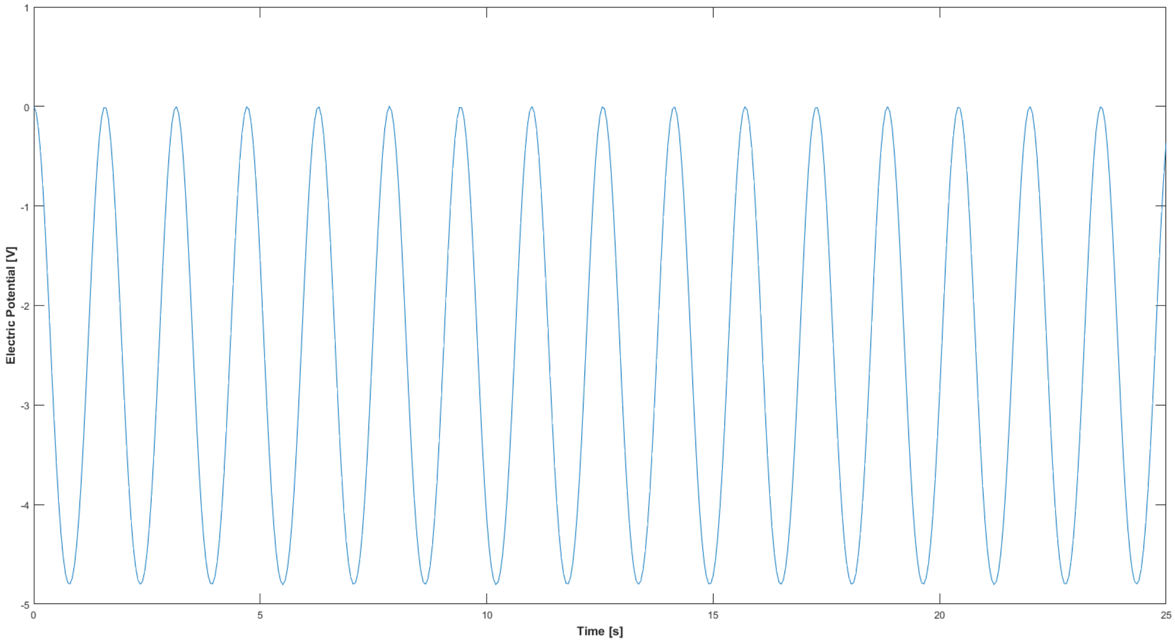

Figure 40: Time dependent simulation.

The following observations can be drawn:

- the model is inadequate to simulate the behaviour of a robot-embedded "freestanding dielectric-to-conductor" triboelectric sensor which bends under an external load;
- triboelectrification is not triggerd through a sliding motion but through the same vertical displacement of the active layer as the othe models;
- the absence of a second dielectric layer in opposition to the one present could enhance air's dielectric properties effect on final results, since now the air gap separates directly dielectric and electrode, nylon and copper, instead of dielectric and dielectric, nylon and Kapton;

4.4 Final thoughts

With the two first models it was possible to study the behaviour of robot-embedded triboelectric sensors in the simulation environment of the COMSOL software, while the last model, much like its real life counterpart, was totally inadequate for the study of the system as was conceived during its design. Some flaws were common to all three prototypes, like the necessity of a coating element to shield the silicone rubber of the soft robot body from the electric field created with the polarisation of charges between the tribo-pair during the tests. This coating element is necessary particularly as a way to correlate the influence of the dielectric properties of silicone rubber on the final results of tests, especially concering circuit noises registrable during tests. Another issue common to the three prototypes was the inability to control and gauge the separation distance between the tribo-pair, which is a crucial factor in the build-up of the electric potential difference between the electrodes under the application of external loads. Another common flaw was the non-negligible thickness of the device which affects the ability of the soft robot in which it is to be embedded to deform and bend under cycle of inflations, thus limiting the actual use of robot embedded tribo sensors.

As for the COMSOL models, the biggest issue common to all three was the assumption of solid-like properties for the stratum of air separating the two elements of the sensor tribo-pair. This assumption limited the model ability to bend under external load and also prevented the actual contact between the dielectric layers under the external load. To circumvent the air problem, the solid-like properties was akin to hyperelastic materials, so that when the model bent under inflation, the air gap would be squeezed by the tribo-pair although, as said, direct contact was not possible between the two elements of the tribo-pair. Air's own dielectric properties mitigated this limitation, enabling the polarisation of charges and charge exchange between the dielectric materials.

5 Conclusions

5.1 Summary

Triboelectric devices have the potential to become a key technology in the following years to address the energetic issues linked with our expanding markets and with the increasing demand of clean energy sources for our electronic devices. Specifically, their simple design and ease of assembling, along with their simple working principle have been fundamental factors in the study of the potential utilisation of triboelectric nanogenerators in the fields of small scale energy harvester and portable power sources for common use electronic devices such as smartphones, smartwatches, notebooks, as noted by Yanbo Zhu et al. (2016) and by A Young Choi et al. (2017). But as demonstrated by Minjeong Ha et al. (2015) and by Aifang Yu et al. (2015), the possible fields of application fo triboelectric devices don't stop with energy harvesting, in particular, they have been able to succesfully use triboelectric devices as external stimuli-detecting skin sensors. Continuing from Minjeong Ha et al. and from Aifang Yu et al.'s own works, the scope of this thesis was to futher investigate this particular field of application by implementing a triboelectric sensor to be used as a deformation sensor in soft robots.

To this scope, several prototypes were designed, built and tested, each one with a particular purpose in mind. The simplest prototype had the scope of proving whether such an application was indeed possible given the peculiar working principle of soft robots and the still-young state of the study of sensor capabilities of triboelectric devices. The inital stages of the work were thus spent trying several designs until it was possible to embed a triboelectric sensor into the robot without completely limiting the robot ability to deform under cycles of inflation. Once a working configuration was found, different configurations of the device were designed to expand the prototype capabilities and to account for the flaws emerged during inflation testing. To this end, two more prototypes were designed, one in which the sensor was split into three smaller sensor to measure the electric potential difference at different cross sections of the soft robot, while the other one was conceived as a way to reduce the overall sensor thickness which proved to be a most pressing issue for the soft robot ability to deform under inflation, as air leakage became particularly troublesome in the presence of a too-thick strain limiter represented by the triboelectric device. Both prototypes were built and then tested to see whether the soft robot could deform without the issue of air leakage occuring. Once for these prototypes as well it was possible to find a good configuration which enabled the robot to inflate, it was possible to actually prove if they were also able to correlate electric potential difference at their electrodes ends with the deformation of the soft robot under external loads, which is obviously their primary function. To this scope, before directly testing the prototypes, equivalent models were created in the simulation environment provided by the COMSOL software, to study the behaviour of the device under inflation. For each prototype a simplified equivalent model was built in the ”electrostatics” and ”solid mechanics” physics settings, and equivalent loading and constraint conditions were applied to them, so that a time-dependent response could be calculated by running these simulations for each model. The results of these simulations were to be confronted with direct testing on the prototypes to highlight some common issues as well as to gather useful data for future studies. The final step was actually testing the prototypes with an electrometer to measure the electric potential difference during the soft robot inflation.

5.2 Contributions

The results observed during the various stages of this work can be summarised in the following points, concerning both the experimental side of the work and the computer aided-simulation side of the work:

- that functioning robot-embedded triboelectric sensors could be built, proving that it is indeed possible to embed a triboelectric sensor into a soft robot without excessively reducing the ability of the latter to deform under external loads;
- that, while measuring is not yet possible due to the aforementioned rudimentary assembling methods used for the system and due to the lack of calibrated measurements, it is possible to correlate, in first analysis, the vertical displacement of the soft robot from its undeformed condition with the electrical output measured at the sensor electrodes ends;
- that even when the geometry of the triboelectric sensor was not well thought-out, like in the sliding mode sensor, it was still able to detect exernal stimuli and generate a measurable electrical output, meaning that the capabilities of these devices in this field could prove to be very promising in future applications;
- that, even with several limitations, functioning COMSOL models could be built to predict the behaviour of the system under loading conditions;
- that, while it is not possible at this stage to numerically predict the behaviour of the robot+triboelectric sensor system in the simulation environments, the prototypes and the corresponding COMSOL models show similar behaviour and results in the same loading conditions;

5.3 Future works

Future studies should focus on finding a numerical correlation between the deformation of the soft robot with the electric potential difference measured with the sensor. In this work such direct correlation could be inferred but not measured, since much of the design, assembling and testing of the prototypes was done manually. Therefore, in order to obtain numerical data gathered via direct testing to be confronted with the results calculated in a simulation environment, the human factor must be reduced. For example, being able to guarantee a certain measurable air gap thickness between the tribo-pair of the triboelectric sensor at the steady state of the system could already sensibly reduce the human factor, as the building process adopted in this work made it impossible to have standardised air gaps thicknesses for each prototype along every cross sections of the separation plane. This is particularly important since the electric potential in triboelectric devices is a direct function of the separation distance between the tribo-pair; once the initial distance is known and settable in each device and a reference electric potential state can be assigned for its steady-state, any soft robot deflection from the steady-state condition will be numerically inferrable and predictable by measuring the electric potential difference at the electrodes embedded of the sensor embedded into the robot, which is the sensors main purpose.

Bibliography

1. **Yanbo Zhu**, **Bin Yang**, **Jingquan Liu**, **Xingzhao Wang**, **Luxian Wang**, **Xiang Chen**, **Chunsheng Yang** (2016), *A flexible and biocompatible triboelectric nanogenerator with tunable internal resistance for powering wearable devices.* National Key Laboratory of Science and Technology on Micro/Nano Fabrication, Department of Micro/Nano Electronics, Shanghai Jiao Tong University, Shanghai, China.

2. **A Young Choi**, **Chang Jun Lee**, **Jiwon Park**, **Dogyun Kim**, **Youn Tae Kim** (2017), *Corrugated Textile based Triboelectric Generator for Wearable Energy Harvesting.* IT Fusion Technology Research Center and Department of IT Fusion Technology, Chosun University, Gwangju, Korea.

3. **Simiao Niu**, **Zhong Lin Wang** (2014), *Theoretical systems of triboelectric nanogenerators.* School of Materials Science and Engineering, Georgia Institute of Technology, Atlanta, USA; Beijing Institute of Nanoenergy and Nanosystems, Chinese Academy of Sciences, Beijing, China.

4. **Yunlong Zi**, **Simiao Niu**, **Jie Wang**, **Zhen Wen**, **Wei Tang** and **Zhong Lin Wang** (2015), *Standards and figure-of-merits for quantifying the performance of triboelectric nanogenerators.* School of Materials Science and Engineering, Georgia Institute of Technology, Atlanta, USA; Beijing Institute of Nanoenergy and Nanosystems, Chinese Academy of Sciences, Beijing, China.

5. **Changsheng Wu**, **Xin Wang**, **Long Lin**, **Hengyu Guo** and **Zhong Lin Wang** (2016), *Paper-Based Triboelectric Nanogenerators Made of Stretchable Interlocking Kirigami Patterns.* School of Materials Science and Engineering, Georgia Institute of Technology, Atlanta, USA; Beijing Institute of Nanoenergy and Nanosystems, Chinese Academy of Sciences, Beijing, China.

6. **Yang Wang**, **Ya Yang** and **Zhong Lin Wang** (2017), *Triboelectric nanogenerators as flexible power sources.* Beijing Institute of Nanoenergy and Nanosystems, Chinese Academy of Sciences, Beijing, China; CAS Center for Excellence in Nanoscience, National Center for Nanoscience and Technology, Beijing, China; School of Materials Science and Engineering, Georgia Institute of Technology, Atlanta, USA.

7. **Minjeong Ha**, **Jonghwa Park, Youngoh Lee**, **Hyunhyub Ko** (2015), *Triboelectric Generators and Sensors for Self-Powered Wearable Electronics.* Department of Energy Engineering, School of Energy and Chemical Engineering, Ulsan National Institute of Science and Technology (UNIST), Ulsan Metropolitan City, Republic of Korea.

8. **Aifang Yu**, **Libo Chen**, **Xiangyu Chen**, **Aihua Zhang**, **Fengru Fan**, **Yan Zhan** and **Zhong Lin Wang** (2015), *Triboelectric sensor as self-powered signal reader for scanning probe surface topography imaging.* Beijing Institute of Nanoenergy and Nanosystems, Chinese Academy of Sciences, Beijing, China; CAS Center for Excellence in Nanoscience, National Center for Nanoscience and Technology, Beijing, China; School of Materials Science and Engineering, Georgia Institute of Technology, Atlanta, USA.

9. **Carmel Majidi**, **Robert F. Shepherd**, **Rebecca K. Kramer**, **George M. Whitesides** and **Robert J. Wood** (2013), *Influence of surface traction on soft robot undulation.* The International Journal of Robotics Research.

10. **Frank L. Hammond III**, **Faye Wu** and H. **Harry Asada** (2018) *Variable Stiffness Pneumatic Structures for Wearable Supernumerary Robotic Devices.* Department of

Mechanical Engineering, MIT, Cambridge, USA.

11. *Ecoflex technical data sheet*, *Moldstar technical data sheet.* Smooth-on inc.

12. **Bobak Mosadegh**, **Panagiotis Polygerinos**, **Christoph Keplinger**, **Sophia Wennstedt**, **Robert F. Shepherd**, **Unmukt Gupta**, **Jongmin Shim**, **Katia Bertoldi**, **Conor J. Walsh**, **George M. Whitesides** (2014), *Pneumatic Networks for Soft Robotics that Actuate Rapidly.* Department of Chemistry and Chemical Biology, Wyss Institute for Biologically Inspired Engineering, School of Engineering and Applied Sciences, Harvard University, Cambridge MA, USA.

13. **Zhong Lin Wang** (2017), *On Maxwell's displacement current for energy and sensors: the origin of nanogenerators.* School of Materials Science and Engineering, Georgia Institute of Technology, Atlanta, USA; Beijing Institute of Nanoenergy and Nanosystems, Chinese Academy of Sciences, Beijing, China.

14. **Changsheng Wu**, **Aurelia C. Wang**, **Wenbo Ding**, **Hengyu Guo** and **Zhong Lin Wang** (2018), *Triboelectric Nanogenerator: A Foundation of the Energy for the New Era.* School of Materials Science and Engineering, Georgia Institute of Technology, Atlanta, USA; Beijing Institute of Nanoenergy and Nanosystems, Chinese Academy of Sciences, Beijing, China.

15. **P. Mazzoldi**, **M. Nigro**, **C. Voci**, *Elementi di fisica: elettromagnetismo e onde*, 2nd Edition. Padova, EdiSES, 2008.

16. **G. K. Ananthasuresh**, **K. J. Vinoy**, **S. Gopalakrishnan**, **K. N. Bhat**, **V. K. Aatre**, *Micro and Smart Systems: Technology and Modeling.* Bangalore, Wiley, 2012.

17. **Manfred Kaltenbacher**, *CAE of Mechatronic Systems I*, Applied Mechatronics, University of Klagenfurt, Austria.

18. **Antonio Gugliotta**, *Elementi finiti: parte II.* Torino, Otto Editore, 2002.

19. **Akira Hirose**, *Electrostatics II. Potential Boundary Value Problems*, Department of Physics and Engineering Physics, University of Saskatchewan, Saskatoon, Canada.

20. **F. Saurenbach**, **D. Wollmann**, **B.D. Terris**, **A.F. Diaz**, *Force microscopy of ion-containing polymer surfaces: morphology and charge structure*, Langmuir, 8 (4) (1992), pp. 1199-1203.

21. **Sihong Wang**, **Long Lin**, **Zhong Lin Wang** (2014), *Triboelectric nanogenerators as self-powered active sensors.* School of Materials Science and Engineering, Georgia Institute of Technology, Atlanta, USA; Beijing Institute of Nanoenergy and Nanosystems, Chinese Academy of Sciences, Beijing, China.

22. **Fridtjov Irgens**, *Continuum Mechanics*, p 232. Springer, 2008.

23. **Vinh Phu Nguyen**, *Finite elements for large deformation solid mechanics problems* (2008). Computational Mechanics Group, Falculty of Civil Engineering and Geosciences, Delft unitversity of Technology, Delft, Netherlands.

24. **Zdenek Fiala**, *Geometry of finite deformations, linearization and incremental deformations under initial stress/strain* (2008). Institute of Theoretical and Applied Mechanics, Prague, Czech Republic.

25. **P. Boulanger**, **M. A. Hayes**, *Finite amplitude waves in Mooney-Rivlin and Hadamard materials*, in *Topics in Finite Elasticity.* Ed. M. A Hayes and G. Soccomandi, International Center for Mechanical Sciences, 2001.

26. **Allan F. Bower**, *Applied mechanics of solids.* CRC press, Taylor and Francis Group, 2010.

27. **Feng-Ru Fan Zhong-Qun Tian**, **Zhong Lin Wang** (2012), *Flexible triboelectric generator.* School of Material Science and Engineering, Georgia Institute of Technology, Atlanta, USA; State Key Laboratory of Physical Chemistry of Solid Surfaces, Department of Chemistry, College of Chemistry and Chemical Engineering, Xiamen University, Xiamen, China.

28. **Simiao Niu**, **Sihong Wang**, **Long Lin**, **Ying Liu**, **Yu Sheng Zhou**, **Youfan Hua** and **Zhong Lin Wang** (2015), *Theoretical study of contact-mode triboelectric nanogenerators as an effective power source.* School of Material Science and Engineering, Georgia Institute of Technology, Atlanta, USA; Satellite Research Facility, MANA, International Center for Materials Nanoarchitectonics, National Institute for Materials Science, 1-1 Namiki, Tsukuba, Japan.

29. **Simiao Niu**, **Ying Liu**, **Sihong Wang**, **Long Lin**, **Yu Sheng Zhou**, **Youfan Hu**, **Zhong Lin Wang** (2013), *Theory of Sliding-Mode Triboelectric Nanogenerators.* School of Materials Science and Engineering Georgia Institute of Technology Atlanta, USA; Beijing Institute of Nanoenergy and Nanosystems Chinese Academy of Sciences Beijing, China.

30. **Simiao Niu**, **Ying Liu**, **Sihong Wang**, **Long Lin**, **Yu Sheng Zhou**, **Youfan Hu**, **Zhong Lin Wang** (2014), *Theoretical Investigation and Structural Optimization of Single-Electrode Triboelectric Nanogenerators.* School of Materials Science and Engineering Georgia Institute of Technology Atlanta, USA; Beijing Institute of Nanoenergy and Nanosystems Chinese Academy of Sciences Beijing, China.

31. **Simiao Niu**, **Ying Liu**, **Xiangyu Chen**, **Sihong Wang**, **Yu Sheng Zhou**, **Long Lin**, **Yannan Xie**, **Zhong Lin Wang** (2015), *Theory of freestanding triboelectric-layer-based nanogenerators.* School of Materials Science and Engineering, Georgia Institute of Technology, Atlanta, United States. Beijing Institute of Nanoenergy and Nanosystems, Chinese Academy of Sciences, Beijing, China.

32. *Mechanics of Materials*, National Chiayi University, Chiayi, Taiwan.